Advanced x-ray multilayer waveguide optics

Dissertation

zur Erlangung des mathematisch-naturwissenschaftlichen Doktorgrades

"Doctor rerum naturalium"

der Georg-August-Universität Göttingen

im Promotionsprogramm ProPhys

der Georg-August University School of Science (GAUSS)

vorgelegt von

Qi Zhong

aus Shaanxi, China

Göttingen, 2017

Thesis Committee:

Prof. Dr. Tim Salditt, Institut für Röntgenphysik, Universität Göttingen

Prof. Dr. Gerd Marowsky, Laser-Laboratorium Göttingen e.V., Universität Göttingen

Members of the Examination Board:

1st Referee: Prof. Dr. Tim Salditt, Institut für Röntgenphysik, Universität Göttingen

2nd Referee: Prof. Dr. Gerd Marowsky, Laser-Laboratorium Göttingen e.V., Universität Göttingen

Further members of the Examination Board:

Prof. Dr. Michael Seibt , IV. Physikalisches Institut, Universität Göttingen

Prof. Dr. Simone Techert, Institut für Röntgenphysik, Universität Göttingen

Prof. Dr. Hans Christian Hofsäss, II. Physikalisches Institut, Universität Göttingen

Prof. Dr. Sarah Köster, Institut für Röntgenphysik, Universität Göttingen

Date of oral examination:

11.08.2017

.

Contents

1 Introduction

Scope and outline of the thesis

With the discovery of x-rays [1], non-invasive x-ray imaging with high penetration and high resolution has become possible. In principle, given the small wavelength of hard x-rays, the resolution can even go down to the Angstrom range, according to the Abbe criterion [2]. However, the challenge is in the realization of suitable optical elements. In order to focus the x-ray beams down to nanoscale or even smaller, several kinds of x-ray optical instruments have been designed and used today: x-ray capillaries [3, 4], Kirkpatrick-Baez (KB) mirror systems [5], compound refractive lenses (CRL), Fresnel zone plates (FZP) and multilayer zone plates (MZP). In the hard x-ray range, KB mirrors have since more than ten years achieved a resolution of about 100 nm [6], and at the same time offer particularly high gain. Since the first realization of a CRL focusing to one (3.7 μm) or two (8 μm × 18 μm) spot size almost 20 years ago [7], CRLs have also undergone substantial progress and now even reach spot sizes around 50 nm [8]. Initially developed for soft x-rays, FZPs have also reached the hard x-ray regime, with focal spot sized down to 17 nm [9]. Fabricated by thin film deposition, MZPs have achieved record values of sub-5 nm point focusing of hard x-rays [10].

As a further optical element, x-ray waveguides (WGs) can be used in combination with the above to further confine and to filter radiation. Indeed, they act as spatial and coherence filters, and provide very clean and coherent wavefronts for holograhic imaging [11]. Typically, they are placed in the focal plane of a pre-focusing devices, i.e. KB mirrors or FZP, of a x-ray beamline [12]. The basic structure of a WG consists of a low density guiding core sandwiched between two high density cladding materials. The first planar WG, namely the resonant beam coupler (RBC), was fabricated and measured already in 1974 [13]. The incoming beam was coupled into the guiding core impinging onto a thin top cladding layer under the grazing incidence. The basic aim of the experiment was to extend the principle of guiding electromagnetic radiation to the x-ray range. After further progress in synchrotron radiation, a few application experiments exploiting the RBC structure were published, including application of the guiding mechanism in a Si/Polyamin/SiO$_2$ structure [14], lensless projection phase contrast microscopy [15], forming x-ray standing wave [16], and providing attractive beam dimensions for microscopy [17]. Later a new ge-

ometry of WGs, named front coupler (FC), had been introduced, both for one-dimensional (1D) and two-dimensional (2D) waveguides. First, the incoming beam was coupled at the front face of a one-dimensional waveguide (1DWG) with tunable air gaps [18]. Two-dimensionally confining channel waveguides (2DWGs) have been introduced by Pfeiffer et al. [19]. The fabrication of 2DWGs requires advanced electron lithography with interferometric positioning and suitable pattern transfer techniques, in order to reach the required aspect ratios. The fabrication of 2DWGs was improved by Fuhse et al. [20], and more recently extended from overgrown polymer channels to air channels capped by wafer bonding techniques [21], serving several different x-ray optical purposes like beam splitting for interferometry [22] and tapered waveguides channels with an exit size of 16.5 nm × 14.6 nm [23] or angular redirections to "bend" x-rays [24].

Notwithstanding these successful developments, lithography still lacks the precision to which planar thin films can be fabricated [25]. For example, the theoretical limits for beam collimation was shown and demonstrated to be in the range of 10 nm depending on the material [26]. With thin film deposition techniques, notably 8 nm [27,28] for the given material could be reached in a planar thin film waveguide with an optimized cladding material ($Mo/C/Mo$ structure embedded in Ge wafers [29]). Furthermore, the single guiding film [30, 31] or the cladding film [32,33] can be generalized to a multilayer structure. Therefore, for purposes of the highest beam confinement or to exploit novel geometries as in this thesis, waveguiding in only one dimension as in an array of thin planar films, is suitable and attractive, owing to a better control of layer sequences.

Outline

The aim of this thesis is to demonstrate that x-ray waveguide optics can be generalized from a single guiding film to an array of planar waveguides, enabling more complex and controllable phenomena of field propagation both in particular in the near-field in the vicinity of objects to be probed by coherent imaging. Two advanced x-ray multilayer waveguides (MWGs) structures, i.e. the **waveguide array (WGA)** and the multi-guide **resonant beam couplers (RBCs)** are designed and discussed. Starting from basic theoretical analysis, the structural model of MWGs is built up. Then the MWGs are studied in detail by numerical simulations based on finite-difference (FD) simulations, fabricated with precision methods for controlled layer thickness, and finally characterized experimentally by phase retrieval methods.

Chap. 1 introduces the basic theory of x-ray waveguides (see section 1.1), and

presents geometries and mechanisms of different coupling devices (see section 1.2). FD simulations and phase retrieval methods are discussed to characterize the field propagation in the near-field and far-field (see section 1.3). In the final section 1.4, the fabrication processes of multilayers and MWGs are presented. Thereafter, the x-ray beams exiting from MWGs are characterized by x-ray reflectivity and far field measurements with focused synchrotron radiation.

Chap. 2 presents the concept of WGA, using the WGA structure with Mo/C multilayer at 19.9 keV photon energy. The controlled variation in guiding layer thickness is introduced to achieve the desired phase shifts between the guided output beams. The FD simulations show that multi-beam interference with the desired phase shifts can lead to a quasi-focal spot sized sub-50 nm in free space behind the waveguide.

Chap. 3 uses two iterative phase retrieval algorithms to reconstruct the near-field distribution behind tailored WGA and - for comparison - simpler periodic waveguide multilayers (WGM) with Ni/C multilayer structure for 13.8 keV photon energy. These are shown to yield distinctly different near-field patterns. Importantly, the WGA also exhibits the desired secondary quasi-focal spot outside the structure.

Chap. 4 presents the coupling of finite (sub-μm) x-ray beams into RBCs with three guiding layers in the $[Ni/C]_3 /Ni$ structure. Using especially resonant mode excitation, more than one reflected beams are generated with different beam offsets along the RBC surface constituting an exceptionally large Goos-Hänchen effect. Possible applications of such devices are beam splitters for coherent imaging and interferometry.

Chap. 5 summarizes the outcomes of this thesis, and discusses future applications and investigations of the WGA and multi-guide RBCs structures.

1.1 Fundamentals of X-ray waveguides

To describe the theoretical background of hard x-ray waveguides in this section, subsection 1.1.1 first presents the propagation of wave fields in a planar waveguide (WG) [20, 25, 34–39]. Using the analytical and numerical calculations, the concept of mode propagation inside a guiding layer is shown. Thereafter, subsection 1.1.2 discusses the relationship between the exit phase φ and guiding layer thickness d in the multilayer waveguides (MWGs).

1.1.1 Planar waveguides
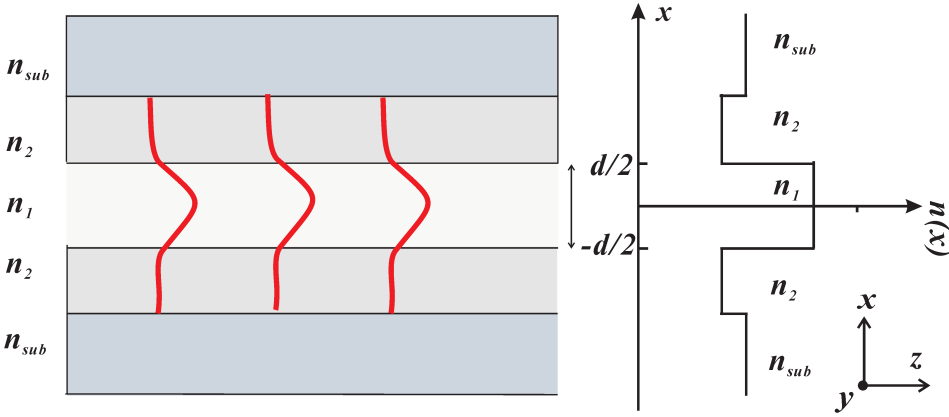
Figure 1.1: **Principle of waveguiding. (a) Sketch of a planar WG, with a guided mode sketched in red, and also in a geometric optical picture. The mode propagates along z inside the guiding layer. (b) The refraction index profile n(x) with $n_2 < n_1 < 1$.**

We consider a planar thin film with index of refraction n_1 and thickness d, sandwiched between two cladding layers of index n_2. In general, there is also a substrate material with n_{sub}; but for thick cladding layers, the substrate influence can be neglected. This planar WG is sketched in Fig. 1.1(a) and (b). Now, the index of refraction profile $n(x)$ is independent of y and z, and reads

$$n(x) = \left\{ \begin{array}{ll} n_1, & |x| \le d/2 \\ n_2, & |x| > d/2 \end{array} \right. ; \tag{1.1}$$

The electric field of TE mode inside the planar WG is determined by the reduced Helmhotz equation [34–36]

$$d^2 E_y / dx^2 + [k_0^2 n^2(x) - \beta^2] E_y = 0, \tag{1.2}$$

where β is the propagation constant, and the wave number is $k = 2\pi/\lambda$. Since the guided mode is confined inside the guiding layer with thickness d, the propagation constant β is restricted to $k_0^2 n_2^2 \leq \beta^2 \leq k_0^2 n_1^2$. The solutions of Eq.(1.2) can be written as symmetrical and asymmetrical modes:

$$E_y^{sym}(x) = \begin{cases} A\cos(\kappa x), & |x| \leq d/2 \\ Ce^{-\gamma|x|}, & |x| > d/2 \end{cases}, \tag{1.3}$$

$$E_y^{asym}(x) = \begin{cases} B\sin(\kappa x), & |x| \leq d/2 \\ De^{-\gamma|x|}, & |x| > d/2 \end{cases}, \tag{1.4}$$

with $\gamma^2 = \beta^2 - k_0^2 n_2^2$ and $\kappa^2 = k_0^2 n_1^2 - \beta^2$. Requiring continuity of the electric field and its derivative, the guided modes have to fulfill these transcendental equations:

$$\xi\tan\xi = \left[\left(\frac{V}{2}\right)^2 - \xi^2\right]^{1/2} \tag{1.5}$$

for symmetrical modes;

$$-\xi\cot\xi = \left[\left(\frac{V}{2}\right)^2 - \xi^2\right]^{1/2} \tag{1.6}$$

for asymmetrical modes.
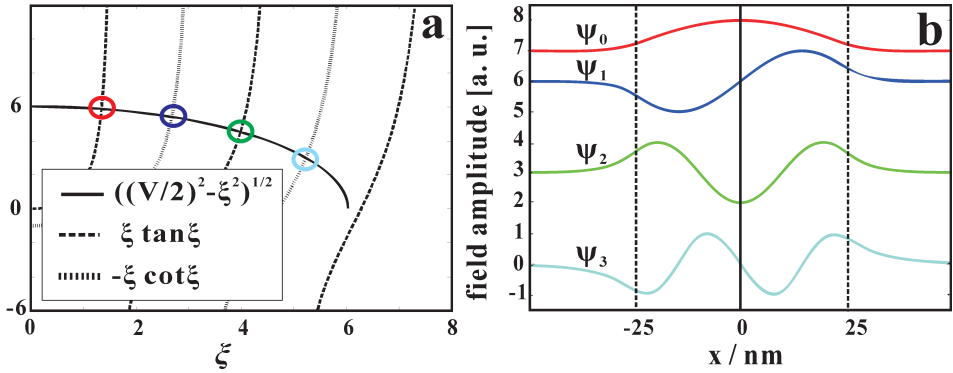
Figure 1.2: *Graphical solution of the eigenvalue problem. (a) The numbers of intersection points of $\xi\tan\xi$ and $\xi\cot\xi$ as a function of ξ for a planar $Ni/C/Ni$ WG with $n_1 = n_C = 1 - 7.18 \times 10^{-6}$, $n_2 = n_{Ni} = 1 - 2.49 \times 10^{-5}$ and $d_C = 50$ nm represent 4-mode propagation (V = 12.06) for a photon energy $E = 8$ keV. (b) Calculated field intensity distribution $|\psi_m(x)|^2$, $m = 1,...,4$.*

Here, the waveguide parameter is $V = k_0 d(n_1^2 - n_2^2)^{1/2}$, and the propagation constant is $\beta = (k_0^2 n_1^2 - 4\xi^2/d^2)^{1/2}$.

The number of the guided modes can be expressed as

$$M = \lceil \frac{V}{\pi} \rceil \tag{1.7}$$

which is mainly influenced by the waveguide parameters V and $\lceil\,\rceil_{int}$ indicates that the term is rounded up to the next integer. Hence, the guided mode of the planar WG is mainly determined by the guiding layer thickness d, and the given x-ray photon energy. Fig. 1.2(a) illustrates the graphic solution of the transcendental equations of Eq.(1.5) and (1.6). Fig. 1.2(b) presents the calculated profiles of the electric field intensity $|\psi_m(x)|^2$ of four TE modes for the system Ni/C (50 nm)$/Ni$ WG at 8 keV photon energy. To obtain mono-modal guiding ($V_{m=0} = \pi$) in the planar WG, the guiding layer thickness should be narrowed to a smaller size ($d_C \leq 13$ nm) [39]. The analogous analysis of TM mode can also be calculated [34]. In order to perform these calculations, we select the TE modes of a WG in the subsequent discussion.

1.1.2 Multilayer waveguides

In this subsection, we extend the WG structure from a single guiding layer to an array of guiding layers. This is performed with the goal to provide tailored beams (probes) for x-ray imaging experiments, exploiting special properties in the near-field. In particular, we want to investigate whether it is possible to achieve a focused beam outside the WG itself.

Fig. 1.3(a) presents the MWG, consisting of seven guiding layers in red and eight cladding layers in purple, which produces a guided mode in each guiding layer i with a required exit phase φ_i. The guiding layer thickness is d_i ($i = 1,...,7$), and the thicknesses of two adjacent cladding layers are c_j and c_{j+1} ($j = 1,...,7$). The refractive indices of guiding and cladding layers are n_1 and n_2, respectively. Let us briefly consider a beam propagation in a reference planar WG with a working length L. The initial guiding layer thickness and cladding layer thickness are d_0 and c_0, respectively, as shown in Fig. 1.3(b). Note that in contrast to the planar WG, the MWG generates x-ray guided modes in each guiding layer i. The exiting field consists of multiple beamlets which interfere to give modulated 'tailored' near-field interference patterns. In order to achieve special multi-beam interference patterns outside the MWG, the exit beamlets can be designed with tailored phases. To this purpose, the relationship between the exit phase φ_i and
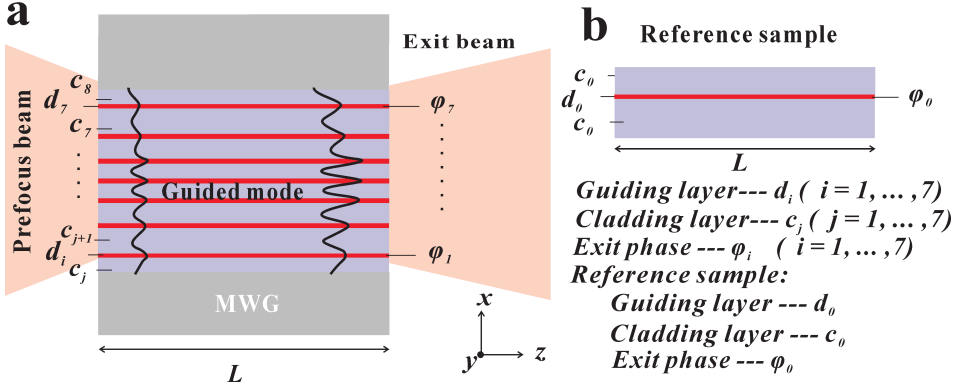
Figure 1.3: *The structures of MWG and planar reference WG. (a) The schematic structure of MWG consists of seven guiding layers in red (d_i, $i = 1,...,7$) and eight cladding layers in purple (c_j, $j = 1,...,7$). After coupling the prefocus beam, the guided mode is excited in each guiding layer. With the working length L, the exit phase φ_i from the corresponding guiding layers i can be controlled by the variation of layer thickness d_i. (b) The phase of reference sample with length L is φ_0, with the corresponding guiding layer thickness d_0 and cladding layer thickness c_0.*

guiding layer thickness d_i would be discussed in the following.

From Eq.(1.2), we see that the guided beam's phase is given by $\varphi = \beta \cdot L$. We assume L and the indices of refraction $n_{1,2}$ fixed. Hence, the phase relations φ_i can be tailored by designing the propagation constants β_i in symmetrical and asymmetrical modes, respectively. Rewriting the equation of β_i, we have

$$\xi_i = \frac{d_i}{2}\sqrt{k_0^2 n_1^2 - \beta_i^2} \qquad (1.8)$$

Symmetrical modes

A series expansion for small changes $d_i \to d_0 + \Delta d_i$, $\xi_i \to \xi_0 + \Delta \xi_i$ and $V_i \to V_0 + \Delta V_i$ yield the transcendental equation

$$(\xi_0 + \Delta \xi_i)\tan(\xi_0 + \Delta \xi_i) = \sqrt{\left(\frac{V_0 + \Delta V_i}{2}\right)^2 - (\xi_0 + \Delta \xi_i)^2}; \qquad (1.9)$$

Separately using Taylor expansions for the *Left* and *Right* sides of the Eq.(1.9),

the *Left* is expressed as

$$Left \rightarrow (\xi_0 + \Delta\xi_i)\tan(\xi_0 + \Delta\xi_i)$$

$$= (\xi_0 + \Delta\xi_i)\left(\tan\xi_0 + \frac{\Delta\xi_i}{\cos^2\xi_0}\right) \qquad ; \qquad (1.10)$$

$$= \xi_0\tan\xi_0 + \frac{\xi_0\Delta\xi_i}{\cos^2\xi_0} + \Delta\xi_i\tan\xi_0 + o(\Delta\xi_i)$$

When $o(\Delta\xi_i) \rightarrow 0$, we modify Eq.(1.10) to

$$Left \simeq \xi_0\tan\xi_0 + \Delta\xi_i\left(\tan\xi_0 + \frac{\xi_0}{\cos^2\xi_0}\right). \qquad (1.11)$$

For the *Right*,

$$Right \rightarrow \sqrt{\left(\frac{V_0 + \Delta V_i}{2}\right)^2 - (\xi_0 + \Delta\xi_i)^2}$$

$$= \sqrt{\frac{V_0^2 + 2V_0\Delta V_i + o(\Delta V_i)}{4} - \xi_0^2 - 2\xi_0\Delta\xi_i - o(\Delta\xi_i)} \qquad ; \qquad (1.12)$$

When $o(\Delta\xi_i) \rightarrow 0$ and $o(\Delta V_i) \rightarrow 0$, the *Right* is given by

$$Right \rightarrow \sqrt{\left(\frac{1}{4}V_0^2 - \xi_0^2\right) + \frac{1}{2}V_0\Delta V_i - 2\xi_0\Delta\xi_i}$$

$$= \sqrt{\left(\frac{1}{4}V_0^2 - \xi_0^2\right)\left(1 + \frac{\frac{1}{2}V_0\Delta V_i - 2\xi_0\Delta\xi_i}{\frac{1}{4}V_0^2 - \xi_0^2}\right)} \qquad ; \qquad (1.13)$$

$$\simeq \sqrt{\left(\frac{1}{4}V_0^2 - \xi_0^2\right)}\left(1 + \frac{1}{2}\frac{\frac{1}{2}V_0\Delta V_i - 2\xi_0\Delta\xi_i}{\frac{1}{4}V_0^2 - \xi_0^2}\right)$$

Based on Eq.(1.5), then the *Right* is expressed as

$$Right \rightarrow (\xi_0\tan\xi_0)\left(1 + \frac{1}{2}\frac{\frac{1}{2}V_0\Delta V_i - 2\xi_0\Delta\xi_i}{\xi_0^2\tan^2\xi_0}\right) \qquad ; \qquad (1.14)$$

$$= \xi_0\tan\xi_0 + \frac{1}{2}\frac{\frac{1}{2}V_0\Delta V_i - 2\xi_0\Delta\xi_i}{\xi_0\tan\xi_0}$$

When the $Left$ (Eq.(1.11)) equals to the $Right$ (Eq.(1.14)), the equation is changed to

$$\frac{1}{4} V_0 \Delta V_i = \Delta \xi_i \left(\xi_0 \tan^2 \xi_0 + \frac{\xi_0^2 \tan \xi_0}{\cos^2 \xi_0} + \xi_0 \right); \tag{1.15}$$

Inserting the waveguide parameter $V_0 = k_0 d_0 \sqrt{(n_1^2 - n_2^2)}$ yields $\frac{1}{4} V_0 \Delta V_i = \frac{1}{4} k_0^2 (n_1^2 - n_2^2) d_0 \Delta d_i$, then Eq.(1.15) becomes

$$\Delta \xi_i = \frac{1}{4} \frac{k_0^2 (n_1^2 - n_2^2) d_0 \Delta d_i}{\xi_0 \left(1 + \frac{\xi_0 \sin \xi_0}{\cos^3 \xi_0} + \tan^2 \xi_0 \right)} = \frac{1}{4} \frac{V_0^2 \Delta d_i}{d_0 \xi_0 \left(1 + \frac{\xi_0 \sin \xi_0}{\cos^3 \xi_0} + \tan^2 \xi_0 \right)}. \tag{1.16}$$

We also do the expansion for $\beta_i \to \beta_0 + \Delta \beta_i$

$$\beta_0 + \Delta \beta_i = \sqrt{k_0^2 n_1^2 - \frac{4(\xi_0 + \Delta \xi_i)^2}{(d_0 + \Delta d_i)^2}}. \tag{1.17}$$

To solve the right side,

$$Right \to \frac{1}{(d_0 + \Delta d_i)} \sqrt{k_0^2 n_1^2 (d_0 + \Delta d_i)^2 - 4(\xi_0 + \Delta \xi_i)^2}$$

$$= \frac{1}{(d_0 + \Delta d_i)} \sqrt{k_0^2 n_1^2 d_0^2 + 2 k_0^2 n_1^2 d_0 \Delta d_i + o(\Delta d_i) - 4\xi_0^2 - 8\xi_0 \Delta \xi_i - o(\Delta \xi_i)} \quad ; \tag{1.18}$$

When $o(\Delta \xi_i) \to 0$ and $o(\Delta d_i) \to 0$, then

$$Right \to \frac{1}{(d_0 + \Delta d_i)} \sqrt{(k_0^2 n_1^2 d_0^2 - 4\xi_0^2) \left(1 + \frac{2 k_0^2 n_1^2 d_0 \Delta d_i - 8\xi_0 \Delta \xi_i}{k_0^2 n_1^2 d_0^2 - 4\xi_0^2} \right)} \quad ; \tag{1.19}$$

$$\simeq \frac{1}{(d_0 + \Delta d_i)} \sqrt{(k_0^2 n_1^2 d_0^2 - 4\xi_0^2)} \left(1 + \frac{1}{2} \frac{2 k_0^2 n_1^2 d_0 \Delta d_i - 8\xi_0 \Delta \xi_i}{k_0^2 n_1^2 d_0^2 - 4\xi_0^2} \right)$$

Inserting Eq.(1.16) and $\beta_0 d_0 = \sqrt{k_0^2 n_1^2 d_0^2 - 4\xi_0^2}$ into Eq.(1.17) and (1.19), the $\Delta \beta_i$

is given by

$$\Delta\beta_i = \frac{\Delta d_i}{d_0 + \Delta d_i}\left[\frac{k_0^2 n_1^2}{\beta_0} - \frac{V_0^2}{d_0^2\beta_0\left(1 + \frac{\xi_0\sin\xi_0}{\cos^3\xi_0} + \tan^2\xi_0\right)} - \beta_0\right]. \tag{1.20}$$

For Δd_i close to zero, $\partial\xi/\partial d \approx \Delta\xi_i/\Delta d_i$ and $\partial\beta/\partial d \approx \Delta\beta_i/\Delta d_i$. This determines a first-order relationship $\partial\beta/\partial d$ between propagation constant β_i and guiding layer thickness d_i for symmetrical modes:

$$\frac{\partial\beta}{\partial d} \approx \frac{\Delta\beta_i}{\Delta d_i} = \frac{k_0^2 n_1^2}{d_0\beta_0} - \frac{V_0^2}{d_0^3\beta_0\left(1 + \frac{\xi_0\sin\xi_0}{\cos^3\xi_0} + \tan^2\xi_0\right)} - \frac{\beta_0}{d_0}; \tag{1.21}$$

Asymmetrical modes

The similar expressions for small changes ($d_i \rightarrow d_0 + \Delta d_i$, $\xi_i \rightarrow \xi_0 + \Delta\xi_i$, $V_i \rightarrow V_0 + \Delta V_i$ and $\beta_i \rightarrow \beta_0 + \Delta\beta_i$) yield the transcendental equation Eq.(1.6) to

$$-(\xi_0 + \Delta\xi_i)\cot(\xi_0 + \Delta\xi_i) = \sqrt{\left(\frac{V_0 + \Delta V_i}{2}\right)^2 - (\xi_0 + \Delta\xi_i)^2}; \tag{1.22}$$

Using analogous procedures as shown in *Symmetrical modes* and inserting the waveguide parameter $V_0 = k_0 d_0\sqrt{(n_1^2 - n_2^2)}$ into Eq.(1.22), then it is expressed as

$$\Delta\xi_i = \frac{1}{4}\frac{V_0^2\Delta d_i}{d_0\xi_0\left(1 - \frac{\xi_0\cos\xi_0}{\sin^3\xi_0} + \cot^2\xi_0\right)}. \tag{1.23}$$

Thus $\Delta\beta_i$ is given by

$$\Delta\beta_i = \frac{\Delta d_i}{d_0 + \Delta d_i}\left[\frac{k_0^2 n_1^2}{\beta_0} - \frac{V_0^2}{d_0^2\beta_0\left(1 - \frac{\xi_0\cos\xi_0}{\sin^3\xi_0} + \cot^2\xi_0\right)} - \beta_0\right]. \tag{1.24}$$

For Δd_i close to zero, $\partial\xi/\partial d \approx \Delta\xi_i/\Delta d_i$ and $\partial\beta/\partial d \approx \Delta\beta_i/\Delta d_i$. The relationship between $\partial\beta$ and ∂d for asymmetrical modes gives

$$\frac{\partial\beta}{\partial d} \approx \frac{\Delta\beta_i}{\Delta d_i} = \frac{k_0^2 n_1^2}{d_0\beta_0} - \frac{V_0^2}{d_0^3\beta_0\left(1 - \frac{\xi_0\cos\xi_0}{\sin^3\xi_0} + \cot^2\xi_0\right)} - \frac{\beta_0}{d_0}. \tag{1.25}$$

Fig. 1.4 shows the relationship $\partial\beta/\partial d$ as a function of d in the symmetrical ($V_0 = \pi$ in red line) and asymmetrical ($V_0 = 5$ in blue line) modes. With certain V_0, we simplify the Eq.(1.21) and (1.25) to

$$\frac{\partial\beta}{\partial d} = \frac{A-\beta}{d} - \frac{B}{d^3},\qquad(1.26)$$

which A is $(k_0^2 n_1^2)/\beta_0$ and $\beta = \beta_0$. B is given by

$$B = \begin{cases} \dfrac{V_0^2}{\beta_0\left(1 + \dfrac{\xi_0\sin\xi_0}{\cos^3\xi_0} + \tan^2\xi_0\right)}, & \text{for symmetrical modes;} \\[3em] \dfrac{V_0^2}{\beta_0\left(1 - \dfrac{\xi_0\cos\xi_0}{\sin^3\xi_0} + \cot^2\xi_0\right)}, & \text{for asymmetrical modes;} \end{cases}\qquad(1.27)$$
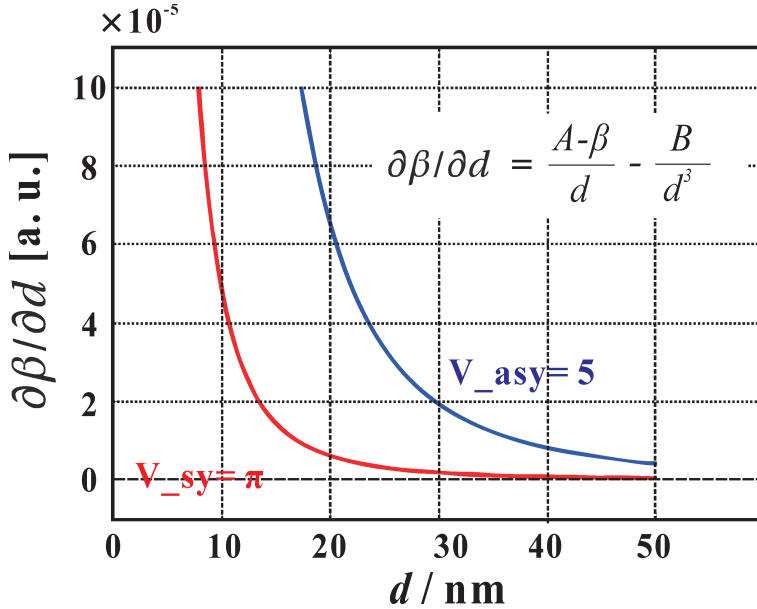
Figure 1.4: *Relationship $\partial\beta/\partial d$ in symmetrical and asymmetrical modes. The relationship $\partial\beta/\partial d$ as a function of d for a planar $Ni/C/Ni$ WG with $n_1 = n_C = 1 - 7.18 \times 10^{-6}$, $n_2 = n_{Ni} = 1 - 2.49 \times 10^{-5}$ presents the curves in symmetrical mode ($V_0 = \pi$ in red line) and asymmetrical mode ($V_0 = 5$ in blue line) for a photon energy $E = 8\,keV$, respectively.*

When the working length L, guiding layer thickness d_0, and initial phase φ_0 are given in the reference sample (Fig. 1.3(b)), the relationship $\partial\beta/\partial d$ of the symmetrical and asymmetrical modes are shown in Fig. 1.4. At present, only the relative phase difference $\Delta\varphi_i = \varphi_0 - \varphi_i$ matters for the near-field distribution. The propagation constant difference then follows from $\Delta\beta_i = \Delta\varphi_i/L$. Finally, with the corresponding slight changes in the guiding layer thickness ($\Delta d_i = \Delta\beta_i/(\partial\beta/\partial d)$), the guiding layer thicknesses ($d_i = d_0 - \Delta d_i$, $i = 1,...,7$) can be determined. To this end, the relative phases φ_i of guided beams has to be controlled via the guiding layer thickness d_i ($i = 1,...,n$). We use Mathematica to calculate the Eq.(1.21) and (1.25), as shown the source codes in App. A.1.1. The numerical simulations and calculations between φ_i and d_i are discussed in section 2.2 in Chapter 2.

1.2 Coupling geometry and mechanism

In this section, the geometries and mechanisms of different waveguides are discussed, exhibiting interesting phenomena in the near-field distributions. With the analytical and numerical simulations in subsection 1.2.1, we first present some common geometries of front couplers (FCs) and then go on to the waveguide array (WGA). Subsection 1.2.2 presents the simulations in the multi-guide resonant beam couplers (RBCs).

1.2.1 Front couplers

In the previous section, the basic theory of planar WG was presented. The FC scheme is based on the planar WG where an incident beam is coupled at the front side of the structure. With different geometries of guiding cores, there are several types of FCs, e.g. straight waveguides [25], tapered waveguides [23], curved waveguides [24], and so on.

Fig. 1.5(a) shows a schematic of straight WG. The low density guiding layer (C layer) is sandwiched between two high density cladding layers (Mo layers). Based on the FD simulations [20, 25, 37], the $Mo/C/Mo$ WG with guiding layer thickness d_C and working length $L = 0.28$ mm, is calculated with an incoming plane wave of unit intensity for 19.9 keV photon energy. In Fig. 1.5(b) of $d_C = 8$ nm, only one mode is guided. Up d_C to 100 nm in Fig. 1.5(c), four guided modes are observed. For comparison, the schematic and simulation of tapered WG are also depicted in Fig. 1.5(c, d), with the entrance size 100 nm and exit size 8 nm. The corresponding 1D intensity profiles for the straight WG of $d_C = 8$ nm, straight WG of $d_C = 100$ nm and tapered WG are plotted in the exit plane as shown in Fig. 1.5(f). From the simulations, the tapered WG exhibits a higher exit intensity than the straight WGs.

Considering a guiding layer in straight WGs replaced with an array of guiding layers, a novel WG variant, which we named WGA, can be designed. Firstly, it serves to increase the coupling efficiency, i.e. collecting more incoming beam intensity by a larger effective geometric cross section. Second, additional geometric parameters in particular the individual guiding layer thickness and positions allow to modulate the mode structure and interference pattern at the exit. In particular, if the exiting beamlets of different guiding layers can be adjusted correspondingly, the near-field distributions could be tailored to achieve some special interference patterns, e.g. creating a quasi-focal spot.

Using several parallel layers, with the aim to generate a focused pattern outside
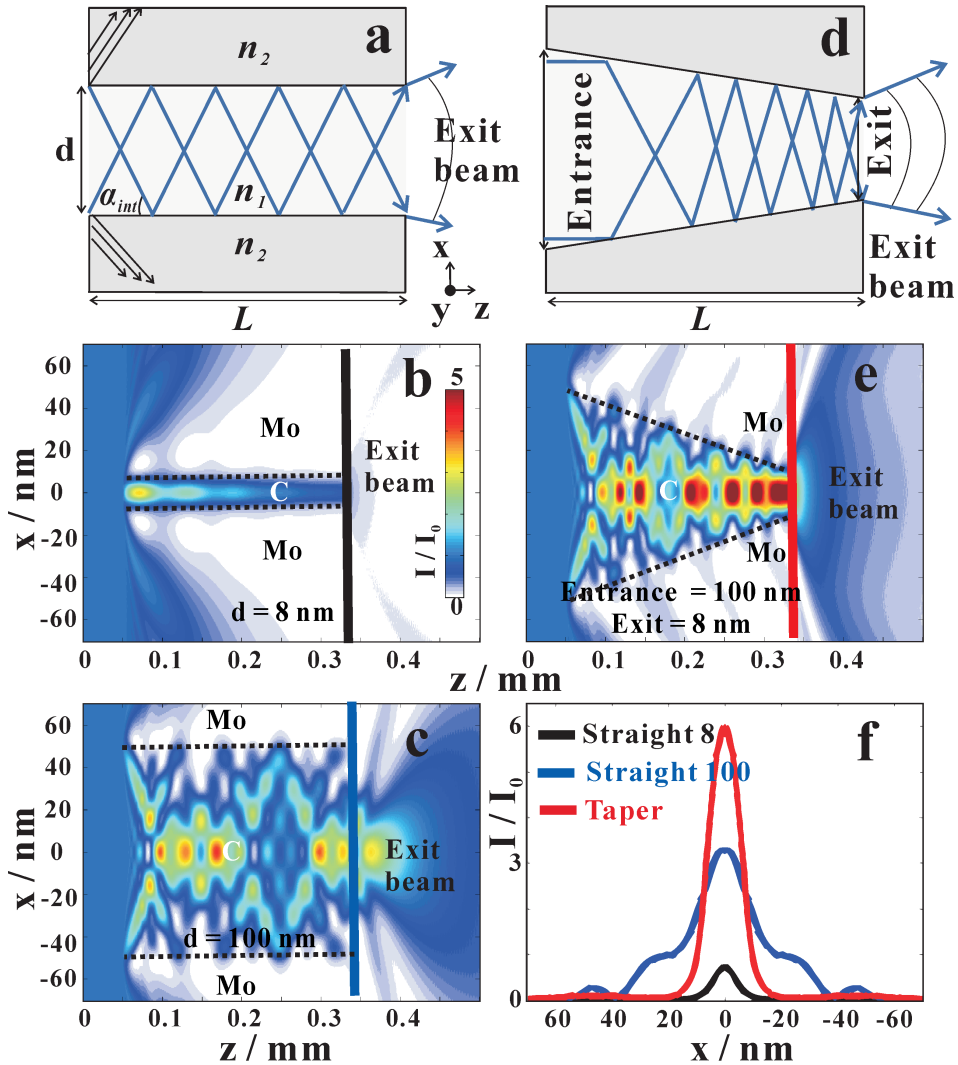
Figure 1.5: *Guiding properties of front couplers. (a) The schematic structure of straight waveguides with one guiding layer n_1, two cladding layers n_2. The field propagation of straight waveguides $Mo/C/Mo$ with different guiding layer thicknesses d_C of (b) d_C=8 nm and (c) d_C=100 nm are simulated in the near-field by FD calculations with an incoming plane wave of unit intensity and 19.9 keV photon energy. The simulations are for waveguide lengths L = 0.28 mm. (d) The schematic structure of tapered waveguides. (e) The field distribution of tapered waveguides with entrance size 100 nm and exit size 8 nm, are also calculated for the length L. (f) The intensity profiles in the exit plane for the straight waveguides with d_C = 8 nm (black line, (b)) and d_C = 100 nm (blue line, (c)), and tapered waveguides (red line, (e)) are compared.*

the structure, one may ask, how such a WGA would differ from the well-known Fresnel zone plate (FZP) [40, 41]. First of all, waveguide modes are a solution to a volume (extended) structure, while the functioning of a FZP avoids volume diffraction. In other words, the WGA can become very thick without loosing the mode structure, while the FZP should be optically thin. This is important for high energy applications. Second, the mechanism of multi-beam interference is different. In the layers of the FZP, the phase shift is the same in all layers of high and low density, respectively, while the phase shift in the WGA is tailored in each guiding layer by the way of adjusting the propagation constant β. Of course, the WGA demonstrated in a proof-of-concept in this work with just a few layers cannot compete with a state-of-the-art FZP, which often has some hundreds or thousands of layers to exploit for focusing.
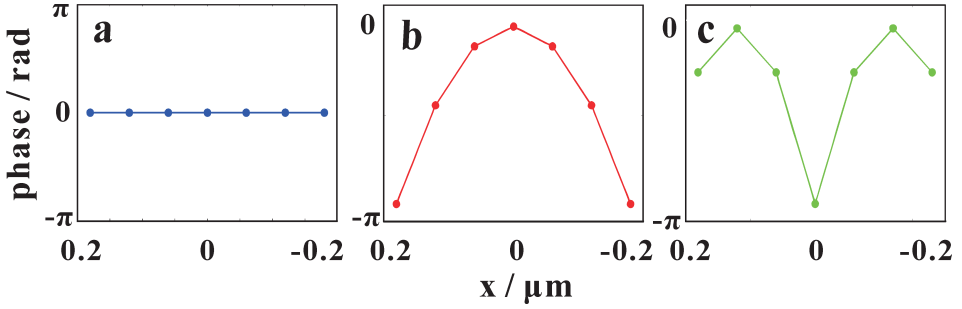
Figure 1.6: *Different phase profiles. Different phase profiles φ_i for a seven-channels structure: (a) constant phase profile in blue (flat), (b) a parabolic phase profile in red and (c) a "double focused phase" profile in green.*

To design the WGA, we first derive analytical expressions for the phase shift in Fig. 1.6 and 1.7, and then verify the performance by numerical FD simulations in Fig. 1.8.

Fig. 1.6 illustrates the different phase profiles: (a) constant phase profile in red (flat), (b) a parabolic phase profile in blue and (c) a "double focused phase" profile in green. Fig. 1.7 presents the multi-beam interference in free space from multiple channels, i.e. (a, b, c) five channels, (d, e, f) six channels, and (g, h, i) seven channels using the similar phase profiles as presented in Fig. 1.6. Each channel emits a Gaussian beam of unit intensity, and with constant width ($FWHM$) of 8 nm (channel width). The distance between each channel is 60 nm, which is close to the fabricated parameters for 19.9 keV photon energy. In the profiles of five channels ($i = 1, \ldots, 5$), the phases of guided beams are denoted as φ_i. Clearly, if all φ_i have the same values, this multi-channel structure is equivalent to a simple grating. Fig. 1.7(a) shows the corresponding near-field
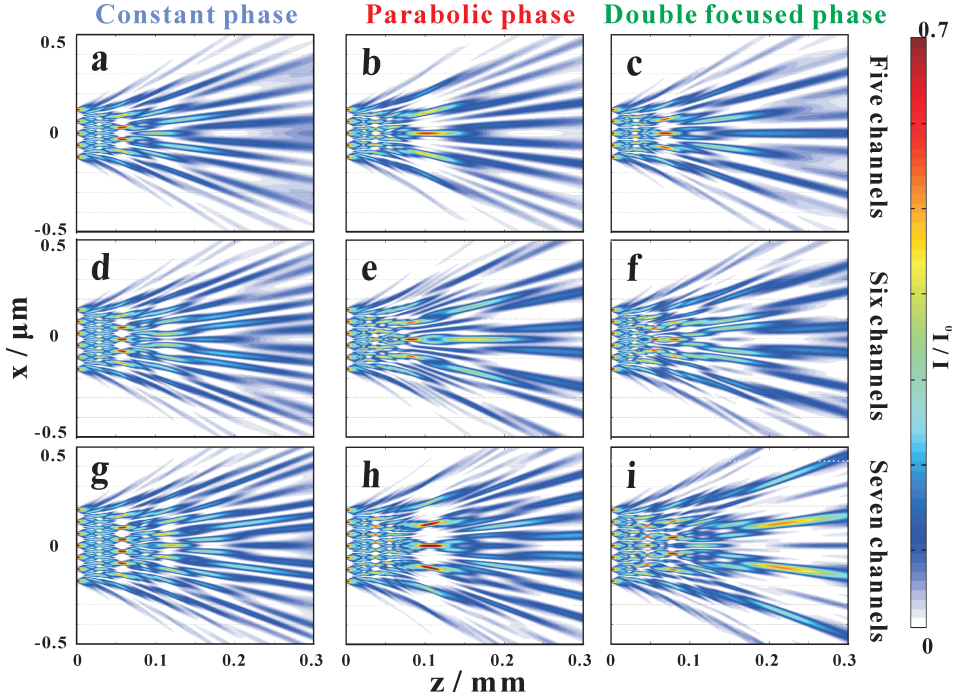
Figure 1.7: *Multi-beam interferences with different phase profiles. The multi-beam interference in free space is controlled by using different phase profiles: (a, d, g) constant phase profile (flat), (b, e, h) a parabolic phase profile and (c, f, i) a "double focused phase" profile; Using the similar phase profiles as shown in Fig. 1.6, the corresponding interference patterns for five-channels (a, b, c), six-channels (d, e, f) and seven-channels (g, h, i) are also presented.*

simulation, based on free space propagation using the parabolic wave equation [20]. To tailor a near-field with e.g. a quasi-focal spot, we keep the central channel's phase unchanged, but decrease the phases φ_i symmetrically towards the outside, thus creating a convex lens for the x-ray beam; see Fig. 1.7(b). Alternatively, a double quasi-focus as shown in Fig. 1.7(c) is also possible. Of course, as shown in Fig. 1.7(a-c and g-i), we find the output efficiency increases for all phase profiles with the number i of channels. To further shed light on the **waveguide array (WGA)**, we also compare it to a simple **periodic waveguide multilayers (WGM)**, as a 'control structure'. The WGA has tailored width d_i ($i = 1, ..., 7$) and the corresponding cladding layer thicknesses c_j ($j = 1, ..., 7$) and c_{j+1} for each waveguide. In contrary, the WGM is a periodic arrangement of the same waveguide structure with constant guiding layer thickness d and cladding layer thickness c.

Table 1.1: *The theoretical Mo/C WGA and WGM designed layer thicknesses are shown.*

Layer Nr.	c_8	d_7	c_7	d_6	c_6	d_5	c_5	d_4	c_4	d_3	c_3	d_2	c_2	d_1	c_1	Sub
Layer name	Mo top	C	Mo	C	Mo	C	Mo	C	Mo	C	Mo	C	Mo	C	Mo	Ge Sub
Waveguide array (WGA)																
Layer thickness /nm	50.0	4.0	56.0	6.2	53.8	7.6	52.4	8.0	52.4	7.6	53.8	6.2	56.0	4.0	50.0	
Periodic waveguide multilayer (WGM)																
Layer thickness /nm	50.0	8.0	52.0	8.0	52.0	8.0	52.0	8.0	52.0	8.0	52.0	8.0	52.0	8.0	52.0	
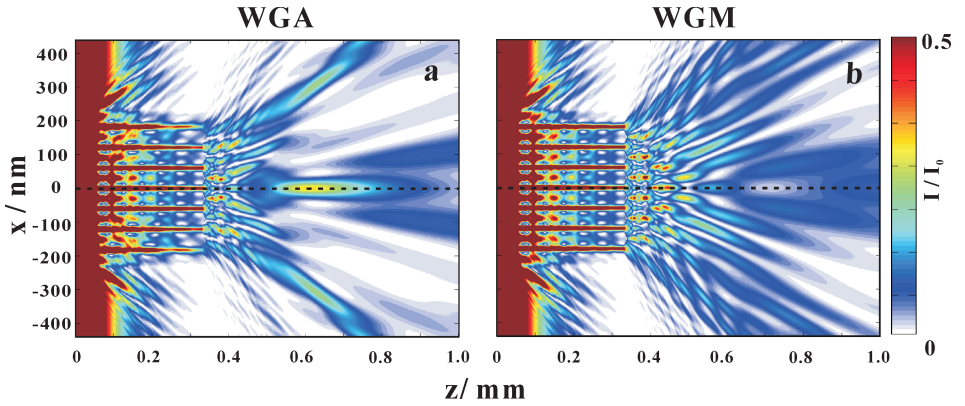
Figure 1.8: *Simulations of the WGA and WGM. Based on the parameters from Table 1.1, field propagations in the (a) WGA and (b) WGM are simulated in the near-field by FD calculations with the incoming plane wave of unit intensity for 19.9 keV photon energy.*

The layer structures of Mo/C WGA and WGM are tabulated in Table 1.1. The corresponding source code is in App. A.1.2.

Fig. 1.8 presents the simulation of electromagnetic field inside the WGA and WGM using the FD algorithm with an incoming plane wave of unit intensity for 19.9 keV photon energy. The simulations are based on the designed parameters of seven C layers and eight Mo layers from Table 1.1. The waveguide length $L = 0.28$ mm is used for the WGA and WGM. Note that in the figure, the pixel sizes in x and z directions are 1 nm and 0.1 μm, respectively. To illustrate the field modulating effects, which can be achieved by a symmetrical variation of waveguide width d_i, Fig. 1.8(a) shows a simulation for the WGA consisting of different guiding layer thickness d_i and cladding layer thickness c_j to control

the exit phase φ_i. The WGA exhibits a near-field distribution with a quasi-focal spot of $FWHM$ = 37.2 nm. For controlled phase φ_i in the WGA structure, a simple periodic structure WGM is used as a reference. The WGM only presents a regular and periodic field distribution in free space, as shown in Fig. 1.8(b). Therefore, It is necessary to further characterize the far-field measurements of WGA (see Chapter 2), and compare the differences between WGA and WGM (see Chapter 3). The corresponding FD simulation source code is in App. A.1.3.

1.2.2 Resonant beam couplers

In the last section, we have discussed the guided mode propagation in the FCs. The FC, i.e. straight waveguide, consists of one guiding layer with low density, sandwiched between two high density cladding layers. An incoming beam is coupled in front of the structure, guided within a guiding layer of length L, and then coupled out in the exit plane. In this section, we will discuss a different coupling method, the resonant beam couplers (RBCs) [35, 42–44]. The guided modes are resonantly excited by shining a parallel beam onto the waveguide under grazing incidence using a precisely controlled incidence angle α_i for each guiding mode.

 The IMD software [45] was used to simulate x-ray intensity inside a RBC structure, as demonstrated earlier [30, 35, 42]. Fig. 1.9(a) shows the simulated x-ray reflectivity with the structure of Ni (5 nm) /C (50 nm) /Ni (50 nm) on a GaAs substrate as a function of incident angle α_i in the range from 0.1° to 0.3° for 13.8 keV photon energy. Note that both the incoming beam size and RBC length L are treated as infinite. The sharp dips in the x-ray reflectivity between the critical angles α_c^C of C and α_c^{Ni} of Ni evidence the excitation of the TE_0 , TE_1 , TE_2 and TE_3 modes inside the cavities. The corresponding calculated electric field intensity distribution as a function of α_i and the depth in x direction can be conveniently illustrated in the form of two-dimensional contour plots, as represented in Fig. 1.9(b). The characteristic antinodes of the x-ray standing waves corresponding to electric modes (TE_m, $m = 0, ..., 3$) of RBC structure can be easily located. Fig. 1.9(c, d) shows the equivalent plots for the multi-guide RBCs with $[Ni$ (5 nm)/C (50 nm)]$_3$ /Ni (50 nm) on GaAs substrate. The coupling modes result in a splitting and lifting of degeneracy, as first discussed in [30]. For the infinite samples and beams, the cusp arises since photons are more likely to get absorbed when they are coupled into the structure, rather than being reflected at the top. For the finite beams and samples, if the footprint reaches the edge of RBC, the guided beams exit at the side.

Fig. 1.10(a) shows a sketch of RBC structure with an incoming beam with fi-
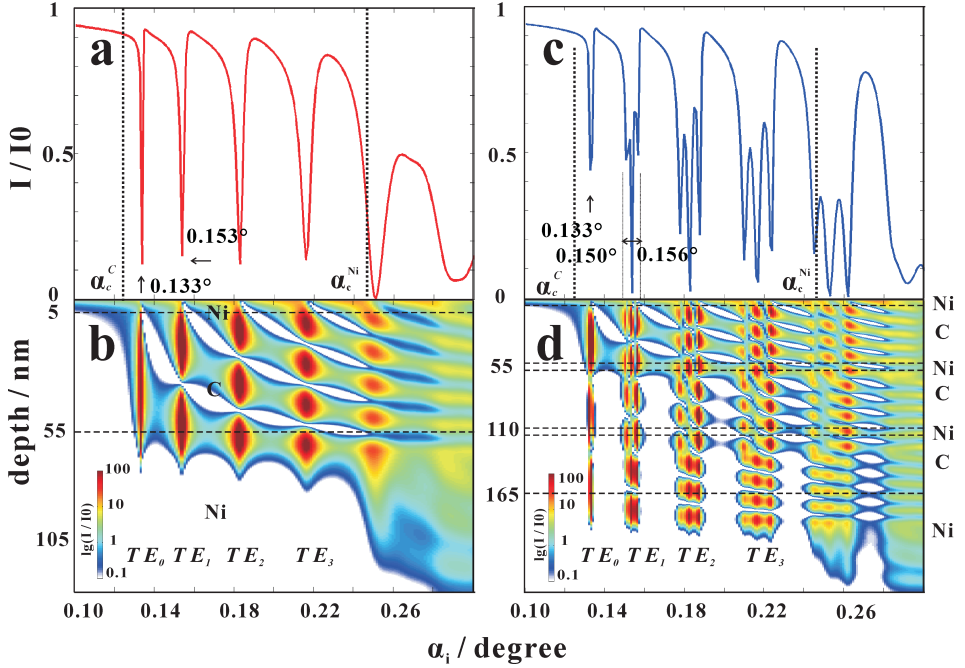
Figure 1.9: *Guiding properties of a RBC with infinite beam size.(a) Simulated reflectivity with Ni (5 nm) /C (50 nm) /Ni (50 nm) on a GaAs substrate as a function of α_i for 13.8 keV photon energy. The critical angles of C (α_c^C) and Ni (α_c^{Ni}) are shown as black dotted lines.(b) Calculated field intensity in the RBC in logarithmic scale. (c, d) The corresponding plots for a multi-guide RBCs structure with three C guiding layers and four Ni cladding layers. The modes TE_m observed at different α_i are labeled. Note that the simulations assume an infinite beam and structure in the IMD software.*

nite beamsize. With similar structure of planar waveguide as shown in Fig. 1.5(a), the guiding layer with index n_1 is sandwiched between two asymmetrical cladding layers with index n_2. The bottom cladding layer is normally very thick, compared to the thinned top one (< 10 nm). An incoming beam with finite beam size hits the RBC surface, e.g. the hitting point P_0. Some parts of the beam are reflected at that position, while some parts penetrate through the thinned top cladding layer, and propagate inside the guiding layer with the internal travelling angle α_{int}. As we know [30, 38], $0 < \alpha_{int} < \alpha_c^{n_1,n_2}$, where

$$\alpha_{int} = \frac{\kappa}{\beta^m}, \tag{1.28}$$

$\alpha_c^{n_1,n_2}$ is the critical angle between the materials n_1 and n_2, m is the different excited modes. Due to the field propagation inside the guiding layer, only a part of
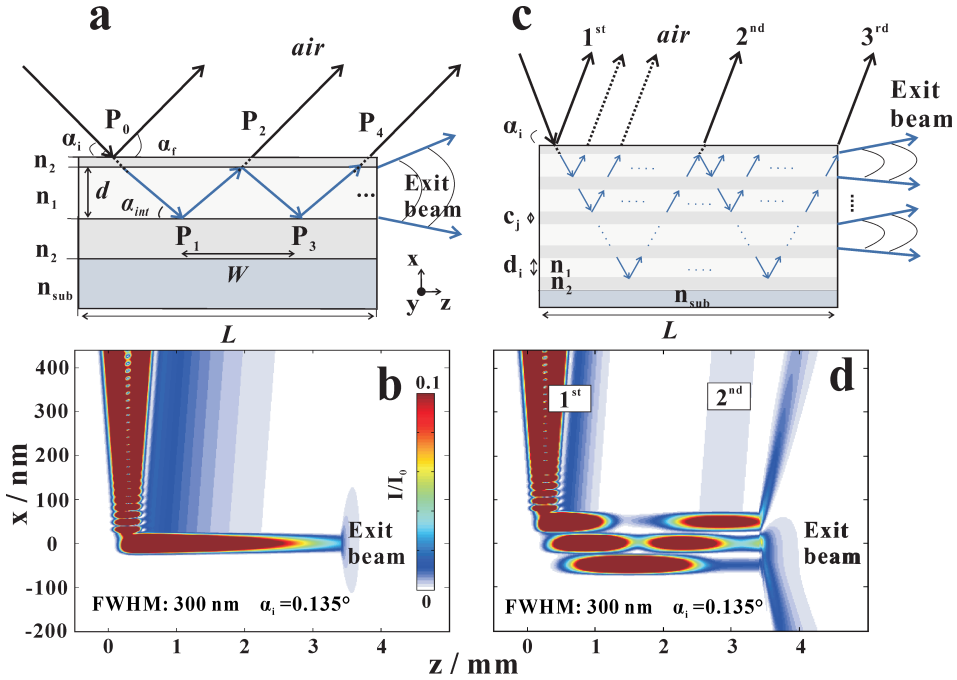
Figure 1.10: *Guiding properties of a RBC with finite beam size. (a) A simple sketch of a RBC, consisting of one guiding layer (n_1) and two cladding layers (n_2), deposited on the substrate (n_{sub}). An incoming beam hits the RBC surface under an incidence angle α_i. It is then partly transmitted into the guiding layer but also reflected from the surface. (b) The near-field distribution of single RBC with one C layer and two Ni layers on the GaAs substrate is calculated with the incoming beam size $FWHM = 300\,nm$ at $\alpha_i = 0.135°$ for 13.8 keV photon energy. (c, d) The corresponding plots for a multi-guide RBCs structure with three C layers and four Ni layers are presented. In the schematic (d), the incoming beam with a beam size $FWHM$ is coupled into the multi-guide RBCs structure. If the beam footprint on the surface of RBCs structure is small enough, that could exit several reflected beams, e.g. the 1st, 2nd,..., reflected beams. Note that the FD simulations shown in (b, d) assume $FWHM = 300\,nm$ and length $L = 3.5\,mm$.*

the beam can exit from the surface at the points $P_2, P_4, \dots$. Based on this analysis, Fig. 1.10(b) shows the corresponding simulation of Ni (5 nm) /C (50 nm) /Ni (50 nm) RBC structure on a GaAs substrate with $FWHM = 300$ nm at $\alpha_i = 0.135°$ for 13.8 keV photon energy. At the incident angle α_i, the photons "get trapped" under the resonance conditions in the guiding layer, propagating parallel to the surface over an active coupling length. Fig. 1.10(c, d) shows the equivalent plots for the multi-guide RBCs with three guiding layers [Ni (5 nm)/C (50 nm)]$_3$ /Ni (50 nm) on GaAs substrate. From the simulations, we can find whether the beam footprint is small enough, and whether are several beams exiting from

surface in both single and three guiding layers RBCs. In Fig. 1.10(d), when the first guided mode forms in the top layer, the wave distribution is more like the phenomena as shown in Fig. 1.10(b). With another guided mode generating in the top channel, the 2nd reflected beam comes out with a large displacement along z, constituting an exceptionally large lateral offset, a kind of giant Goos-Hänchen effect.

Goos-Hänchen effect
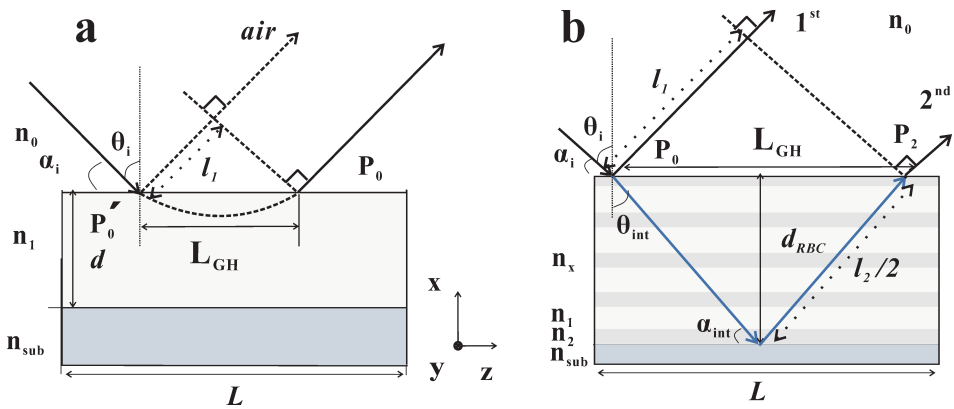
Figure 1.11: *The Goos-Hänchen shift at an interface and a RBC structure. (a) The sketch of Goos-Hänchen effect at an interface between air and a material n_1, with the Goos-Hänchen shift L_{GH} at an incident angle α_i. (b) presents a kind of generalized Goos-Hänchen effect occurring in a RBC structure, observable when illuminated with by a finite-size beam. The RBC structure consists of several guiding layers with n_1 and cladding layers with n_2. The total thickness d_{RBC}, and the Goos-Hänchen shift L_{GH} inside the RBC is represented for an incident angle α_i matching certain mode conditions. The path lengths of the 1st and 2nd reflected beams are l_1 and l_2, respectively.*

The Goos-Hänchen effect denotes a lateral shift when an incident beam is totally reflected from a planar interface between two dielectric materials: the reflected beam is shifted laterally along the surface by a distance L_{GH} (the Goos-Hänchen shift), i.e. a parallel shift to the reflecting interface. [46–54]. Fig. 1.11 sketches the Goos-Hänchen effects at an interface (a) and a RBC structure (b) during the field propagation.

Fig. 1.11(a) [48, 50, 52, 53] shows the Goos-Hänchen effect at an interface between a material with n_1 and air with n_0. When an incident beam with angle α_i hits on the surface of the material n_1, the reflected beam is not immediately reflected into air at point P_0'. With the Goos-Hänchen shift L_{GH}, the real reflected

beam exits at the point P_0 and experience some phase shifts. In this diagram, we assume φ_r is the reflection phase and $k_z L_{GH}$ is the phase accumulated during that propagation. Based on Artmann's model [48], φ_r is given by

$$\varphi_r = -k_z L_{GH} = -\frac{2\pi n_0}{\lambda} sin\theta_i L_{GH}, \tag{1.29}$$

where k_z is the z component of the wave vector, $\theta_i = \pi/2 - \alpha_i$, and n_0 is the index of air. Thus the phase shift $d\varphi_r$ is given by

$$d\varphi_r = -d(k_z L_{GH}) = -\frac{2\pi n_0}{\lambda} cos\theta_i L_{GH}(d\theta_i), \tag{1.30}$$

Then L_{GH} is presented as

$$L_{GH} = -\frac{\lambda}{2\pi n_0 cos\theta_i}\left(\frac{d\varphi_r}{d\theta_i}\right) = \frac{\lambda}{2\pi n_0 sin\alpha_i}\left(\frac{d\varphi_r}{d\alpha_i}\right). \tag{1.31}$$

Without considering the penetrated depth into the interface, the Goos-Hänchen time τ_{GH} is given by

$$\tau_{GH} = \frac{l_1}{v} = \frac{n_0}{c} sin\theta_i L_{GH} = -\frac{\lambda tan\theta_i}{2\pi c}\left(\frac{d\varphi_r}{d\theta_i}\right), \tag{1.32}$$

which c is the speed of light, $l_1 = sin\theta_i L_{GH}$ is the path length of the original reflected beam.

Fig. 1.11(b) [50, 53] illustrates a form of generalized Goos-Hänchen effect in the case of propagation inside a RBC with multilayer structure, consisting of several guiding layers with n_1 and cladding layers n_2. In this case, an incident beam with angle α_i hits on the surface. Some parts of the beam, denoted as 1st reflected beam, is reflected at that position P_0, while another part penetrate through the thinned top cladding layer, and propagates inside the guiding layers. Afterwards, a part of the beam, denoted 2nd reflected beam, can exit from the multilayer at the points P_2, which is laterally displaced by a significant distance of up to several millimeters can be regarded as a generalized Goos-Hänchen effect.

Because of the complex interfaces in the RBC structure, we can treat the entire structure as a single effective interface as presented in Fig. 1.11(a), in view of applying Artmann's theory. For this purpose, we can use Eq.(1.31) to calculate the displacement of the reflected beam, and present a phase curve as a function of α_i. Fig. 1.12 illustrates the comparison of the phase curves between the IMD calculation with infinite beam and the FD simulation ($FWHM = 300$ nm) for the Ni (5 nm)/C (50 nm) /Ni (50 nm) RBC on GaAs substrate for 13.8 keV photon energy. Fig. 1.12(a) shows the reflectivity (dark blue line) and corresponding
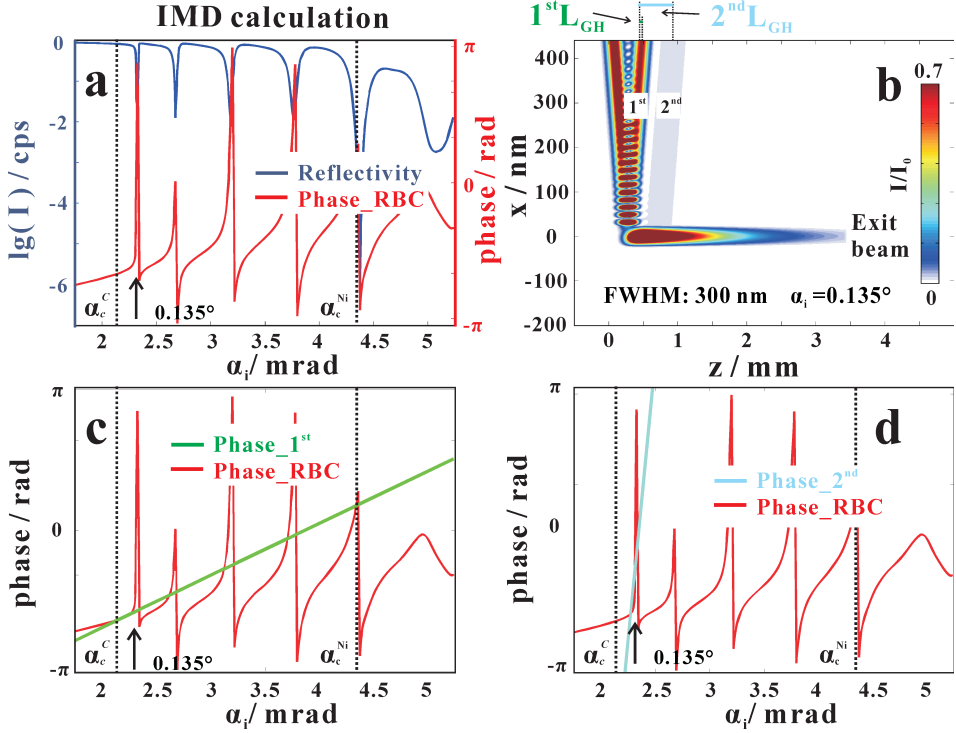
Figure 1.12: *Characterization of the Goos-Hänchen effect. (a) Using IMD calculates the reflectivity (dark blue line) and corresponding phase curve (red line) as a function of α_i for the Ni (5 nm)/C (50 nm) /Ni (50 nm) RBC on GaAs substrate for 13.8 keV photon energy. The critical angles of C (α_c^C) and Ni (α_c^{Ni}) are shown as black dotted lines. (b) The corresponding field intensity is simulated with $FWHM = 300$ nm at $\alpha_i = 0.135°$ by using FD simulations. The RBCs structure can exhibit several reflected beams, the 1st and 2nd reflected beams, with the Goos-Hänchen shifts $1^{st} L_{GH} = 6.9 \,\mu m$ and $2^{nd} L_{GH} = 0.454$ mm, respectively. Based on Eq.(1.31), the phase shift curves of 1st and 2nd reflected beams as a function of α_i are presented in (c) green line and (d) light blue line, respectively.*

phase curve (red line) as a function of α_i in the range of 0.1° to 0.3° (1.75 mrad to 5.25 mrad), using IMD software. Fig. 1.12(b) present the FD simulations of the RBC with $FWHM = 300$ nm at $\alpha_i = 0.135°$ (*on mode*). Based on the simulation, we obtain the Goos-Hänchen shifts, $1^{st} L_{GH} = 6.9 \,\mu m$ and $2^{nd} L_{GH} = 0.454$ mm, of 1st and 2nd reflected beams, respectively. Using Artmann's model as presented in Eq.(1.31), the phase curves of 1st (green line) and 2nd (light blue line) reflected beams are compared with the one (red line) from the IMD calculation, as shown in Fig. 1.12(c) and (d), respectively. In the case of 1st reflected beam (Fig. 1.12(c)), the phase curve for the *on mode* case is similar to the one

in *off mode* case, which is matched in the range from 2.07 mrad to 2.22 mrad. In the case of 2nd reflected beam in Fig. 1.12(d), the phase curve's slope of the 2nd reflected beam is significantly increased with $2^{nd} L_{GH}$. Although the slope has a little difference with the one in the TE_0 mode from the IMD calculation, the results illustrate some interesting phenomena: First, if we gather the phases of all reflected beams in the FD simulation, the phase curves in the TE_0 mode might be similar as the one in IMD calculations. Second, we can extent use the Artmann's model to illustrate the Goos-Hänchen effect in the RBC structure. Third, with multi-guide RBC structure, the significant differences in the phase curves of different reflected beams can be observed.

To sum up, Fig. 1.11 and 1.12 shows the Goos-Hänchen effects during the wave propagation at an interface and RBC structure. With the influence of guided mode, the waveguide radiation can be regarded as a superposition of the Goos-Hänchen shift in the RBC structure, resulting in a enormous shift in the reflected beam of several millimeters. Note that this thesis only performs basic analysis and assumption, considering the Goos-Hänchen shift in an RBC structure. Further numerical and detailed analysis are the obvious extensions for future work.

Based on the simulation in Fig. 1.10(d), it has illustrated the effect of the beam footprint s on the surface. To clearly observe two reflected beams, s has to be smaller than the beam offsets o arising from the Goos-Hänchen effect, associated with the multiple reflections and coupling into modes. Several important factors, i.e. incident angle α_i (see Fig. 1.13), $FWHM$ (see Fig. 1.14, 1.15) and RBC structure (see Fig. 1.16, 1.17), influence the multiple reflections, as discussed in the following.

Fig. 1.13 presents the FD simulations for 13.8 keV photon energy, and incoming Gaussian beam with beam size $FWHM$ = 300 nm at different incident angles α_i, carried out for (a-d) single RBC with Ni (5 nm)/C (50 nm) /Ni (50 nm), and (e-h) the multi-guide RBCs with $[Ni$ (5 nm)/C (50 nm)$]_3$ /Ni (50 nm). The total length of RBCs along z is L = 3 mm in the simulations. The standing wave on the surface forms an interference zone [55] in all RBCs structures. The phenomena of multiple reflections in the multi-guide RBCs are much more obvious than the ones in single RBC, e.g. as shown in TE_0 mode of Fig. 1.13(a) and (e). The guided modes are resonantly excited in the different channels at different positions along z. When the guided mode forms in the top channel, the 2nd reflected beam comes out from the surface. In Fig. 1.13(g, h), the simulations illustrate the importance of a sufficiently focused incoming beam to clearly separate the reflected beams. It is to be noted that the maximum amplitude values of the 1st and 2nd reflected beams are almost similar. From these simulations,
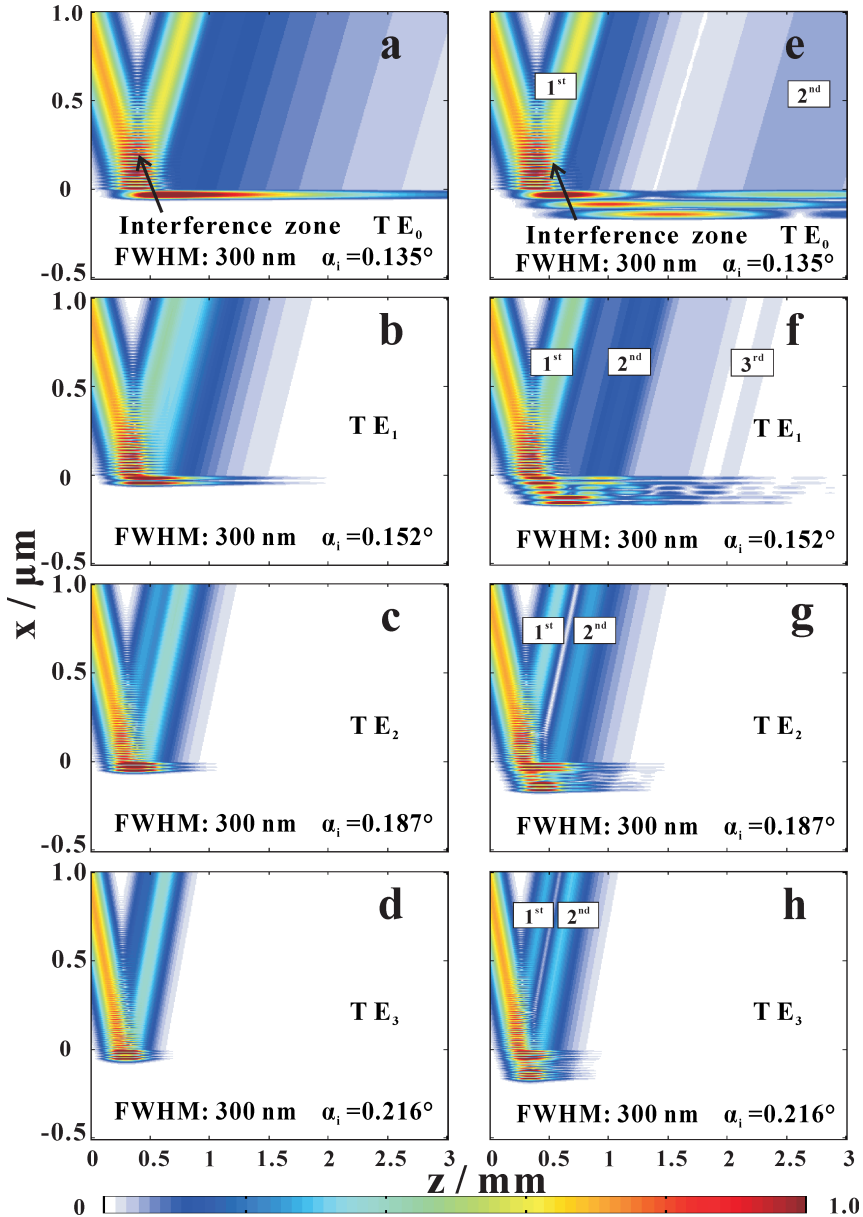
Figure 1.13: *Simulations of the Ni-C RBC system with single guiding layer (left column) and three guiding layers (right column) for different incident angles. Simulations of mode excitation with FWHM=300 nm for 13.8 keV photon energy. The near-field distributions for a single guiding layer RBC at (on-mode) conditions: (a) TE_0 at $\alpha_i = 0.135°$, (b) TE_1 at $\alpha_i = 0.152°$, (c) TE_2 at $\alpha_i = 0.187°$ and (d) TE_3 at $\alpha_i = 0.216°$ are calculated. (e-h) The corresponding plots for multi-guide RBCs with three guiding layers.*
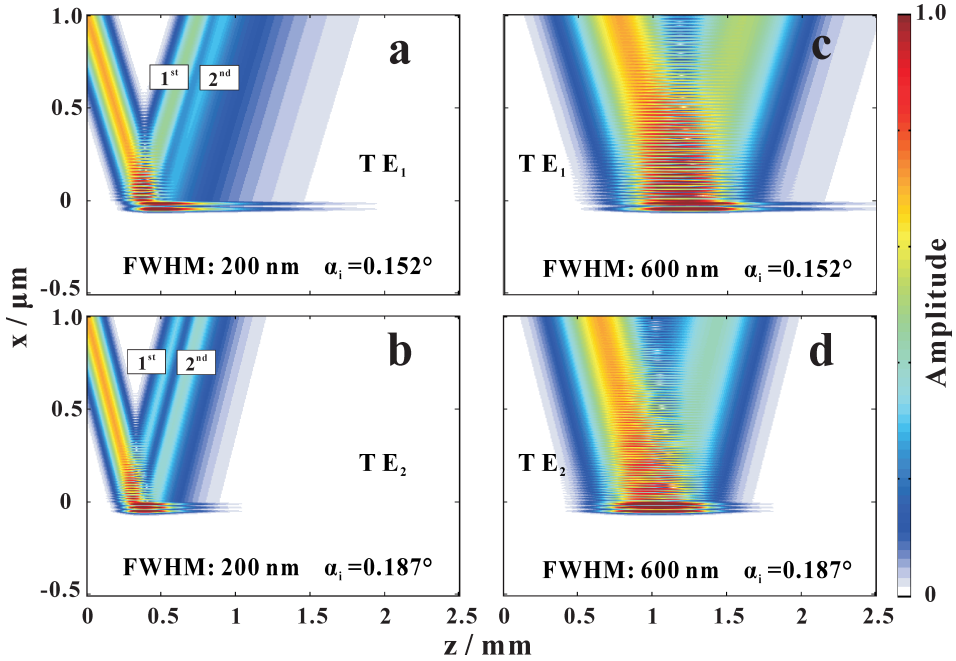
Figure 1.14: *Simulations of the RBC with single guiding layer for different FWHM. Simulation of mode excitation for single RBC structure for 13.8 keV photon energy. The near-field distributions are calculated with $FWHM = 200$ nm at (a) $\alpha_i = 0.152°$, (b) $\alpha_i = 0.187°$, and $FWHM = 600$ nm at (a) $\alpha_i = 0.152°$, (b) $\alpha_i = 0.187°$, respectively.*

we can conclude that multi-guide RBCs can result in multiple reflected beams, linked to the incidence angles α_i of mode excitation.

Fig. 1.14 presents the field distributions, carried out for the single RBC with the same parameters simulated in Fig. 1.10(b) for 13.8 keV photon energy. The near-field distributions are calculated in two cases: $FWHM = 200$ nm with (a) the TE_1 mode at $\alpha_i = 0.152°$, (b) the TE_2 mode at $\alpha_i = 0.187°$, and $FWHM = 600$ nm with (c) the TE_1 mode at $\alpha_i = 0.152°$, (d) the TE_2 mode at $\alpha_i = 0.187°$. For $FWHM = 200$ nm, the separated reflected beams exit from the surface, especially in Fig. 1.14(b). While for $FWHM = 600$ nm, only the 1st reflected beam is observed due to larger beam footprint s on the surface.

Fig. 1.15 shows the simulations of multi-guide RBCs with three guiding layers, again with different $FWHM$ from 200 nm to 1800 nm. The multiple reflections are only observed when $FWHM \leq 1$ μm as shown in Fig. 1.15(a, b, c). When $FWHM > 1$ μm (Fig. 1.15(d, e, f)), the 2nd reflected beams begin to involve into the 1st reflected beams. From the simulations, we can find that the multiple
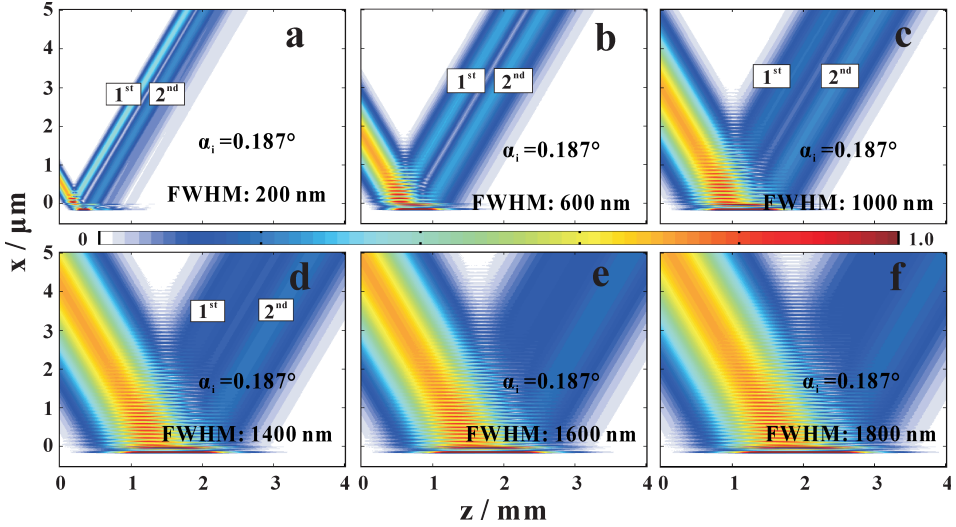
Figure 1.15: *Simulations of the RBC with three guiding layers for different FWHM. Using the similar process, the near-field distributions for multi-guide RBCs with three guiding layers are simulated at the $\alpha_i = 0.187°$ with increasing of FWHM (a) 200 nm, (b) 600 nm, (c) 1000 nm, (d) 1400 nm, (e) 1600 nm and (f) 1800 nm.*

reflections in the multi-guide RBCs with three guiding layers occur only at the proper α_i values required for mode excitation with finite-size (sub-μm) beams. Fig. 1.16 presents the field propagations in multi-guide RBCs with (a, b) two guiding layers, (c, d) four guiding layers, (e, f) five guiding layers, and (g, h) seven guiding layers. Fig. 1.16(a) shows that the guided modes are resonantly excited in the RBCs with two guiding layers with $FWHM = 300$ nm for the TE_0 modes at $\alpha_i = 0.135°$. When the amplitude of guided mode becomes the relative maximum in the top channel, the 2nd reflected beam comes out with a large displacement along z. Using $FWHM = 600$ nm for the TE_1 mode at $\alpha_i = 0.152°$ in the simulation, only two reflected beams are observed. Similar phenomena happened also in the other structures, but with different lateral shifts between two reflected beams on the surface as shown in Fig. 1.16(c-h). Fig. 1.17 presents an extended comparison of multi-guide RBCs with different guiding layers in the near-field distributions. Fig. 1.17(a) presents a sketch of multi-guide RBCs similar to that shown in Fig. 1.10(c). If the illuminated spot size on the surface s and lateral displacement o become of comparable size, the multiple reflected beams in the near-field are well separated. Fig. 1.17(b) gives the FD simulation of amplitude distribution in the near-field. An incoming beam with $FWHM = 600$ nm at incident angle $\alpha_i = 0.187°$ hits on the sur-
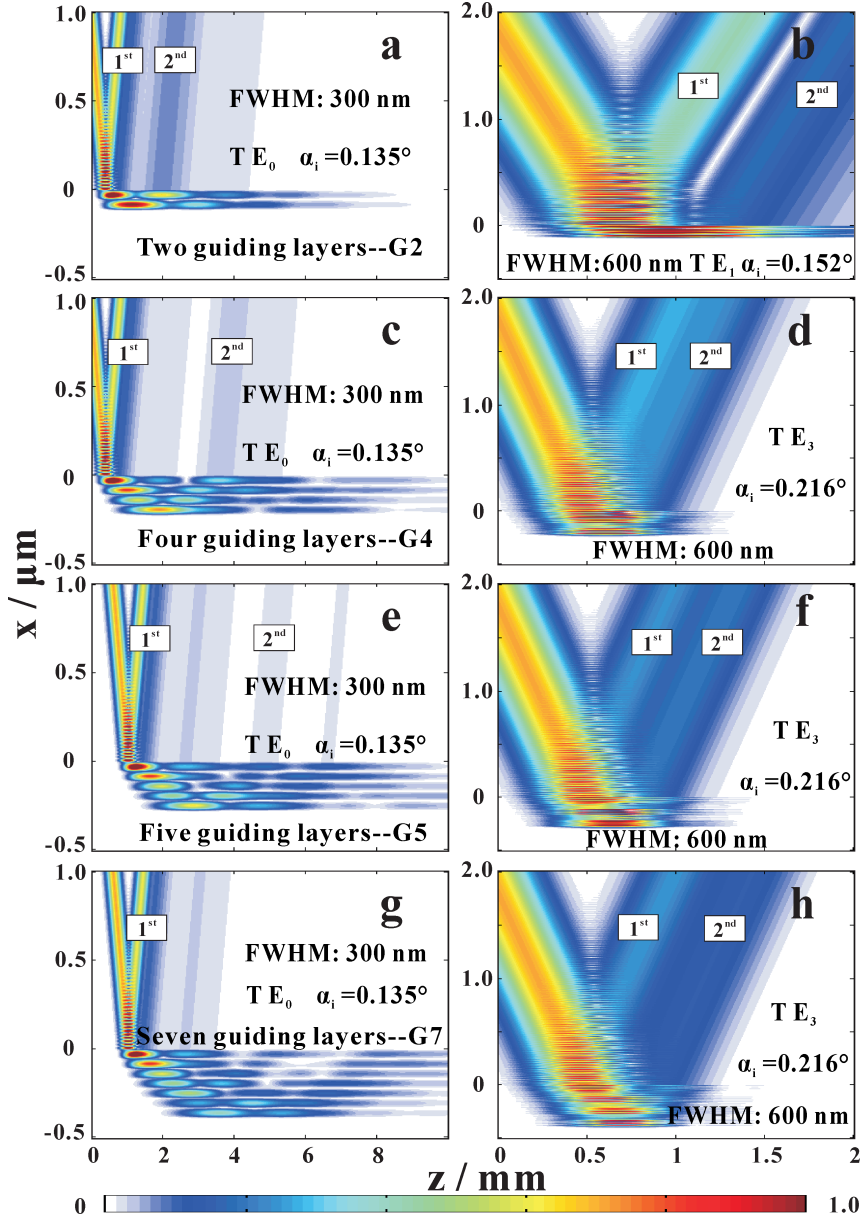
Figure 1.16: *Simulations of the RBCs with variable guiding layers. (a, b) the multi-guide RBCs with two guiding layers (G2): the near-field distributions with $FWHM = 300$ nm at $\alpha_i = 0.135°$ and $FWHM = 600$ nm at $\alpha_i = 0.152°$; (c, d) the multi-guide RBCs with four guiding layers (G4): the near-field distributions with $FWHM = 300$ nm at $\alpha_i = 0.135°$ and $FWHM = 600$ nm at $\alpha_i = 0.216°$; (e, f) the multi-guide RBCs with five guiding layers (G5): the near-field distributions with $FWHM = 300$ nm at $\alpha_i = 0.135°$ and $FWHM = 600$ nm at $\alpha_i = 0.216°$; (g, h) the multi-guide RBCs with seven guiding layers (G7): the near-field distributions with $FWHM = 300$ nm at $\alpha_i = 0.135°$ and $FWHM = 600$ nm at $\alpha_i = 0.216°$.*
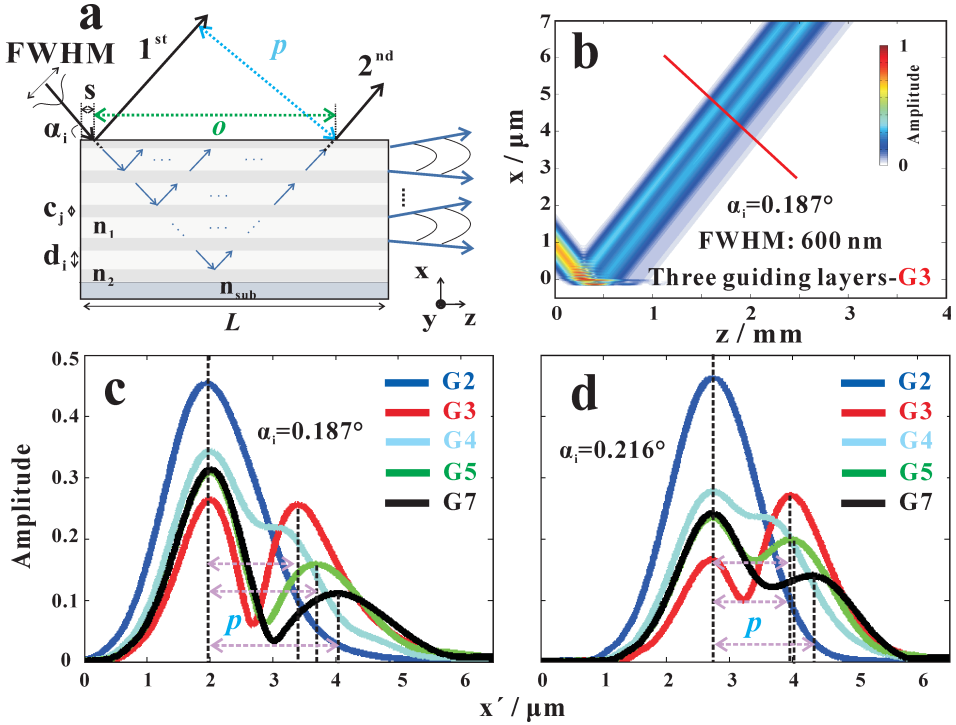
Figure 1.17: *Differences in the RBCs with variable numbers of guiding layers. In the schematic of (a) the incoming beam with a beam size $FWHM$ is coupled into the multi-guide RBCs structure, illuminating the surface over a size $s = FWHM/sin(\alpha_i)$. If $FWHM$ and s are sufficiently small, the RBCs structure can exhibit several reflected beams. Some Important parameters characterizing the 1st and 2nd reflected beams are the beam offsets on the surface o (green dash lines), and the distance between two beams p (blue dash lines). (b) The near-field distributions are simulated by FD simulation for the theoretical RBCs parameters [Ni (5 nm)/C (50 nm)]_3 /Ni (50 nm) on GaAs substrate (G3) for the experimental photon energy 13.8 keV, $\alpha_i = 0.187°$ and beam size $FWHM = 600$ nm. Simulated near-field amplitude in the plane with different numbers of guiding layers indicated by the red line in (b) for (c) $\alpha_i = 0.187°$ and (d) $\alpha_i = 0.216°$ in the relevant multi-guide RBCs with different guiding layers.*

face of multi-guide RBCs with three guiding layers. The amplitude of reflected beam is collected at a certain reference plane along x' (red line, orthogonal to the reflected beam). Fig. 1.17(c) shows the comparison of amplitude distributions along x' at $z = 2$ mm with incident angle $\alpha_i = 0.187°$ of different RBCs structures. Fig. 1.17(d) presents the comparison of the similar distributions along x' at $z = 1.5$ mm with incident angle $\alpha_i = 0.216°$ of different RBCs structures. In these plots, the distances between two beams p are probably increased with the numbers of guiding layers, as shown in the purple dash lines. It is to be

noted that the maximum values of two reflected beams (1st and 2nd) are almost equal in the multi-guide RBCs structure with three guiding layers at $\alpha_i = 0.187°$, which makes this configuration attractive for beam-splitter and delay applications. The corresponding source code is in App. B.1.1.

To sum up, FD simulations show that multi-guide RBCs structures can generate multiple reflections on the surface. With specially designed structures, proper α_i for mode excitation and finite-size (sub-μm) beams, two reflected beams with same amplitudes in the near-field can be achieved. The corresponding far-field analysis is discussed in Chapter 4, using the simulated source code as shown in App. B.1.2.

1.3 Simulation and reconstruction of wave propagation

This section describes two different methods: finite-difference simulation in subsection 1.3.1 and phase retrieval methods in subsection 1.3.2, characterizing the near-field distributions in the x-ray waveguide.

1.3.1 Finite-difference simulation
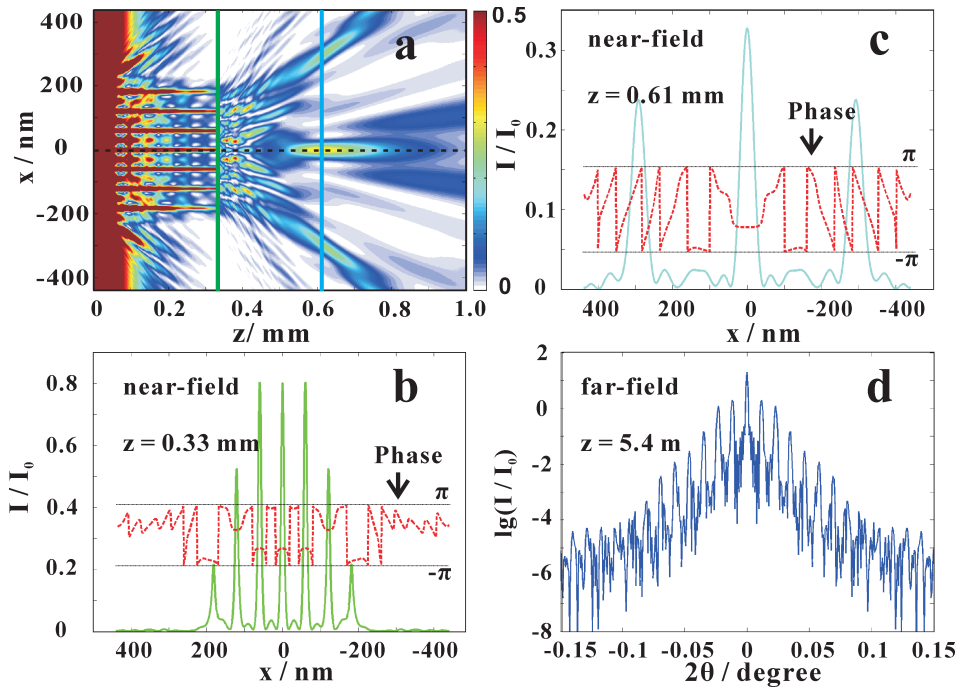
Figure 1.18: *FD simulations. (a) The field propagation is calculated with the parameters as shown in Table 1.1 inside and outside the WGA by using the FD method. The simulated near-field amplitude (color line) and phase (red dash line) are presented in the different planes along z direction: (b) the green line in the exit plane and (c) the light blue line in the quasi-focal plane. (d) The corresponding far-field is also shown.*

We use the finite-difference (FD) method to design the waveguides and the corresponding experiments [20, 22, 25, 29, 37, 38, 56, 57]. To this end, the precise layer structure is used to simulate the field propagation both inside and outside the waveguide. Firstly, we can collect the wave-field information at the exit plane or any other plane in the near-field, and then transform the near-field

information to the far-field pattern, using a Fourier transformation. Finally, the simulated far-field can be used to compare with the experimental one.

As mentioned in subsection 1.1.1, the parabolic wave equation in x and z directions is expressed as

$$\frac{\partial u(x,z)}{\partial z} = C\frac{\partial^2 u(x,z)}{\partial x^2} + D(x,z)u(x,z), \tag{1.33}$$

which the $C = -i/2k$, $D = -ik[n^2(x,z)-1]/2$. For the Crank-Nichelson scheme [20,37,58], the derivative expressions with approximately equivalent difference quotients are used in x and z direction. Using $u_i^n = u(x_i,z_n)$ and $D_i^{n+1/2} = D(x_i,z_{n+1/2})$ into Eq.(1.33),

$$\frac{u_i^{n+1}-u_i^n}{\Delta z} = \frac{C}{2(\Delta x)^2}[(u_{i-1}^n-2u_i^n+u_{i+1}^n)+(u_{i-1}^{n+1}-2u_i^{n+1}+u_{i+1}^{n+1})]+\frac{D_i^{n+\frac{1}{2}}}{2}(u_i^{n+1}+u_i^n), \tag{1.34}$$

The xz plane can be divided into a finite number of grid points $((M_x+1)\times(2M_z+1))$, which

$$x_i = i\Delta x, i = 0,1,...,M_x, \tag{1.35}$$

$$z_n = n\Delta z, n = 0,\frac{1}{2},1,\frac{3}{2},...,M_z. \tag{1.36}$$

With the boundary conditions:

$u(x,0) = u_0(x,0)$: the wave field at the front face of planar waveguide;

$u(x_0,z) = u_0(x_0,z)$: the lower boundary in the cladding layer far away from the guiding layer;

$u(x_{M_x},z) = u_0(x_{M_x},z)$: the upper boundary in the cladding layer far away from the guiding layer.

Therefore, we can calculate u_i^{n+1} from u_i^n step by step, and then present the field propagation in the WG. Fig. 1.18(a) presents the field propagation inside and outside the Mo/C WGA for 19.9 keV photon energy, with the parameters as tabulated from Table 1.1. Afterwards, the amplitude and phase informations can be collected in the exit plane (Fig. 1.18(b)) and the quasi-focal plane (Fig. 1.18(c)). Using Fourier transform [59], the different near-field planes result in the same far-field curve as shown in Fig. 1.18(d). Therefore, we can compare the calculated far-field with the experimental one to estimate the WGA structure and the near-field distributions. The author of this thesis first wrote an

own FD simulation code (Matlab), but later used the finite-difference software (C++) and PyPropagate software written at the Institute for X-ray Physics by Lars Melchior [60], which was used for all presented results. Using this package, numerous scripts for different geometries were written in this thesis. The most important script is shown in App. A.1.3.

1.3.2 Phase retrieval

Contrary to the method mentioned in the last section, where the near-field distribution was calculated by FD simulation in a WGA model, this section uses the phase retrieval method to invert experimental far-field data and thereby to characterize the near-field. The far-field intensity of a wave field diffracted from an object plane can be measured by a higher resolution detector without the phase information. Using phase retrieval method, the amplitude and phase in the object plane can be reconstructed, enabling a direct visualization of the near-field interference pattern. Three different, well established phase retrieval algorithms are used to reconstruct the wave in the object plane from the measured far-field pattern: the error reduction (ER) algorithm [27, 61, 62], hybrid input-output (HIO) algorithm [61, 62] and the HIO+ER algorithm [63].

Error reduction (ER) algorithm

The ER algorithm relies on the support constraint to provide the missing data for phase retrieval. The algorithm is initialized with a guess of wavefield $u_k(x, y)$ in the object plane (xy), for the kth iteration. The iteration consists of forward-propagation (implemented numerically by a fast Fourier transform) to wavefield $U_k(X, Y)$ in the far-field detector plane (XY plane). The $U_k^{'}(X, Y)$ is formed from $U_k(X, Y)$ making the minimum changes to satisfy the amplitude constraint (measured data $M(x, y)$). The corresponding error can be expressed as [64]

$$\chi(U, M) = \sqrt{\frac{\sum |U - M|^2}{\sum |M|^2}}. \tag{1.37}$$

Then the $U_k^{'}(X, Y)$ is back-propagated to the object plane $u_k^{'}(x, y)$. With the support constraint,

$$u_{k+1}(x, y) = \begin{cases} u_k^{'}(x, y), & (x, y) \in S, \\ 0, & (x, y) \notin S, \end{cases} \tag{1.38}$$

where the support is given the region of S in the xy plane. Normally, the support S is selected in the exit field plane of the waveguide. Finally, a new estimate of

object plane $u_{k+1}(x,y)$ results in the next input of cyclic iteration. The aim of ER algorithm is to find a local minimum in the phase retreival problem. The ER source codes are in App. A.1.4.

Hybrid input-output (HIO) algorithm

By using the hybrid input-output (HIO) algorithm, a non-local search of a solution to the phase retrieval problem can be performed. The first four steps are the same for both the ER and HIO algorithms: assuming a trial wave field $u_k(x,y)$, forward-propagation to $U_k(X,Y)$, satisfying amplitude constraint to get $U_k^{'}(X,Y)$ and back-propagation to $u_k^{'}(x,y)$. The main difference is only in the support constraint step. The constraint is as a nonlinear system with input wave field $u_k(x,y)$, and the output wave field $u_k^{'}(x,y)$ at iteration k. The new $u_{k+1}(x,y)$ is formed as a linear combination of the input and output of the modulus constraint system [62]. Thus, the next input is expressed as

$$u_{k+1}(x,y) = \begin{cases} u_k^{'}(x,y) & (x,y) \in S, \\ \\ u_k(x,y) - \beta u_k^{'}(x,y) & (x,y) \notin S, \end{cases} \quad (1.39)$$

where $\beta \leq 1$ is typically chosen to be close to 1. The HIO method can avoid that $u_{k+1}(x,y)$ is trapped into the local minima. The HIO source codes are presented in App. A.1.4.

The HIO+ER algorithms falls somewhere in between the local minimizers (ER algorithm) and global minimizers (HIO algorithm). All three algorithms have different advantages and drawbacks. Depending on the sample and far-field measurements, the most suitable algorithm has to be tested. Due to the small errors and convincing patterns, we further compare the two supports using the ER and HIO algorithms in Chapter 3. The corresponding phase retrieval source codes are presented in App. A.1.4.

1.4 Fabrication and characterization

In this section, we present the fabrication process of multilayers and multilayer waveguides in subsection 1.4.1. Further, we introduce the in-house and synchrotron instruments used for characterization in subsection 1.4.2.

1.4.1 Fabrication
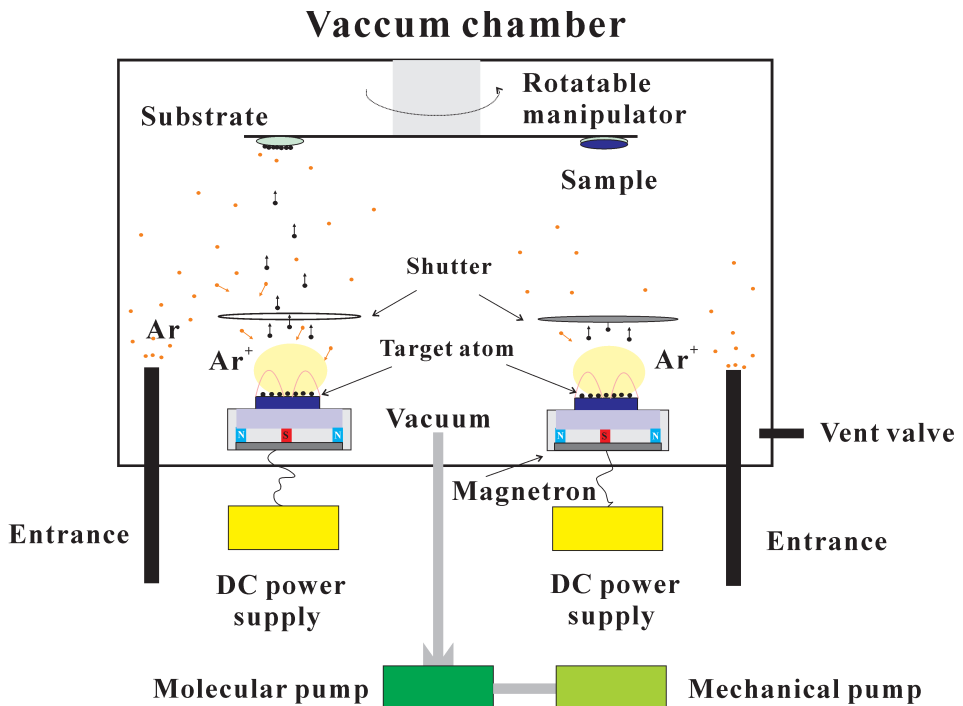
Figure 1.19: *Fabrication by sputtering. Sketch of a setup for DC magnetron sputtering.*

Direct-current (DC) magnetron sputtering is an extremely stable technique for the fabrication of multilayers with controlled layer thickness in the range of 0.2 nanometers [65–71]. Fig. 1.19 shows the sketch of a setup for the fabrication of a multilayer sample. The base pressure of the vacuum chamber is set to 1×10^{-4} Pa. The sputtering gas is argon (Ar) with a purity of 99.9999%, e.g. with a gas pressure of $2.00 \pm .02$ mTorr (0.266 Pa). With the DC power, a target on a magnetron can generate a magnetic trap for the argon ions (Ar^+). Putting the

target at a negative voltage attracts argon ions to the target. When the ions hit the target surface, the atoms of the target can escape from the surface, which go straight to a substrate forming a layer. Therefore, the layer thickness is determined by the sputtering speed (which is influenced by the voltage on the target and the argon gas pressure), distance from the target to substrate and the sputtering time on a substrate. To fabricate a multilayer sample, the shutters on top of the target could control different materials deposited on a substrate. Alternating the targets, a multilayer structure is formed. For this thesis, all samples were fabricated by the DC magnetron sputtering systems at the Institute of Precision Optical Engineering at Tongji University, China.

Figure 1.20: *WGA fabrication process. The schematic of different steps of the WGA fabrication and basic characterization.*

Fig. 1.20 presents the fabrication steps of a x-ray waveguide array [72]. Fig. 1.20(a): after multilayer sample deposition, an additional 120 nm thick Ni layer and absorbing capping Cr layer (3 nm) was deposited on both multilayer sample and Ge capping wafer.

Fig. 1.20(b): a thin $In52Sn48$ in the form of 25 μm thick ribbon (GPS Technologies GmbH, indalloy number 1E) is sandwiched between the Ni faces of multilayers a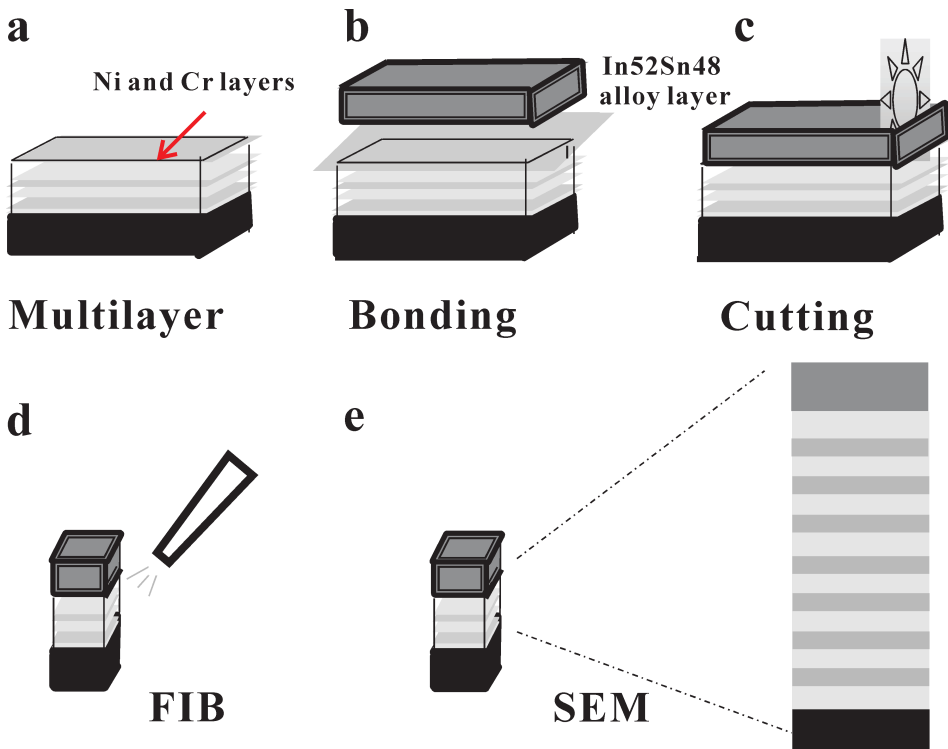nd Ge wafer in a vacuum oven at 250° for one hour. The WGA was cooled down to room temperature at a base pressure of 1×10^{-1} Pa.

Fig. 1.20(c): after the alloy bonding process, the sample is sliced to the designed length.

Fig. 1.20(d): a focused ion beam (FIB) is used to polish a cross section.

Fig. 1.20(e): the layer structure with the polished cross section can be characterized by the scanning electron microscope (SEM).

1.4.2 Characterization
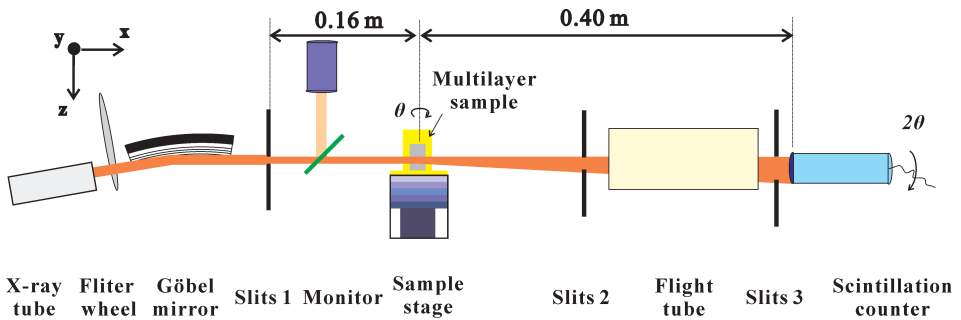
Figure 1.21: *The laboratory diffractometer Wendi. The schematic of the laboratory diffractometer 'Wendi', operated at $Cu\ K_\alpha$ photon energy (8.048 keV) as selected by the bent multilayer mirror (Göbel mirror).*

Fig. 1.21 shows the schematic of the in-house setup *Wendi* at the Institute for X-ray Physics, University of Göttingen. The X-ray tube (Dx-Cu 12×0.4-S GE-Seifert), generates a characterisitic line of Cu Kα (λ= 0.154 nm, E = 8.048 keV) radiation, which is collimated (to a parallel beam) by a parabolic Göbel mirror, made from a W/C multilayer on a bent substrate. The mirror also suppresses the bremsstrahlung background. The output x-ray beam can be attenuated by six Al filters with different thicknesses from 0 to 750 μm. A monitor detector (GE-Seifert) is mounted behind the entrance slit (slit 1), recording the intensity from a thin Kapton foil, scattered at 90°. This allows for the inspection of the primary intensity, after calibration. By control of the fully motorized slit 1 system, the incoming beam size is controlled. A typical slit setting (slit 1) for reflectivity was 0.1 mm× 6 mm in $y \times z$ plane. The sample was mounted on a z-axis goniometer tower (Huber Diffraktionstechnik) with Eulerian cradles and yz trans-

lation on the θ rotation axis. Setting the slits on the detector arm (2θ-arm), slits 2 and 3 (detector slit) were adjusted to minimize the contribution from scattering in non-specular directions. The multilayer sample was mounted upright in xz plane by fixing it by double-sided tape on a home-built Aluminum holder. More details on the instrument can be found in [73]. After careful alignment, an incoming beam with incident angle α_i and beam size 0.1 mm in y direction hits on the sample surface. The scintillation counter can collect the diffracted beam signal. Many different measurements can be accomplished in the *Wendi* setup, as discussed in detail in the App. C.1. In general, the reflectivity curves are measured in the range of incident angle θ from 0° to 10° with 0.005° step size and 30 s exposure time per step, e.g. the initial x-ray reflectivity curve is shown in blue line of Fig. C11 in App. C.1, and after subtracting background and performing an illumination correction, the curves can be fitted as shown in Fig. 4.8 in App. 4.4 in Chapter 4.
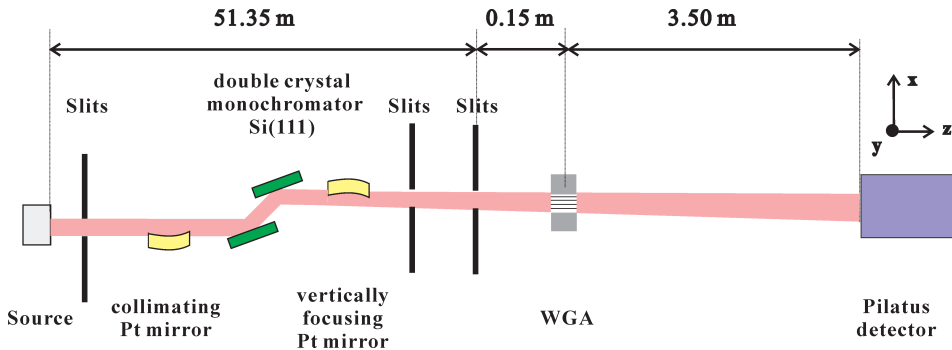
Figure 1.22: *The path of the x-rays is traced from the storage ring to the waveguide chip. Radiation 19.9 keV photon energy was selected by a double crystal monochomator.*

Fig. 1.22 presents the schematic of experimental setup at the ROBL beamline at the ESRF in Grenoble, France [29]. The beam exiting from the source is filtered by a $Si(111)$ double crystal monochromator (E = 19.9 keV), which is placed in between two conjugate Pt mirrors. The WGA is positioned at the focal plane of the conjugate Pt mirrors. After alignment, the incoming beam with beam size 160 μm × 60 μm in $x \times y$ plane is coupled into the front side of WGA and guided within length L, before it couples out in the exit plane. By multi-channel interference, the 2D far-field pattern of WGA is measured by a single photon counting pixel detector (Pilatus; Dectris Inc., Switzerland) with a square pixel size of 172 μm at 3.5 m. The 1D far-field intensity distribution is recorded at a
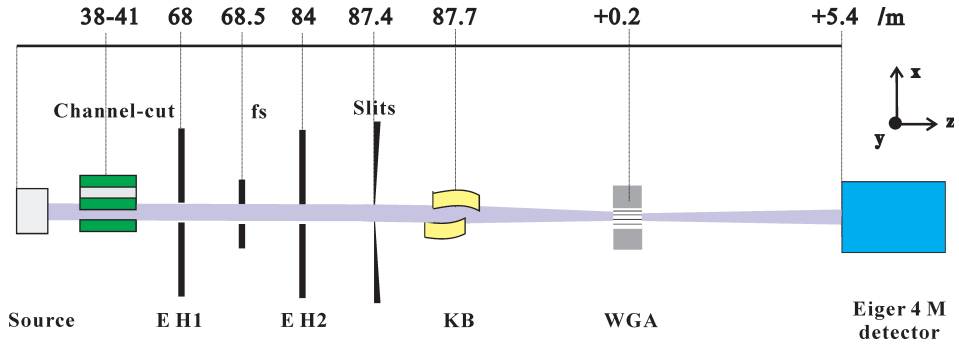
Figure 1.23: *Schematic of the GINIX nano-focus instrument at the P10 undulator beamline of the PETRA III storage ring at DESY. For this work, the radiation of 13.8 keV photon energy was used.*

distance of 0.97 m behind the WGA exit by a one-dimensional pixel detector (Mythen, Dectris) with a pixel size of 50 μm. The corresponding far-field patterns are shown in Chapter 2.

Fig. 1.23 shows the schematic of the GINIX (Göttingen Instrument for Nano-Imaging with X-rays) experiment setup, installed in the second experimental hutch (EH2) at the P10 beamline at the PETRA III synchrotron facility in Hamburg (DESY) [12, 74]. The beam exiting from the source can be selected by a channel-cut device (E = 13.8 keV). The KB focusing system of GINIX provides an x-ray nano-focus for the photon energy range between 6 and 14 keV [75–78], which consists of a vertically focusing mirror and a horizontally focusing mirror with Rh (Rhodium) coating (a few tens of nm) on the surface. Depending on the slits in front of the KB, the beam size in the focal plane (focal length f = 200 mm for the second mirror) can be adjusted. In particular, smaller slits result in full coherence and a broadening of a focal spot by diffraction. For alignment of the KB, the reference 2DWG [12, 27] was placed on a custom-designed hexapod system (Smaract) in the focal plane of the KB mirrors. By translating the aligned 2DWG, the beamsize of the KB was measured. After alignment, Fig. 1.24(c) shows the measured far-field pattern of the 2DWG as a function of the coordinates θ_x and θ_y (exposure time 1 s of a frame), recorded by the Pilatus detector with a square pixel size of 172 μm at 5.4 m. The alignment followed the references [12, 27]. Fig. 1.24(a, b) presents the beamsizes in (a) the horizontal (y, $FWHM$ = 302 nm) and (b) the vertical (x, $FWHM$ = 632 nm) directions, respectively, with the slits sizes in front of the KB (horizontal slits hg 0.4 mm and vertical slits vg 0.4 mm in x and y direction, respectively). Note that the diffraction plane for the WGA samples was the vertical direction, and the beam
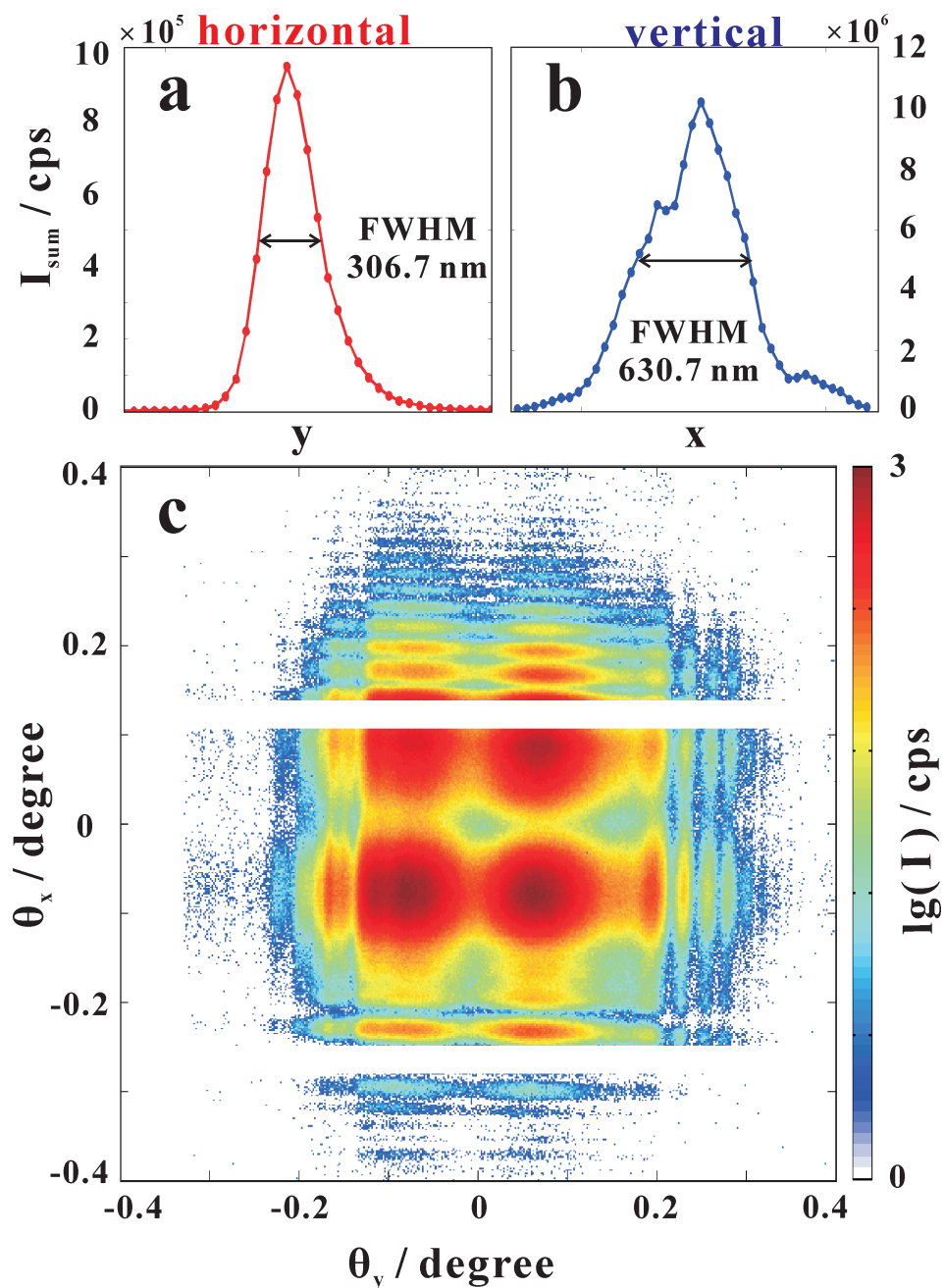
Figure 1.24: *(a) Horizontal beam profile and (b) vertical beam profile measured by scanning a waveguide through the focal plane of the KB mirrors. (c) Far field patterns of the reference 2DWG [27] by using Pilatus detector at the distance 5.4 m.*

needed to be sufficiently large to couple into all planar layers. At the same time, reducing the slits in front of the KB, the coherence was increased, along with the focal spot size. Therefore, experiments as shown in Chapter 2 and 4 were carried out with small slit setting yielding full coherence and a spot size broadened by diffraction. For alignment a Pilatus 300 k was used, while the actual far-field pattern of the samples were recorded by a Eiger 4 M pixel detector (Dectris) with a square pixel size of 75 μm at 5.4 m.

2 X-ray waveguide arrays: tailored near-fields by multi-beam interference

Qi Zhong, Markus Osterhoff, Mingwu Wen, Zhanshan Wang and Tim Salditt

A novel 1D X-ray waveguide, the *Mo/C* waveguide array (WGA), is introduced to tailor the optical near-field distribution by precisely designed and controlled multi-beam interference at 19.9 keV hard x-ray energy. Seven precisely controlled guiding layers with optimized layer thickness variation were fabricated by high precision direct-current magnetron sputtering of amorphous carbon (*C*) and molybdenum (*Mo*). The thickness variations are designed in such a way to introduce the desired phase shifts between the guided output beams, to act as a quasi-focusing device. The WGA and the layer thicknesses are characterized by x-ray reflectivity (XR), Transmission Electron Microscopy (TEM), and measurement of the synchrotron radiation far-field intensity pattern. Based on the measurements and simulations, a reliable *Mo/C* multilayer layers combination can be verified. With the layer thicknesses, simulations inside the WGA and in the optical near-field behind it show that multi-beam interference with the designed phase shifts lead to a relative beam intensity of 0.59 in a quasi-focal plane 0.08 mm behind the exit, with a spot size of 23.8 nm.

2.1 Introduction

X-ray waveguides (WGs) serve a variety of x-ray optical purposes like beam collimation in the nanometer range, coherence filtering [79] for high resolution holographic X-ray imaging [11], beam splitting for interferometry [22], beam tapering [23] or angular redirections [24] to "bend" x-rays. Typical diameters d of the guiding core are in the range of a few tens of nanometers, while the length of the waveguide L is in the range between 0.1 to 10 mm depending on the photon energy. Note that in imaging experiments, L is dictated by the requirement to absorb the radiative modes, and to single out only the guided modes.

The theoretical limits for beam collimation was shown to be in the range of 10 nm depending on the material [26], and experimental values in the predicted range have been demonstrated, notably 8 nm [27, 28] in a planar thin film waveguide with an optimized cladding material ($Mo/C/Mo$ structure embedded in Ge [29]). Several different ways have been used to generate x-ray modes, or more precisely to couple x-ray beams into WGs. Resonant beam coupling into planar waveguided with thinned cladding was used in early work [13–17]. Front coupling into planar waveguides with tunable air gaps was then demonstrated in [18], and later extended to two-dimensional waveguide channels [20, 56, 57]. Tapered waveguide with a broader entrance size that geometrically collects more of the incoming light and can funnel the beam to a smaller exit size. Tapered waveguides channels with an exit size down to 16.5 nm × 14.6 nm have been reported recently [23]. In [30, 31], the single guiding film was generalized to an array of planar wavguides, and in [32, 33], the cladding was generalized to a multilayer structure.

 In this work, we present a new approach combining the multilayer concept
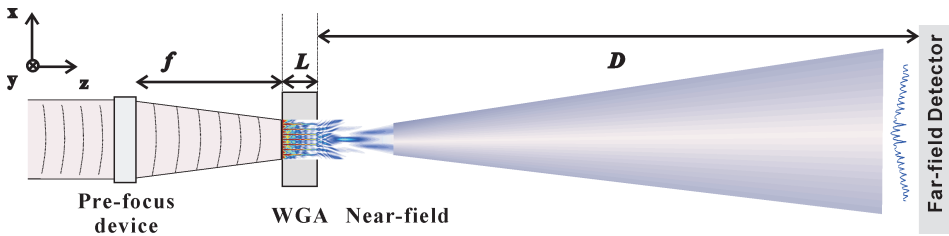
Figure 2.1: *Schematic experimental setup at the undulator endstation. The waveguide array (WGA) is positioned at f in the focal plane of an elliptic mirror system, which could also be replaced by alternative (pre-focusing) devices such as compound refractive lenses (CRL) or Fresnel zone plates (FZP). The incoming beam, with primary intensity I_0 and photon energy E, is coupled into the front side of the X-ray waveguide array, guided within the WGA of length L, before it couples out in the exit plane. By multi-channel interference the near-field can be tailored in the desired way. The far-field detector (a photon counting pixel detector) is located at the distance D behind the WGA exit. From its far-field intensity pattern, the near-field can be reconstructed by iterative phase retrieval.*

with a novel geometry, aimed at creating particular interference pattern and designed near-field distributions behind the waveguide exit. In particular, we design, fabricate, and test a specific x-ray waveguide array (WGA) made from a Mo/C layer sequence, with controlled exit phases by variation of d. The WGA can serve several purposes: First, it enables similar optical functions and applications as conventional x-ray waveguides used at synchrotron sources, in particular coherence and spatial filtering if the incoming beam, as illustrated in

Fig. 2.1. To this end, the WGA is aligned in the pre-focused synchrotron beam of photon energy E. The beam is then guided (and filtered by selective absorption of radiation modes) over a working length L, before it is coupled out in the exit plane. The desired exit near-field distribution is governed by free-space propagation and finally diverges to the far-field pattern, which can be recorded at the distance D by the far-field detector. Compared to the conventional waveguides with a single guiding layer, the WGA has a larger effective entrance cross section, it can thereby help to increase the coupling efficiency. Second, with an optimized material combination, the WGA can reduce the absorption inside the cladding. Third and most importantly, the phase relations between the different guided beams can be tailored to produce special near-fields behind the WGA's exit by multi-waveguide interference. This differs from multilayer Fresnel zone plates (FZP), which is based on diffraction in a more or less thin structure. In FZPs, diffraction within the zones compromise the interference pattern and focusing, while the WGA is based on eigenmodes corresponding to the full 3D structure. In other words volume diffraction effects are undesired in FZP optics, but are the intrinsically built into the concept of WGA. Near-field interference behind the exit plane are then achieved by carefully designing the multilayer geometry, in particular by choosing different cross sections d_i for each channel i. This allows to tailor intensity distributions with special properties, e.g. creating a secondary quasi-focal spot in free-space. We demonstrate this concept by a specific x-ray WGA consisting of seven planar waveguides with precisely designed layer thickness variations, fabricated by high precision direct-current magnetron sputtering of amorphous carbon and molybdenum. To control the relative phases between the seven guided beams, thickness variations on the order of 0.2 nm are required.

The paper is organized as follows. In Sec. 2 we describe the analytical and numerical design; the fabrication of our WGA is explained in Sec. 3. The WGA is first characterized by x-ray reflectivity (XR) and Transmission Electron Microscopy (TEM) in Sec. 4.1; in Sec. 4.2 we report synchrotron radiation measurements carried out at the European Synchrotron Radiation Facility (ESRF); near-field simulations based on all these measurements are presented in Sec. 4.3. We conclude with a summary and comments in Sec. 5.

2.2 Theoretical calculation and design

To tailor the optical near-field behind the WGA, the relative phases of the guided beams have to be controlled via the layer thickness. Note that in con-

trast to single x-ray waveguides, the WGA generates x-ray guided modes in each of the waveguide layers. The exiting field consists of a multiple of beamlets with different phases, as controlled by the individual guiding layer thickness. In this way we can achieve special near-field interference patterns. To design this multilayer structure, we first derive analytical expressions for the phase shift, and then verify the performance of a WGA by numerical simulations.
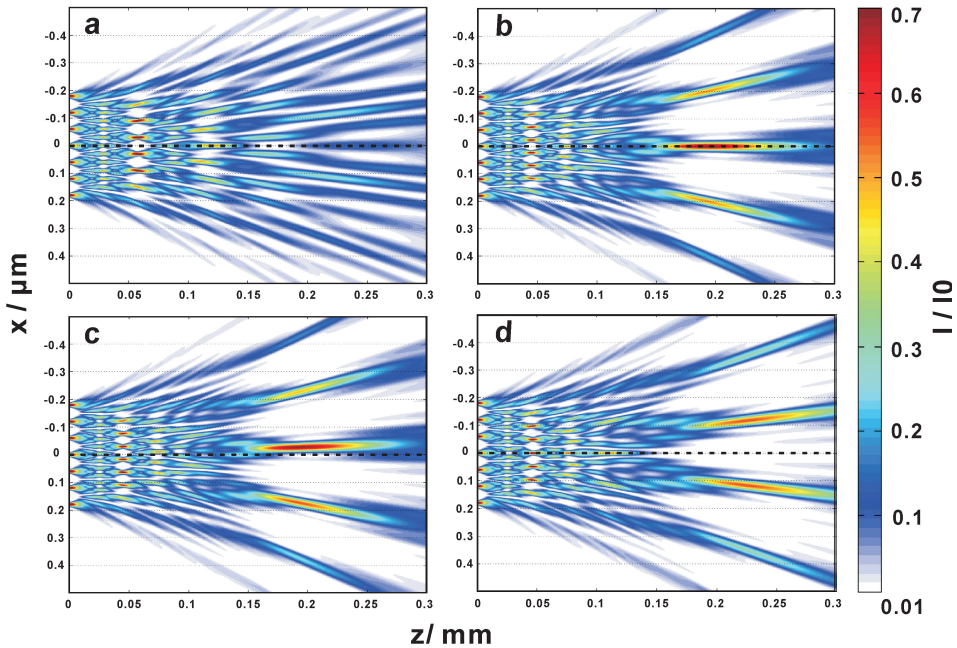
Figure 2.2: *The multi-beam interference in free space is controlled by using different phase φ_i for a 7 channel structure: (a) constant phase profile, (b) a "focus phase" profile, (c) an off-axis "focus phase", and (d) a "double focus phase".*

Considering a multi-channel simulation as shown in Fig. 2.2 with seven channels ($i = 1, \ldots, 7$), each emitting a Gaussian beam of unit intensity, and with constant width ($FWHM$) of 8 nm (channel widths). The distance between channels is 60 nm, which is close to the fabricated parameters for an x-ray energy of 19.9 keV. The phases of the guided beams are denoted φ_i. Clearly, if all φ_i have the same value, this multi-channel structure is equivalent to a simple grating. Fig. 2.2(a) shows the corresponding near-field simulation, based on free space propagation using the parabolic wave equation [20].
To tailor a near-field with e.g. a quasi-focal spot, we keep the central channel's

phase unchanged, but decrease the phases φ_i symmetrically towards the outside, thus creating a convex lens for the x-ray beam; see Fig. 2.2(b). Alternatively, with asymmetrical phases, an off-axis quasi-focal spot as in Fig. 2.2(c) can be formed. Even a double quasi-focus as shown in Fig. 2.2(d) is possible: starting from the parameters of Fig. 2.2(d), a double quasi-focus is obtained by an additional decrease of the central channel's phase.

In the following, we will put the WGA design on a more rigorous theoretical footing. We consider a planar thin film with index of refraction n_1 with thickness d, sandwiched between two cladding layers of index n_2. In general, there is also a substrate material with n_{sub}; but for thick cladding layers, the substrate influence can be neglected. This planar WG is sketched in Fig. 2.3(a) and (b). Now, the index of refraction profile $n(x)$ is independent from y and z and reads

$$n(x) = \begin{cases} n_1, & |x| \leq d/2, \\ n_2, & |x| > d/2, \end{cases} \tag{2.1}$$

The electric field $E_y(x)$ inside this 1DWG is determined by the reduced Helmhotz equation [34–36]

$$d^2 E_y/dx^2 + [k_0^2 n^2(x) - \beta^2] E_y = 0, \tag{2.2}$$

where β is the propagation constant, and the wave vector k in z-direction is given as $k = n \cdot k_0$ in the corresponding medium. Since the guided mode is confined inside the guiding layer of thickness d, the propagation constant β is restricted to $k_0^2 n_2^2 \leq \beta^2 \leq k_0^2 n_1^2$. The solutions of Eq.(2.2) can be written as symmetrical and asymmetrical modes:

$$E_y^{sym}(x) = \begin{cases} A\cos(\kappa x), & |x| \leq d/2, \\ Ce^{-\gamma|x|}, & |x| > d/2, \end{cases} ; \tag{2.3}$$

$$E_y^{asym}(x) = \begin{cases} B\sin(\kappa x), & |x| \leq d/2, \\ De^{-\gamma|x|}, & |x| > d/2, \end{cases} , \tag{2.4}$$

with $\gamma^2 = \beta^2 - k_0^2 n_2^2$ and $\kappa^2 = k_0^2 n_1^2 - \beta^2$. Requiring continuity of the electric field and its derivative, the guided modes have to fulfill these transcendental equations:

$$\xi \tan \xi = \left[\left(\frac{V}{2} \right)^2 - \xi^2 \right]^{1/2} \tag{2.5}$$

for symmetrical modes;

$$-\xi \cot \xi = \left[\left(\frac{V}{2} \right)^2 - \xi^2 \right]^{1/2} \tag{2.6}$$

for asymmetrical modes. Here, the waveguide parameter is $V = k_0 d \left(n_1^2 - n_2^2 \right)^{1/2}$, and the propagation constant is $\beta = (k_0^2 n_1^2 - 4\xi^2/d^2)^{1/2}$. From Eq.(2.2) we see that the guided beam's phase $\varphi = \beta \cdot L$, where L is the working length of the waveguide. We assume L and the indices of refraction $n_{1,2}$ fixed. Hence, the phase relations φ can be tailored by designing the propagation constants β; rewriting the equation of β we have e.g.

$$\xi = \frac{d}{2} \sqrt{k_0^2 n_1^2 - \beta^2} \qquad (2.7)$$

for symmetrical modes.

How does the phase φ depend on d ? A series expansion for small changes $d \to d + \Delta d$ (and similar expressions for the other quantities) yields the transcendental equation (symmetrical modes)

$$(\xi_0 + \Delta\xi) \tan(\xi_0 + \Delta\xi) = \sqrt{\left(\frac{V_0 + \Delta V}{2} \right)^2 - (\xi_0 + \Delta\xi)^2}; \qquad (2.8)$$

Inserting the waveguide parameter $V_0 = k_0 d_0 \sqrt{\left(n_1^2 - n_2^2 \right)}$ yields

$$\Delta\xi = \frac{1}{4} \frac{V_0^2 \Delta d}{\xi_0 d_0 \left(1 + \dfrac{\xi_0 \sin\xi_0}{\cos^3 \xi_0} + \tan^2 \xi_0 \right)}, \qquad (2.9)$$

which can be solved to

$$\Delta\beta = \frac{\Delta d}{d_0 + \Delta d} \left[\frac{k_0^2 n_1^2}{\beta_0} - \frac{V_0^2}{d_0^2 \beta_0 \left(1 + \dfrac{\xi_0 \sin\xi_0}{\cos^3 \xi_0} + \tan^2 \xi_0 \right)} - \beta_0 \right]. \qquad (2.10)$$

For Δd close to zero, $\partial\xi/\partial d \approx \Delta\xi/\Delta d$ and $\partial\beta/\partial d \approx \Delta\beta/\Delta d$. This determines a first-order relationship between propagation constant β and guiding layer thickness d for symmetrical modes:

$$\frac{\partial\beta}{\partial d} \approx \frac{\Delta\beta}{\Delta d} = \frac{k_0^2 n_1^2}{d_0 \beta_0} - \frac{V_0^2}{d_0^3 \beta_0 \left(1 + \dfrac{\xi_0 \sin\xi_0}{\cos^3 \xi_0} + \tan^2 \xi_0 \right)} - \frac{\beta_0}{d_0}; \qquad (2.11)$$

The analogous calculation for asymmetrical modes gives

$$\frac{\partial\beta}{\partial d} \approx \frac{\Delta\beta}{\Delta d} = \frac{k_0^2 n_1^2}{d_0 \beta_0} - \frac{V_0^2}{d_0^3 \beta_0 \left(1 - \dfrac{\xi_0 \cos\xi_0}{\sin^3 \xi_0} + \cot^2 \xi_0 \right)} - \frac{\beta_0}{d_0}. \qquad (2.12)$$

To validate this analytical description for the dependence of $\varphi(d)$, we have simulated the electromagnetic field inside the planar waveguides using a finite difference algorithm [20] for the intended x-ray energy of 19.9 keV. The WG consists of a planar C layer sandwiched between to Mo layers on the top of a Ge wafer, see Fig. 2.3(a, b), with a propagation length (channel length) of $L = 0.28$ mm in z direction. We have simulated C layers with $d_1 = 8$ nm (WG1) and $d_2 = d_1 - \Delta d = 7.6$ nm (WG2). The Mo layer thickness is 52 nm for both structures. The electromagnetic field (intensity) inside these structures is shown in Fig. 2.3(c) and (d), respectively. We assume that the same intensity I_0 impinges on both WGs.

The exiting field of the two WGs is compared in Fig. 2.3(e) (intensity) and (f) (phase). The (normalised) intensity of WG2 is slightly smaller than WG1. The phase shift in the exit plane of two WGs (WG1 and WG2) is $\Delta \varphi = 0.486\pi$, which is in good agreement with the prediction of $\partial \beta / \partial d \approx 1.36194 \times 10^{-5}$ based on Eq.(2.11) (symmetrical modes).

To sum up, analytical and numerical calculations, show that a WGA with desired properties can be designed. The parameters are given in Table 2.1. The bi-layer period (Mo/C layers) is 60 nm, and the C layers vary symmetrically from 8 nm (center) down to 4 nm (outmost layers).

The advantages of the designed structure over conventional x-ray waveguides are the following:

1. *Increased aperture:* Compared to 1D straight channel WGs, the aperture collecting the incoming light is larger by the number of channels. If the thickness of a single WG channel would be increased, the number of excited modes also increases [20], which impacts the overall coherence [79]. In the case of WGA, on the other hand, we can achieve a large aperture, although the individual channels are still mono-modal.

2. *Reduced absorption:* It is well known that a multilayer structure based on Bragg theory can increase the guided intensity [32, 33]; also the choice of materials plays an important role: Introducing two Mo layers into a $Ge/C/Ge$ structure can increase the transmission significantly [29] by reducing absorption of the evanescent wave in the cladding.

3. *Control of the exit phase for quasi-focusing*: At first sight, the presented WGA seems similar to (multilayer) Fresnel Zone Plates (FZPs). But the focusing effect is achieved in a different way: In the case of FZPs, the zone positions are based on geometrical optics; for multilayer FZPs, x-ray diffraction theory is applied. Here, it is only the layer thickness that is changed, and in such a way to produce the phase relations required for a
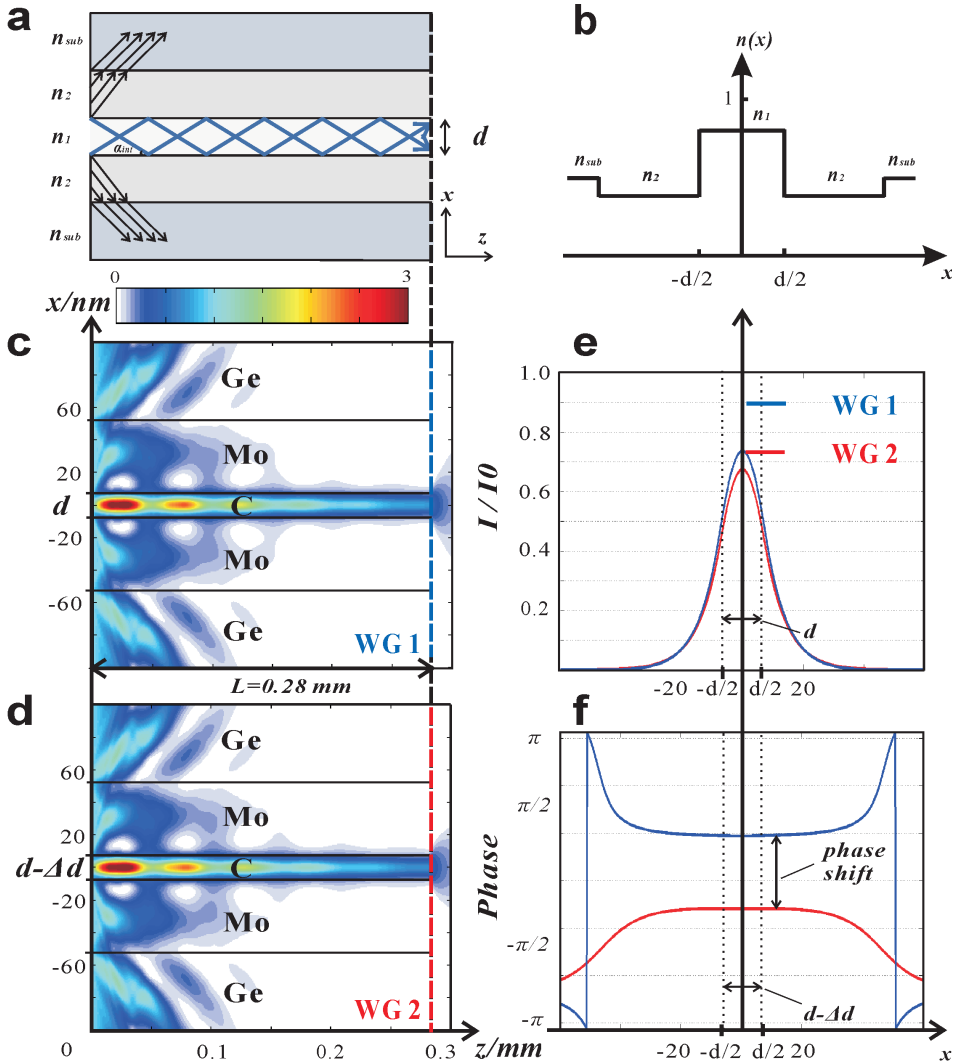
Figure 2.3: *(a) Sketch of slab waveguide, one guided mode is propagating inside the guiding layer. (b) The refraction index profile $n(x)$ with $n_2 < n_1 < 1$. The electromagnetic field inside the planer waveguide is simulated for a C layer sandwiched between two Mo cladding layers on Ge wafers. The photon energy is 19.9 keV, and the propagation length along the optical axis z is $L = 0.28$ mm. The Mo/C/Mo layers for each kind of structures (WG1 and WG2) are sandwiched between Ge wafers. The layer thicknesses of the guiding layers are (c, e) $d_0 = 8$ nm in WG1 and (d, f) $d_0 - \Delta d = 7.6$ nm in WG2. The corresponding results for the exit field (e) intensities and (f) phases are shown in blue ($d_0 = 8$ nm) and red ($d_0 - \Delta d = 7.6$ nm), respectively. The intended phase shift is clearly demonstrated.*

specific purpose such as forming a quasi-focal spot. Note that more chan-
nels are needed to obtain a more pronounced quasi-focus. In contrast to
multilayer FZP, the WGA does not suffer from volume diffraction, owing
to the nature of the guided modes, which are eigenmodes of the full 3D
structure. Hence, in contrast to multilayer FZP, the optical structure does
not have to be 'thin'. This is achieved, since the near field distribution be-
hind the WGA is not tailored by phases shifts calculated by a projection
approximation, but by phase shifts arising from propagation of guided
modes.

Generally speaking, these advantages of the novel WGA result in enhancement
of the waveguide performance [26, 29, 32, 33], being at the same time a coher-
ence filter and a secondary quasi-focusing device.

2.3 Experiment

The fabricated Mo/C waveguide array consists of seven C and eight Mo lay-
ers. The in total 15 layers according to the designed thicknesses shown in Table
2.1 had been deposited on a Ge wafer using direct-current magnetron sputter-
ing [66, 71], at the Institute of Precision Optical Engineering at Tongji University.
The base pressure was set to 1.8×10^{-4} Pa; the sputtering gas was Ar with a pu-
rity of 99.9999%, with a gas pressure of $2.00 \pm .02$ mTorr (0.266 Pa). The solid Mo
and C targets had a diameter of 100 mm. After deposition, a Ge capping wafer
had been bonded in a vacuum oven at 250° for one hour. After annealing, the
WGA was cooled down to room temperature at a base pressure of 1×10^{-1} Pa.
Afterwards, the WGA was sliced into a 280 μm thick sample.

The fabricated structure had been characterised by x-ray reflectivity (XR) using
a $Cu\ K_\alpha$ source with $\lambda = 0.154$ nm. The reflectivity curve was then fitted to the
multilayer model, using the Genetic Binda algorithm of IMD [45]. As additional
verification, a specimen for transmission electron microscopy (TEM, Philips
CM 200 FEG-UT) had been prepared by a Focused Ion Beam (FIB, FEI Nova
Nanolab 600) at the IV. Physical Institute of Gttingen University.

The far-field diffraction pattern of the WGA was measured at the Rossendorf
Beamline (ROBL) of the European Synchrotron Radiation Facility (ESRF) in
Grenoble, France, at an x-ray energy of 19.9 keV. Simulations had been per-
formed using a finite-difference algorithm based on the parabolic wave equa-
tion [20]. See the next section for more details.

2.4 Results

X-ray reflectivity and Transmission electron microscope
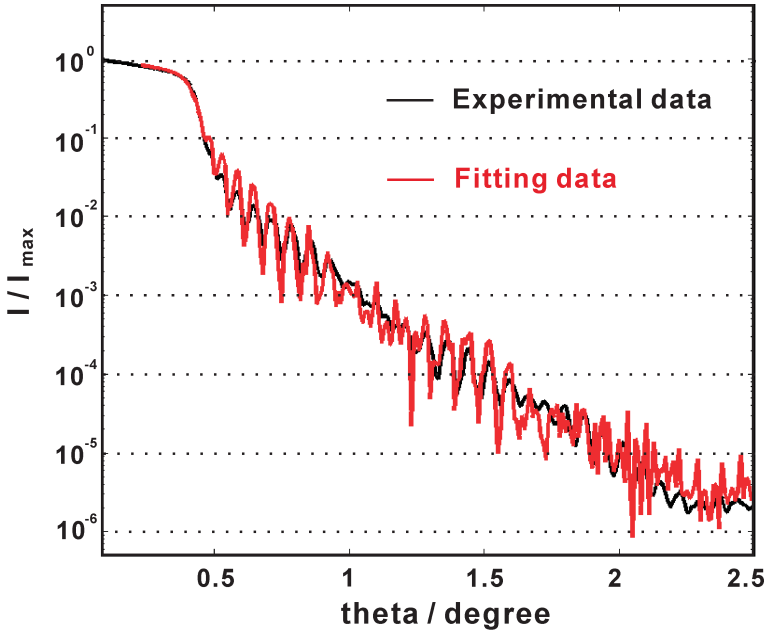
Figure 2.4: *Measured reflectivity (black line) and fitting curve (red line) as a function of incident angle θ for the multilayer sample, as measured before the bonding process.*

The layer structure of the Mo/C multilayer WGA was first characterised by XR over an angular range of 0 to 10 degrees with a Cu K_{α} source. In addition, an off-set scan (off-set angle of 0.1°) was measured to determine the background. The measured data after correcting for illumination and background is shown as the black line in Fig. 2.4. The best fitting model curve with layer thickness and roughness as tabulated in Table 2.1 is shown in red curve. Accordingly, the deposited structure is slightly asymmetric but close to the design values, and the interface roughness in the order of 0.7 nm. Because the Mo layers are fully crystallised, the roughness of the C-on-Mo interfaces is larger than that of the Mo-on-C interfaces.

The Mo/C layer structures characterized by XR had also been inspected by TEM. Fig. 2.5(a) shows three transmission electron micrographs, with superimposed design layer scheme. The pixel size is 0.32 nm, and the scale bar denotes

as 50 nm. From six different images and 50 line cuts, the layer thicknesses had been measured and were summarised in Table 2.1 (TEM results). The average layer thickness is determined from the line cut results.

Table 2.1: *Design parameters, XR fitting results and average layer thickness as determined by TEM.*

Layer Nr.	15	14	13	12	11	10	9	8	7	6	5	4	3	2	1	Sub
Layer name	Mo top	C	Mo	C	Mo	C	Mo	C	Mo	C	Mo	C	Mo	C	Mo	Ge Sub
Theoretical design results																
Layer thickness /nm	50.00	4.00	56.00	6.20	53.80	7.60	52.40	8.00	52.40	7.60	53.80	6.20	56.00	4.00	50.00	
XR fitting results																
Layer thickness /nm	49.81	4.25	53.15	5.92	51.30	7.27	49.90	8.33	49.72	6.80	52.40	5.34	55.40	3.41	50.00	
Roughness /nm	0.69	0.87	0.84	0.82	0.79	0.80	0.77	0.90	0.81	0.69	0.60	0.74	0.63	0.59	0.50	0.62
TEM reading results error bar ± 0.32 nm																
Layer thickness /nm	49.67	4.07	53.00	5.85	51.25	7.33	49.97	8.32	49.93	7.07	52.48	5.46	55.70	3.70	50.08	
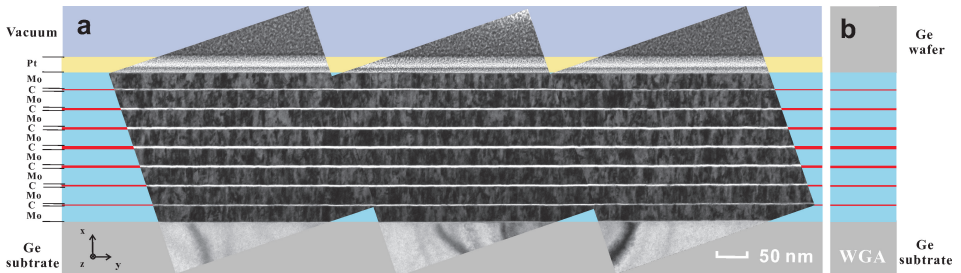
Figure 2.5: *(a) TEM image of the cross section of the multilayer with seven C guiding layers and eight Mo cladding layers, deposited on the Ge wafers. Scale bar 50 nm. (b) After bonding, the Ge capping wafer on the multilayer sample is sliced into the length $L = 0.28$ mm, ready for experiments.*

Far-field pattern measurements

To further estimate the layer thickness and x-ray optical performance of the WGA, far-field intensity patterns had been measured at the ROBL beamline,
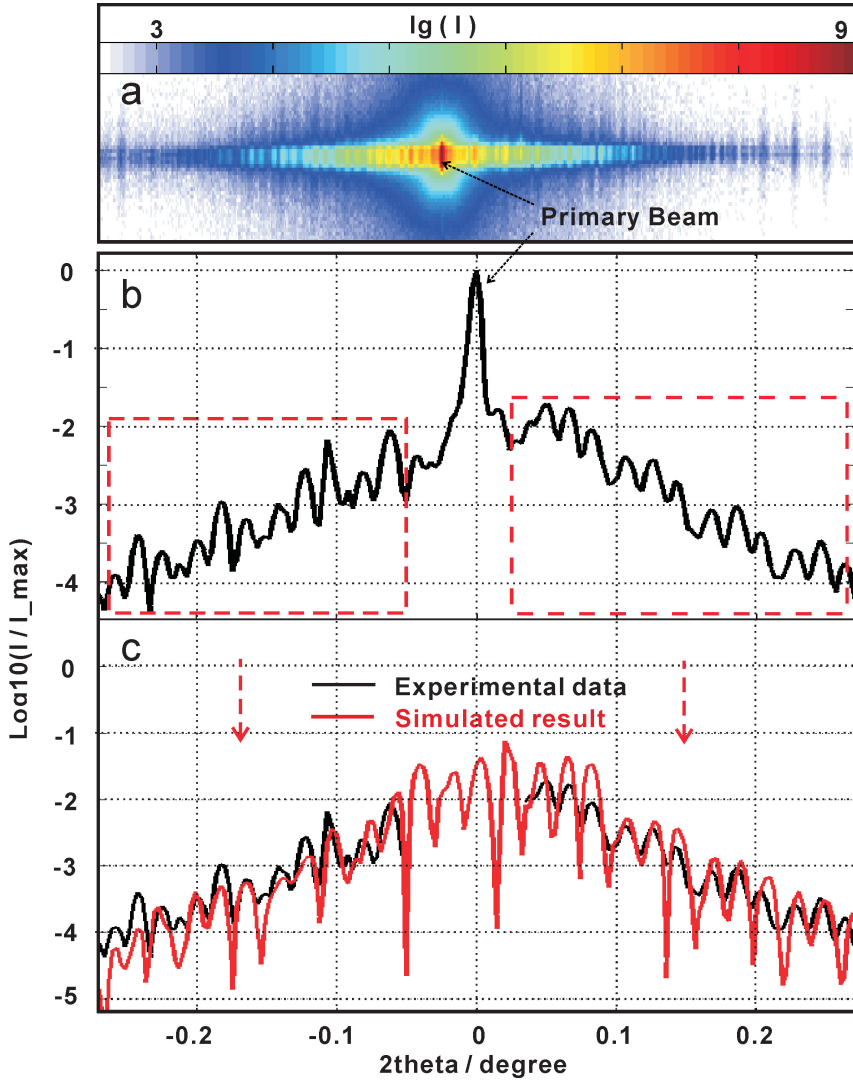
Figure 2.6: *(a) The two-dimensional far-field pattern of the WGA at 19.9 keV was measured by the Pilatus detector at 3.5 m in ROBL beamline, ESRF. (b) The 1D far-field intensity distribution was recorded at a distance of 0.97 m behind the WGA exit by a one-dimensional pixel detector (Mythen, Dectris). The regions indicated by the red dash rectangles had primarily been used for finding the best parameters in the simulation, since the central values were too much affected by the primary beam. (c) Simulation curve for the parameters shown in Table 2.2.*

ESRF, France. The X-ray energy was 19.9 keV. After alignment, two-dimensional far-field images had been recorded with a single photon counting pixel detec-

tor (Pilatus; Dectris Inc., Switzerland) with a square pixel size of 172 μm; the detector was placed 3.5 m behind the WGA.

With the working length (L) of 280 μm, the primary beam penetrated trough the WGA and covers part of the multilayer signal (vertical stripes), as shown in Fig. 2.6(a). However, the largest part of the strip pattern was not affected by the primary beam. In addition, a 1D Mythen detector (Dectris Inc) with a pixel size of 50 μm was placed 0.97 m behind the WGA; the data is shown in Fig. 2.6(b) on a logarithmic scale. Apart from the primary beam in the center, a regular diffraction pattern from the WGA is visible. By varying the *Mo* and *C* layers thickness, a simulated far-field with reasonable agreement has been found, see the red curve in Fig. 2.6(c). A comparison of simulation and experiment shows that the peak positions are in very good agreement, while the intensities vary more strongly. We attribute this difference to influences by the background intensity in the near-field. Experimentally, this background cannot be fully measured by the detectors due to limited pixel size (limited sampling).

The simulated data has been obtained first by numerical propagation inside the WGA with adjusted layer structures, and second by a Fourier transform into the far-field detector plane. The used layer parameters are summarized in Table 2.2.

Table 2.2: *Comparison of layer thickness: design values and simulation results (from far-field pattern).*

Layer Nr.	15	14	13	12	11	10	9	8	7	6	5	4	3	2	1
Layer name	Mo top	C	Mo	C	Mo	C	Mo	C	Mo	C	Mo	C	Mo	C	Mo
Theoretical design /nm	50.00	4.00	56.00	6.20	53.80	7.60	52.40	8.00	52.40	7.60	53.80	6.20	56.00	4.00	50.00
Far-field simulated results /nm	49.97	4.35	53.00	5.96	51.36	7.25	49.84	8.40	49.74	6.75	52.40	5.32	55.40	3.40	50.00

Propagation in the near-field

The layer thickness results obtained using XR fitting and TEM measurements from Table 2.1 and far-field experiments from Table 2.2 are compared against the design values (light blue circles) in Fig. 2.7. Interlayer roughness has been estimated to be larger than 0.5 nm by XR, which might influence the propagation inside the WG channels [36]. However, roughness has not yet been incorporated into the simulations. This could be a further reason why the simulated far-field data (red triangles) differs from the XR values (dark blue stars), even
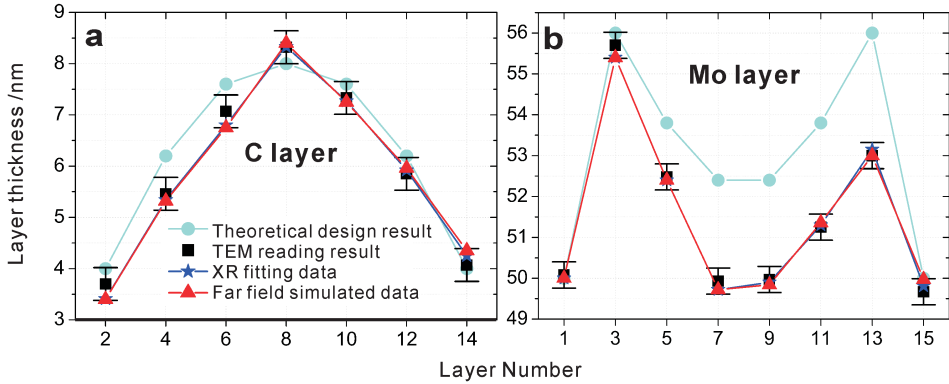
Figure 2.7: *Layer thickness of (a)* C *and (b)* Mo *layers for the measured WGA, compared to the design profiles (light blue). Experimental results correspond to the parameters from Table 2.1 and 2.2. TEM values are shown as black points, XR fitting results in dark blue stars, and far-field simulated data points in red.*

though the overall agreement is quite satisfactory. The TEM measurements (black squares) are averaged over 50 line cuts from six different images of different parts of the TEM specimen. The error bars of ±0.32 nm reflect the TEM resolution (limited mainly by the image pixel size). The three experimental results, i.e. the XR, TEM and the far-field simulation results, respectively, agree within the respective error bars (see also Table 2.1 and 2.2).

From these different measurements, we have selected the far-field values (red triangles) for further discussion. Based on these layer thicknesses, the optical performance of the WGA can be visualised by optical near-field simulations inside and directly behind the device. The X-ray intensity calculated by a finite difference algorithm is shown in Fig. 2.8 for the design values (a) and the measured values (b). In case of the design WGA, the quasi-focal spot is located 0.18 mm behind the device, with a relative intensity of $I/I_0 = 0.30$ compared to the illumination, and a full width at half maximum ($FWHM$) of 37.2 nm. The actual layers possess a higher numerical aperture, yielding a quasi-focal spot at only 0.08 mm behind the device, with $I/I_0 = 0.59$ and a $FWHM$ of 23.8 nm. We conclude that the fabricated structure does indeed show the tailored near-field beams as designed, although in the present case the design values have not been reached with good accuracy. The general idea of a WGA, on the other hand, has shown its potential as a combined filtering and forming a quasi-focal spot device for imaging, diffraction, and spectroscopy with nanometer sized X-ray beams.

F₁: *I_max/I0=0.30 , FWHM=37.2 nm*   F₂: *I_max/I0=0.59 , FWHM=23.8 nm*
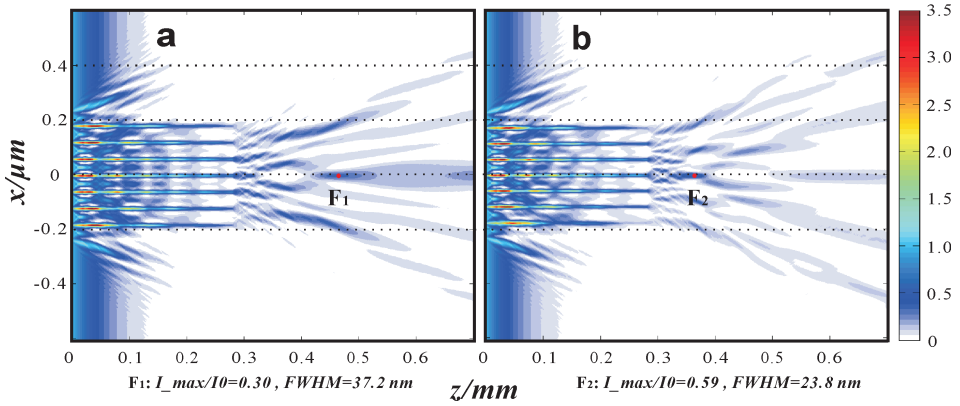
Figure 2.8: *Propagation in the WGA and free space is shown by using the theoretical design layer thickness (a) and far-field simulated data (b). The information of the quasi-focal spot (*F1 *and* F2*) are presented in both figures.*

2.5 Conclusion

In conclusion, based on an analytical and numerical design, an x-ray waveguide array has been fabricated; with the tailored optical near-field, the WGA acts both as a filtering and focusing device for hard x-rays. The layer thicknesses of the WGA have been measured using x-ray reflectivity, transmission electron microscopy, and x-ray diffraction. From the measured multilayer structure, the optical near-field, which is not directly accessibly to experimental methods, has been investigated by numerical simulations.

The multi-beam interference of seven guiding layers with phase shifts controlled by varying layer thickness lead to a free-standing quasi-focal spot behind the WGA with a spot size of 23.8 nm ($FWHM$). Further generalizations of such a scheme involving a significantly higher number of waveguides could be used to achieve higher field enhancement, as required for scanning nanoprobe experiments. Importantly, such a WGA with enhanced focusing capability would also work at high photon energy, since it circumvents the usual volume diffraction of multilayer zone plates. Simulations show that also special effects like a double focus or tilted emission of the beam can be achieved by such WGA structures. A near-field design with a doubled quasi-focal spot, for example, could be used for differential phase contrast imaging. Tilted emission, on the other hand, could be used to increase the effective numerical aperture for holographic recordings. Further, the vary structured and diverse near-field distributions could be very beneficial for ptychographic phase retrieval. Note

that future generalizations of this concept can be directed at two-dimensional control of the near-field distribution by crossing to thin WGA foils, similar to the 2D waveguides described in [27, 28]. We do want to stress, however, that all such applications rely on the brilliance of synchrotron radiation, and are at least currently not compatible with compact x-ray sources. Concerning experimental characterisation, an important next step would also be the reconstruction of the near-field distribution from the measured far-field by iterative phase retrieval. In view of the fact, that 1D structured wavefields are challenging to reconstruct, the bending magnet radiation used in this work which was of very low coherence and very extended in the plane of the WGA has to be exchanged with focused undulator radition, so that the wavefield is confined in two directions and of much higher partial coherence.

Acknowledgments

3 Reconstruction of the near-field distribution in x-ray waveguide array

Qi Zhong, Lars Melchior, Jichang Peng, Qiushi Huang, Zhanshan Wang and Tim Salditt

Iterative phase retrieval has been used to reconstruct the near-field distribution behind tailored X-ray waveguide arrays, by inversion of the measured far-field pattern recorded under fully coherent conditions. It is thereby shown that multiwaveguide interference can be exploited to control the near-field distribution behind the waveguide exit. This can, for example, serve to create a secondary quasi-focal spot outside the waveguide structure. For this proof-of-concept, we use an array of seven planar *Ni/C* waveguides, with precisely varied guiding layer thickness and cladding layer thickness, as fabricated by high precision magnetron sputtering systems. The controlled thickness variations in the range of 0.2 nanometers results in a desired phase shift of the different waveguide beams. Two kinds of samples, a one-dimensional waveguide array and periodic waveguide multilayers, were fabricated, each consisting of seven *C* layers as guiding layers and eight *Ni* layers as cladding layers. There are shown to yield distinctly different near-field patterns.

3.1 Introduction

X-ray waveguides (WGs) enable manipulation of x-ray fields at the nanoscale, based on the optics of guide modes. Similarly to their optical counterparts, they enable optical functions such as collimation, mode selection and coherence filtering [79] as well as beam splitting for interferometry [22], beam tapering [23] or angular redirections [24]. With typical diameters d of the guiding core in the range of a few tens of nanometers, they also form suitable quasi-point sources for x-ray holography [11]. For this application, the length of the waveguide L has to be sufficiently long to absorb all radiative modes in the cladding, re-

quiring L to be in the range between 0.1 to 10 mm, depending on the photon energy. Generally, one distinguishes between one-dimensionally confining planar waveguided [13–18] and two-dimensionally confining channel waveguides (2DWG), which were introduced by [19], and which require advanced electron lithography with interferometric positioning and suitable pattern transfer techniques in order to reach the required aspect ratios. The fabrication of 2DWGs was improved by [20], and more recently extended from overgrown polymer channels to air channels capped by wafer bonding techniques [21, 23]. In this form 2DWGs now serve as fully operational secondary sources for holographic imaging [11]. Notwithstanding this successful development, lithography still lacks the precision to which planar thin films can be fabricated. Therefore, for purposes of highest beam confinement or to exploit novel geometries, wave guiding in only one dimension as in thin planar films is suitable, owing to a better control of layer sequences. For example, in this way the theoretical limits for beam collimation [26], notably 8 nm for the given material could be reached in a planar thin-film waveguide with an optimized cladding material ($Mo/C/Mo$ structure embedded in Ge [27, 28].

X-ray waveguide optics can be generalized from a single guiding film to an array of planar waveguides, enabling more optical functions. For example, using several planar waveguides can serve to increase the coupling efficiency, i.e. to collect more incoming beam intensity by a larger effective entrance cross section. Further, with an optimized material combination, the overall transmission and mode structure could be modulated. Finally, interference and coupling effects between the different guiding layers can be exploited. The generic aspects of coupling x-ray waveguide modes are analogous to other forms of coupled resonators, i.e. mode splitting, lifting of degeneracies and ultimately - when increasing the number of guides - the formation of a quasi continuous spectrum of propagation constants analogous to a band structure. This was first demonstrated by [30], using a planar thin film structure with several planar waveguides, placed in proximity to achieve strong coupling of modes. In these experiments, the collimated synchrotron beam was coupled into the array of waveguides via the so-called resonant beam coupling scheme through the top of the multilayer structure. In other applications [32, 33], the cladding layer instead of the guiding layer was generalized to a multilayer, while keeping only a single guiding layer. In this way, the internal reflection angles of guided beams could be increased. Periodically structured claddings could also be useful to realize other coupling geometries, namely Bragg couplers. Recently, we have introduced a further multilayer concept to x-ray waveguide optics, which we denote as a waveguide array (WGA) [80]. A WGA consists of an array of planar

waveguides with individually tailored guiding layer thickness and hence propagation constants. Further, the individual guides are separated at distances large enough to avoid coupling. We have proposed this novel scheme to achieve special multi-beam interference patterns outside the waveguide after coupling out a number of beamlets with tailored phase and position.

In contrast to the waveguides introduced by [30], the WGA must be operated in front-coupling geometry. After coupling of the beam in the front side, the radiation is guided in the multiple waveguides, before the beamlets are finally coupled out at the other side of the structure. Spurious reflected or transmitted beams are removed, since the waveguides are embedded in a non-transparent cladding. Importantly, by variation of the guiding layer thickness d_i for each waveguide i individually, the phase in the exit plane of the waveguide is controlled for each waveguide beamlet individually. In this way, the phase relations between the different guided beams can be tailored to produce special near-fields behind the WGA's exit by multi-waveguide interference [80]. Hence, near-field intensity distributions with special properties can be realized, e.g. creating a secondary quasi-focal spot in free space. For example, in our previous work we use seven planar waveguides with precisely designed layer thickness variations, fabricated by high-precision direct-current magnetron sputtering of carbon (C) and molybdenum (Mo), with systematic thickness variations of the order of 0.2 nm. To this end, the design of the structure must be guided by numerical simulations of field propagation, notably finite-difference (FD) simulations, which predict a beam intensity maximum with a spot size ($FWHM$) in the sub-50 nm range located in free space behind the WGA at 19.9 keV hard x-ray energy.

In the present paper we show that multi-waveguide interference as introduced by [80] can actually be verified experimentally by reconstructing the near-field from the measured far-field diffraction pattern, on the basis of iterative phase retrieval algorithms. Contrary to the approach of [80], where the far-field distribution was simulated by using a precise layer combination in a WGA model, this work enables a much more direct visualisation of the near-field interference pattern and a better comparison with the theoretical design. To illustrate the specific field modulating effects which can be achieved by a symmetrical variation of the waveguide width d_i for each waveguide i, we have investigated the near-field of two different kinds of waveguide structures, namely the aforementioned waveguide array (WGA) and - for comparison - a simpler periodic waveguide multilayers (WGM), respectively. The WGA has taylored width d_i ($i = 1, ..., 7$) and corresponding cladding layer thickness c_j ($j = 1, ..., 8$) and c_{j+1} for each waveguide, designed for particular interference effects [quasi-focus,

double focus etc. , as discussed in [80]]. In contrary, the WGM is a periodic arrangement of the same waveguide structure with constant guiding layer d and cladding layer c. To some extent, the WGM can be regarded as a control sample for the WGA. In both cases, the examples given are structures with a total of $i = 7$ and $j = 8$ layers, and the guiding layer was composed of amorphous C, while the cladding layer was made of polycrystalline Ni [80].

With respect to our earlier work [80], two major experimental steps forward have enabled the successful field reconstruction presented here. Firstly, we have extended the synchrotron experiment from partially coherent bending magnet radiation to highly brilliant undulator radiation (with substantially higher spatial coherence). Secondly, we use a pre-focused beam so that the field is confined in the xy plane perpendicular to the optical axis z. Note that the phase problem in one-dimensional geometries is generally not amenable to phase retrieval by iterative algorithms (non-uniqueness). Therefore, the changes both in support (focused in xy rather than extended in y) and in geometry (two-dimensional diffraction pattern rather than line scan) were instrumental. Specifically, the near-field distributions for the WGA and WGM are retrieved from the experimental far-field pattern by using the error-reduction algorithm [27, 61, 62]. The complex-valued field distribution in the exit xy plane (amplitude and phase) can then be propagated along the z axis, and can be compared with the FD calculations of the designed WGA parameters.

The paper is organized as follows. § 2 describes the design of the Ni/C WGA and optical field simulations. § 3 describes the fabrication and characterization of the transmission electron microscopy (TEM) samples. § 4 then presents the experimental parameters and results, leading to the near-field reconstruction, before the paper closes with a brief summary and outlook in § 5.

3.2 Design and simulations

The WGA is designed to work as a front-coupled waveguide, as illustrated in Fig. 3.1(a). The synchrotron beam is coupled in, guided in the set of parallel planar layers and then coupled out, to yield the desired near-field pattern in the free space behind the WGA. The exit beam is subsequently broadened again by diffraction and finally diverges to the far-field pattern, which is the main experimental observable. Before addressing the WGA structure designed in this work, we first repeat the basic optical concept of the WGA. The incoming beam of photon energy E and primary intensity I_0, is coupled into the Ni/C WGA with working length L. The WGA tailors the near-field to the desired shape, e.g. form-
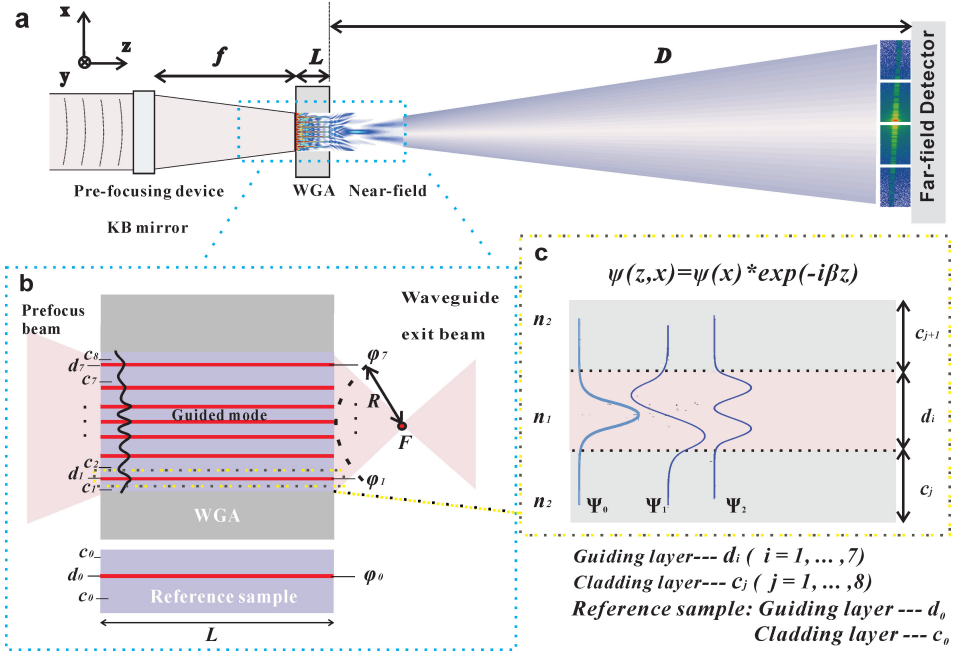
Figure 3.1: *(a) Schematic of the experimental setup. The X-ray waveguide array (WGA) is positioned at f, which is the distance from the exit of the Kirkpatrick-Baez (KB) device to the sample. The incoming beam with photon energy E and primary intensity I_0, is coupled into the Ni/C WGA with working length L, which tailors the near-field to the desired shape. The far-field intensity distribution is recorded at a distance of D behind the WGA exit by a two-dimensional pixel detector; (b) The schematic structure of the WGA consists of seven guiding layers in red (d_i, $i = 1,...,7$) and eight cladding layers in purple (c_j, $j = 1,...,8$). After the pre-focus beam has been coupled, the guided mode is produced in the different guiding layers. With the working length L, the exit phase φ_i from corresponding the guiding layers i can be controlled by the variation of the layer thickness d_i. The parameters at the exit of the WGA can be optimized such that the lines of the exit phase φ_i describe a circle with radius R, resulting in constructive interference in a quasi-focal spot (F) outside the WGA. The phase of the reference sample with length L is φ_0, with the corresponding guiding layer (d_0) and cladding layers (c_0); (c) Sketch of a slab waveguide with two cladding layers c_j and c_{j+1}. Under the influence of the electric field inside the waveguide [$\psi(z,x) = \psi(x)exp(i\beta z)$], the symmetrical guided modes (ψ_0, ψ_2) and the asymmetrical mode ψ_1 propagate inside the guiding layer depending on the different layer thickness d_i.*

ing a quasi-focus spot. The two-dimensional far-field intensity distribution is recorded at a distance of D behind the WGA exit by a two-dimensional detector. As shown in Fig. 3.1(b), the WGA, consisting of seven guiding layers ($i = 1,...,7$) in red and eight cladding layers ($j = 1,...,8$) in purple, produces a guided mode in each guiding layer i. Let us briefly consider the beam propagation in a slab

waveguide i with working length L and initial guiding layer thickness d_0. The guiding layer (C) thickness is d_i, and the thickness of the adjacent two cladding layers (Ni) are c_j and c_{j+1} as shown in Fig. 3.1(c). The refractive indices of the guiding and cladding layers are n_1 and n_2, respectively.

The field in the waveguides can be calculated by the reduced Helmhotz equation [34, 36],

$$d^2 E_y / dx^2 + [k_0^2 n^2(x) - \beta^2] E_y = 0, \tag{3.1}$$

where β is the propagation constant, and the wave vector k in z-direction is given as $k = nk_0$ in the corresponding medium. For $k_0^2 n_2^2 \leq \beta^2 \leq k_0^2 n_1^2$, the solution of Eq.(3.1) for symmetrical modes can be written as

$$E_y^{sym}(x) = \begin{cases} A\cos(\kappa x), & |x| \leq d/2, \\ C e^{-\gamma |x|}, & |x| > d/2, \end{cases} \tag{3.2}$$

where the parameters of the solution are linked to β according to $\gamma^2 = \beta^2 - k_0^2 n_2^2$ and $\kappa^2 = k_0^2 n_1^2 - \beta^2$. Continuity at the interfaces then leads to a discrete set of solutions, which are determined from the transcendental equations

$$\xi \tan \xi = \left[\left(\frac{V}{2} \right)^2 - \xi^2 \right]^{1/2}, \tag{3.3}$$

Here, the waveguide parameter is $V = k_0 d (n_1^2 - n_2^2)^{1/2}$, and the propagation constant is $\beta = (k_0^2 n_1^2 - 4\xi^2 / d^2)^{1/2}$.

After a Taylor series expansion [80], the relationship between the propagation constant β and the guiding layer thickness d for symmetrical modes becomes

$$\frac{\partial \beta}{\partial d} \approx \frac{\Delta \beta}{\Delta d} = \frac{k_0^2 n_1^2}{d_0 \beta_0} - \frac{V_0^2}{d_0^3 \beta_0 (1 + \frac{\xi_0 \sin \xi_0}{\cos^3 \xi_0} + \tan^2 \xi_0)} - \frac{\beta_0}{d_0}. \tag{3.4}$$

Therefore, the propagation constant β and hence the phase of the exit beam can be controlled by variation of the guiding layer thickness. For the experimental materials and parameters $E = 8$ keV and $d_0 = 18$ nm, we obtain $\partial \beta / \partial d \simeq 1.24542 \times 10^{-5}$. To optimize the thickness values of the seven guiding layers $(i = 1, ..., 7)$, we first determine the required exit phase φ_i as presented in our earlier work [80]. The phase of a beamlet from the reference sample, as shown in Fig. 3.1(b) is φ_0 for constant L and a given (initial) guiding layer thickness d_0. Physically, only the relative phase difference $\Delta \varphi_i = \varphi_0 - \varphi_i$ matter for the near-field distribution. The propagation constants then follow from $\Delta \beta_i = \Delta \varphi_i / L$. Finally, with the corresponding slight changes in the guiding layer thickness $[\Delta d_i = \Delta \beta_i / (\partial \beta / \partial d)]$, the seven guiding layer thicknesses of the WGA

[$d_i = d_0 - \Delta d_i$] are calculated. After propagating over a distance L in the WGA, the value of the exit phase φ_i is thus determined by the corresponding guiding layer d_i. Note, however, that the numerical simulations presented below are not using this approximation.

This phase and the layer positions are the main parameters to optimize and design specific near-field distributions. The parameters of the WGA can be optimized such that the lines of the exit phase φ_i describe a circle with radius R, as shown in Fig. 3.1(b), which results in a quasi-focus point F in the near-field. When the initial guiding layer thickness ($d_0 = 18$ nm) is set, R is mainly influenced by the cladding layer thickness c_j. With increasing c_j, the interference point F moves farther away from the exit plane of the WGA. From this analysis, it appears that several interesting refraction and interference phenomena can occur in the WGA structure and free space, and can easily be controlled by changing the cladding layer thickness c_j.

To illustrate the field modulating effects that can be achieved by a symmetrical variation of the waveguide width d_i, we have simulated the near-fields for two different kinds of waveguide structures, WGA and WGM. Both consist of seven C layers and eight Ni layers. Using the different guiding layer thickness d_i and cladding layer thickness c_j to control the exit phase φ_i in the WGA, a quasi-focus spot F can be created as introduced by [80]. To emphasis the controlled phase φ_i in the WGA structure, a simple periodic structure WGM is used as a reference, with parameters given in Table 3.1. Based on the FD calculations presented in [20], the electromagnetic field inside the WGA and WGM are simulated for an X-ray energy of 13.8 keV. We perform simulations for the waveguide lengths $L_1 = 0.26$ mm (Fig. 3.2(a) and (c)) and $L_2 = 0.52$ mm (Fig. 3.2(b) and (d)) for WGA and WGM, respectively. In the case of the WGA, the relative intensity I/I_0 and $FWHM$ of the quasi-focal spot are 0.16870 and 22.0 nm in Fig. 3.2(a) for $L_1 = 0.26$ mm, compared to $I/I_0 = 0.04759$ and $FWHM$ of 25.8 nm in Fig. 3.2(b) for $L_2 = 0.52$ mm. Compared to Mo/C WGA considered in our earlier report [80], where we presented simulations with a quasi-focus spot of $FWHM$ 37.2 nm, located at 180.0 μm behind the exit, the Ni/C WGA used in the present work exhibits a higher numerical aperture and a more desirable near-field distribution owing to the variations in cladding layer thickness c_j, yielding a focal spot at 224.6 μm behind the device, with an $FWHM$ of 22.0 nm. The field distribution in free space behind the WGM is quite similar for the different optical length L_1 (Fig. 3.2(c)) and L_2 (Fig. 3.2(d)). Hence, the length of the WGM is not as important as the layer structure itself.

For comparison, we also present the field distribution of a single WG (Ni [52 nm] / C [18 nm] /Ni [52 nm]) on a Ge substrate (see Fig. 3.2(e)).
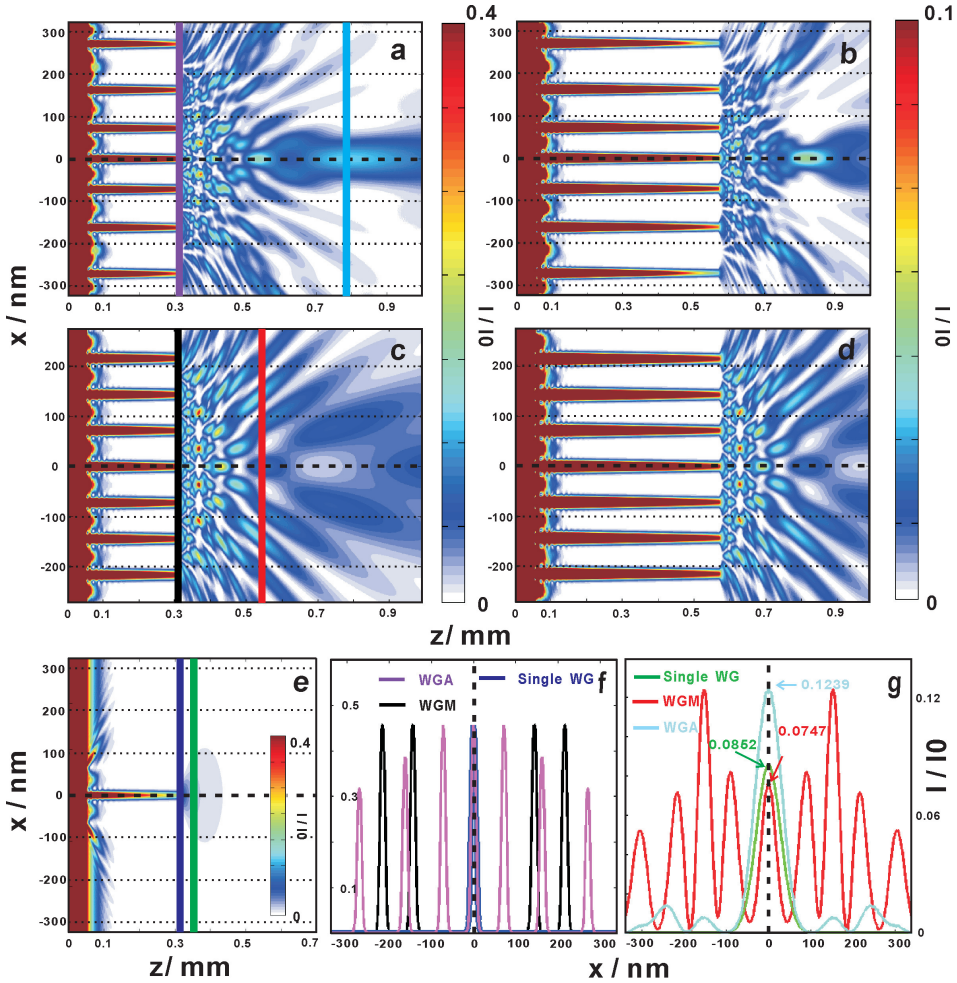
Figure 3.2: *On the basis of the design parameters from Table 3.1, field propagation in the WGA and the WGM were simulated in the near-field by FD calculations, with the incoming plane wave of unit intensity and 13.8 keV photon energy. The simulations are for waveguide lengths $L_1 = 0.26$ mm [(a) and (c) for the WGA and WGM, respectively] and $L_2 = 0.52$ mm [(b) and (d), respectively]. (e) The field distribution of a single WG (Ni[52 nm] /C[18 nm] /Ni[52 nm]) on a Ge substrate are also calculated for the length L_1. (f) The intensity profiles in the exit plane for the WGA (purple line, (a)), the WGM (black line, (c)) and the single WG (dark blue line, (e)) are compared. (g) Comparison of intensity profiles in the downstream planes, for the WGA (light blue line) at a distance of 0.48 mm from exit, for the WGM (red line) at a distance of 0.22 mm from exit, and the single WG (green line) at a distance of 0.02 mm from the exit. The corresponding intensity I/I_0 of the WGA, the WGM and the single layer at the central positions are 0.1239, 0.0747 and 0.0852, respectively.*

The corresponding one-dimensional intensity profiles for the WGA, WGM and single WG are plotted in the exit plane, and a downstream plane in Fig. 3.2(f), and Fig. 3.2(g), respectively. For the WGA, a quasi-focus point with the intensity I/I_0=0.1239 at a distance of 0.48 mm from the exit is observed.

3.3 Fabrication and characterization

Table 3.1: *The theoretical WGA and WGM designed layers thickness.*

Layer Nr.	c_8	d_7	c_7	d_6	c_6	d_5	c_5	d_4	c_4	d_3	c_3	d_2	c_2	d_1	c_1	Sub
Layer name	Ni top	C	Ni	C	Ni	C	Ni	C	Ni	C	Ni	C	Ni	C	Ni	Si Sub
Waveguide array (WGA)																
Layer thickness /nm	50.0	15.7	92.3	17.2	72.8	17.8	54.2	18.0	54.2	17.8	72.8	17.2	92.3	15.7	50	
Periodic waveguide multilayer (WGM)																
Layer thickness /nm	50.0	18.0	54.0	18.0	54.0	18.0	54.0	18.0	54.0	18.0	54.0	18.0	54.0	18.0	54.0	

To evaluate the performance of a WGA, two kinds of structures have been fabricated. First, a prototypical WGA with the characteristic variations in the guiding layer thickness d_i and the corresponding cladding layer thickness c_j. Second, a simple control structure (WGM) with fully periodic waveguide layers, i.e. with constant d and c. In both cases the guiding layer is composed of amorphous C and the cladding layer of polycrystalline Ni, following the parameters shown in Table 3.1. The 15 layers for each kind of samples (WGA and WGM) were deposited by direct-current magnetron sputtering [66, 71] at the Institute of Precision Optical Engineering at Tongji University, China. The seven C layers and eight Ni layers were deposited on Si substrates alternately, under a base pressure of 3.0×10^{-4} Pa. The sputter gas was Ar with purity of 99.999%, and the gas pressure was kept constantly at $1.50 \pm .02$ mTorr (0.1995 Pa). The bonding process was carried out after the fabrication, following [28]. The structures were bonded to an Si wafer, by a $In52Sn48$ alloy layer (GPS Technologies GmbH, indalloy number 1E), and using a vacuum oven at 250° for one hour, keeping the base pressure at 1×10^{-1} Pa. Afterwards, the WGA was sliced into $L_1 = 0.26$ mm, and the WGM was sliced into a $L_2 = 0.52$ mm thick samples, ready for the synchrotron experiments. These were carried out at the GINIX (Goettingen Instrument for Nano-Imaging with X-rays) experimental setup, installed at the

P10 beamline at the PETRA III synchrotron facility in Hamburg (DESY). The far-field diffraction pattern of the waveguided beams leaving the structures were recorded by a Eiger 4M pixel detector (Dectris). The x-ray energy was set by a $Si(111)$ channel cut monochormator to 13.8 keV. The setup is described in detail in [12]. In the experiment, the focusing of the synchrotron radiation by the KB mirros has to match such that the focal spot size is larger (but not very much larger) than the WGA, which is 658.00 nm (design structure as shown in Table 3.2). With fully opened entrance slits in front of the KB mirrors, the beam size at GINIX was around 295 nm × 181 nm in x and y directions. Therefore, experiments were carried out with smaller slits, notably with a 50 μm slit size, to achieve a spot size broadened by diffraction, see also the ptychographic probe reconstructions presented in [81]. Moreover, this setting warrants full spatial coherence.
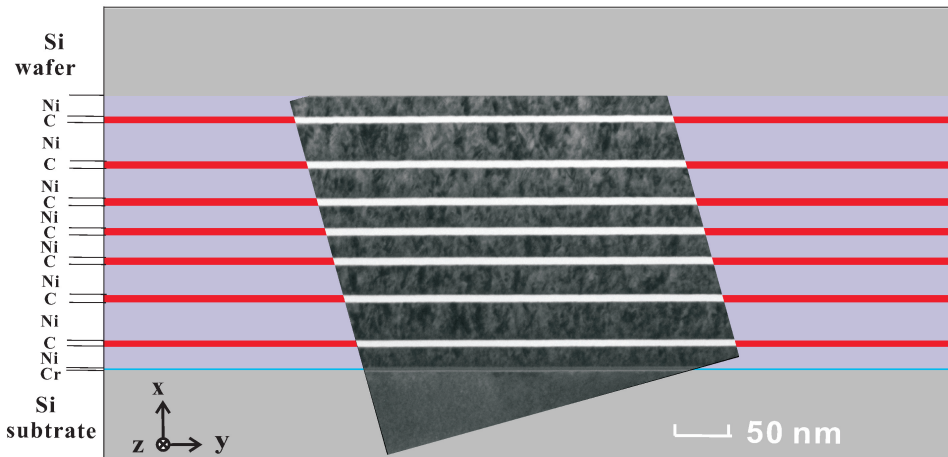
Figure 3.3: *The TEM images of the cross section of the multilayer with seven C guiding layers and eight Ni cladding layers in the WGA structure, bonded to an Si cap wafer. Scale bar 50 nm.*

Compared to the periodic structure of the WGM, the layer parameters of the WGA are more critical and therefore have to be precisely characterized before the synchrotron experiments, in order to verify whether the design parameters have been reached [80]. To this end, the TEM (using a Philips CM 200 FEG-UT) was used to determine the layer thicknesses for slices cut out by a focused ion beam (FIB, FEI Nova Nanolab 600). Several transmission electron micrographs were acquired with partial overlap to cover the WGA cross section (see Fig. 3.3). The scale bar represents 50 nm and the pixel size is 0.45 nm. The averaged layer

thickness values in several micrographs over 52 line cuts of different parts of the TEM specimen were calculated, with error bars of ±0.45 nm, as shown in Table 3.2.

Table 3.2: ***Design parameters and averaged layer thickness as determined by TEM for the WGA structure.***

Layer Nr.	c_8	d_7	c_7	d_6	c_6	d_5	c_5	d_4	c_4	d_3	c_3	d_2	c_2	d_1	c_1	Total thickness /nm
Layer name	Ni	C	Ni	C	Ni	C	Ni	C	Ni	C	Ni	C	Ni	C	Ni	
Theoretical design results																
Layer thickness /nm	50.00	15.70	92.30	17.20	72.80	17.80	54.20	18.00	54.20	17.80	72.80	17.20	92.30	15.70	50.00	658.00
TEM reading averaged results, error bar ± 0.45 nm																
Layer thickness /nm	51.36	15.40	95.60	16.87	76.16	17.19	57.05	17.60	57.10	17.15	76.60	16.16	96.37	14.62	52.29	677.52

3.4 Results

Fig. 3.4 presents the measured far-field patterns of the WGA and WGM, on a logarithmic scale, as recorded with the Eiger 4M pixel detector (Dectris), with pixel size 75 μm, placed at $D = 5.4$ m behind the focal plane of the KB mirrors. With an X-ray energy of 13.8 keV, the *Si* wafers of both the WGA $L_1 = 0.26$ mm and the WGM samples $L_2 = 0.52$ mm are semi-transparent, so that besides the waveguide exit beam there is also a contribution of the primary beam. To minimize this contribution, the detector was aligned such that the primary beam fell onto the inter-module gaps of the detector (with additional attenuation of the beam), as shown in Fig. 3.4(a) and (b), well separated from the extended multilayer signal (vertical stripes). The total accumulation time for the two-dimensional far-field pattern was 10 s, distributed over ten frames. We see that the signal of the WGA is distinctly different from that of the WGM, which exhibits the expected periodic diffraction orders, extending over the entire detector. To better compare the differences of the two structures, the two-dimensional far-field patterns of WGA and WGM are integrated in *y* direction to yield the corresponding one-dimensional profiles [see, respectively, the blue and red curves in Fig. 3.4(c)]. In both one- and two-dimensional representation, the "grating" character of the WGM becomes apparent, representing a regular and periodic far-field pattern.

To further corroborate the correct optical functioning of the WGA, we perform
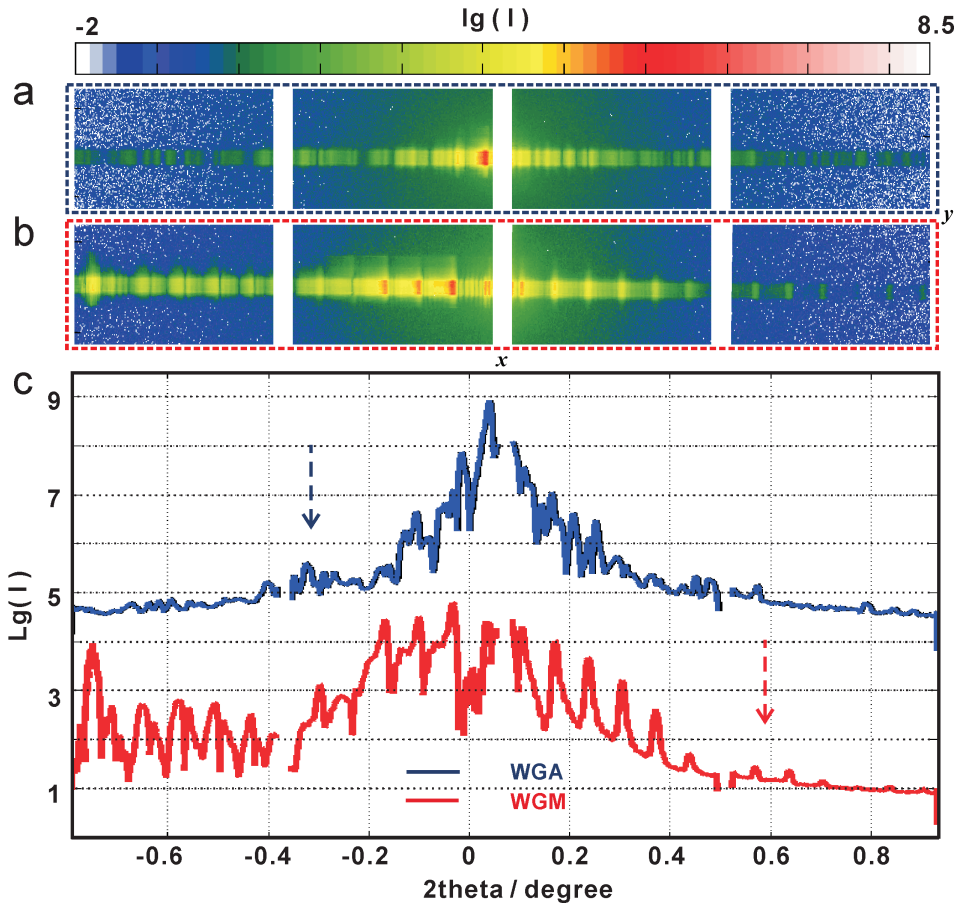
Figure 3.4: *The measured two-dimensional far-field pattern of the WGA (a) and WGM (b) at 13.8 keV, recorded with the Eiger 4M pixel detector at a distance of D = 5.4 m behind the structures. (c) The integrated one-dimensional far-field curves, corresponding to (a) and (b).*

a reconstruction of the complex-valued near-field distribution from the measured far-field pattern (two-dimensional), using two different well established phase retrieval algorithms [63, 64], the error reduction (ER) algorithm and hybrid input-output (HIO) algorithm [61, 62]. Fig. 3.5(a) illustrates the procedure of the iterative reconstruction scheme. The algorithm is initialized with a guess of the wavefield in the object plane (xy). The iteration consists of (i) forward propagation (implemented numerically by a fast Fourier transform) to the far-field detector plane (XY plane), where the wavefield $U(X, Y)$ is subjected to a an amplitude constraint (measured data), resulting in $U_{update}(X, Y)$, followed
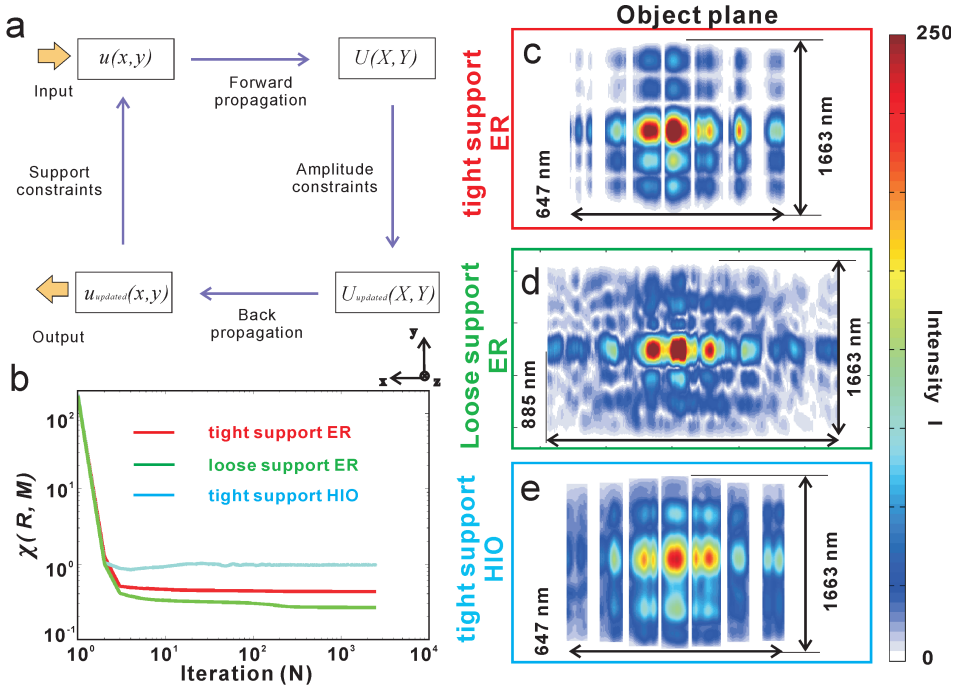
Figure 3.5: *(a) Schematic of the iterative reconstruction scheme. (b) Error metrics for the tight support using ER algorithm (red line), the loose support using ER algorithm (green line), and the tight support using HIO algorithm (light blue line). The reconstructed wavefronts are shown after N = 2500 iterations, for (c) the tight support using ER algorithm (size: 647 nm × 1663 nm in x and y directions), (d) the loose support using ER algorithm (size: 885 nm × 1663 nm in x and y directions), (e) the tight support using HIO algorithm (size: 647 nm × 1663 nm in x and y directions).*

by (ii) back-propagation to the object plane, where the field $u_{update}(x, y)$ is projected onto the support, resulting in the next input of the cyclic iteration. The experimental parameters, namely the 2167 pixels along the wide direction of the Eiger detector, the pixel size $Px = 75$ μm, the detector distance of $D = 5.4$ m, and the wavelength $\lambda = 0.898$ Å, resulted in a pixel size in the object plane of $px = 2.98$ nm. Note that this pixel size is the fundamental limit of the resolution in the growth direction of the WGA, provided consistent phase retrieval up to the edge of the detector, where the signal (in q_x direction) is still sufficiently strong. Specifically, two different supports were tested, denoted by 'tight' support and 'loose' support, as visualized in Fig. 3.5(c) and (d), respectively. The tight support constraints the field in x direction were derived from the known parameters of the WGA geometry (design values plus some tolerance, width 647

nm), while the support in y direction (1663 nm) was selected to be much larger than the incoming beam size in y direction.

Contrarily, the loose support corresponds to a rectangle of size 885 nm and 1663 nm in x and y directions, respectively. Note that the primary beam (PB) is not completely absorbed by the WGA and gives a signal in the central maximum of the detector. The corresponding pixels must hence be masked in the projection onto the measurement. To compare the robustness and validity, the ER and HIO phase retrieval algorithms were used, as shown the corresponding object planes in Fig. 3.5(c) and (e). Both were run for $N = 2500$ iterations. Fig. 3.5(b) presents the error metrics for three different cases: tight support using ER algorithm (red), loose support using ER algorithm (green) and tight support using HIO algorithm (light blue). The error metric is computed by [64]

$$\chi(R, M) = \sqrt{\frac{\sum |R - M|^2}{\sum |M|^2}} \, , \tag{3.5}$$

where the summation is over all pixels of the field R (reconstructed pattern) and M (measured pattern). The error of the tight support using ER algorithm is smaller than that using HIO algorithm, which is in line with the general experience with similar phase retrieval problems. Since ER is a local, and HIO a non-local optimisation, it is often a good strategy to use first HIO and then ER. In the present case, such combinations of HIO and ER were also tested but gave less convincing results than the ER initialized with amplitude data and a flat phase profile. Importantly, for all three reconstructions the beamlets exiting from the WGA can be clearly discerned, as indicated in Fig. 3.5(c, d, e). At the same time, the field configurations show differences, which may indicate that the loose support is too 'weak' as a constraint. The tight support may also be affected by a small systematic error, since the structure was partially transparent. Owing to the smaller error and most convincing pattern, we primarily compare the results of tight and loose support using the ER algorithm in the following discussion.

Fig. 3.6 shows a comparison of the measured far-field pattern shown in (a) with the reconstructed far-field pattern, corresponding to (b) the tight and (c) the loose support, along with the corresponding line profiles, shown in (d). Note that concerning the experimental data, we have combined the measured data with same accumulation time from two detector positions (x_1 and x_2) into one (fused) dataset. The three blank regions in the experimental data (x_1 as shown in Fig. 3.4(a)) is filled with values from the data in x_2, resulting in the combined (fused) data set shown in Fig. 3.6(a). The profile of the loose support (green line) is highly consistent with the measured data (blue line). For this reason, we select the results from the loose support in the subsequent comparison of field

propagation.

Fig. 3.7 shows the results for the WGM control structure, again comparing (a) the measured and (b) the reconstructed diffraction pattern, as well as the (c) the reconstruction in the object plane. Note that in this case only the tight support gave a satisfactory reconstruction. The support used is also shown in Fig. 3.7(c) and consists of seven strips of 22 nm width separated by gaps of 50 nm width in a 454 nm × 1747 nm (x and y directions) rectangular field. The corresponding one-dimensional far-field pattern in Fig. 3.7(d) shows a satisfactory agreement between reconstruction (black line) and measurement (red line).

Next, we compute the near-field propagation along the optical axis z, starting
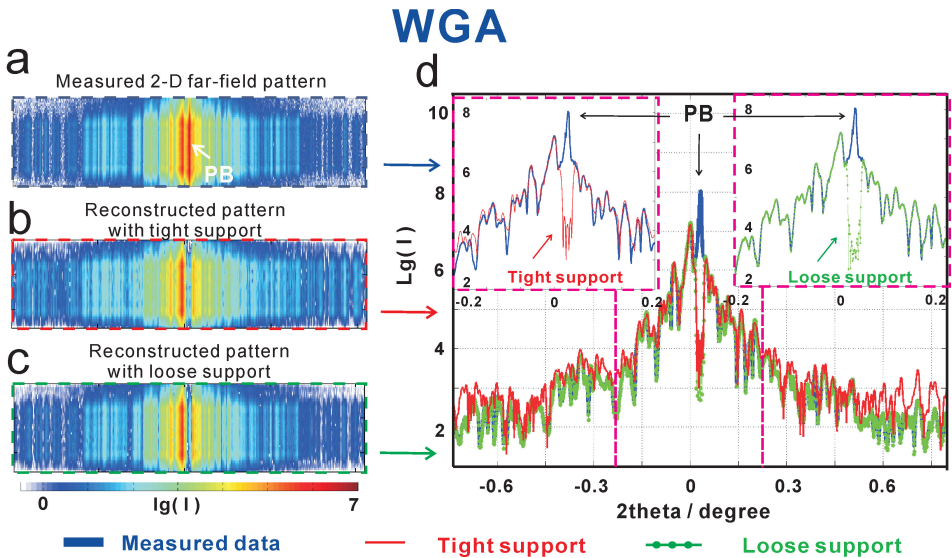
Figure 3.6: *The two-dimensional measured far-field pattern with the transmitted primary beam (PB) of (a) the WGA, compared with the reconstructed results of (b) the tight support and (c) the loose support. (d) The corresponding one-dimensional profiles, after integration along the y direction: measured far-field (blue line), reconstruction with the tight support (red line), and reconstruction with the loose support (green line).*

from the complex-valued field in the reconstruction plane, and compare this to the simulation according to the (ideal) design values. To this end, we carry out FD simulations in two different dimensional settings: Simulations denoted as 1+1 dimensional have one dimension along the optical axis z and one dimension x orthogonal to the optical axis parallel to the normal vector of the thin film interfaces. Simulations denoted as 2+1 dimensional take into account both dimensions orthogonal to the optical axis, i.e. also the direction y, in which
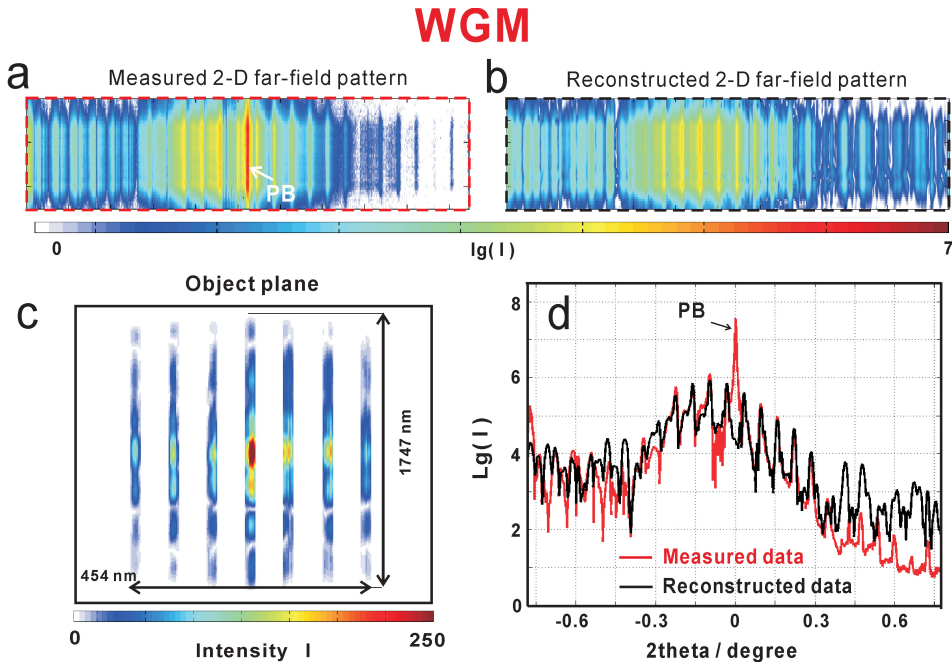
Figure 3.7: *Reconstruction for the WGM (periodic control structure). (a) the two-dimensional measured far-field pattern with the transmitted PB, and (b) reconstructed far-field pattern. (c) The corresponding reconstructed object plane (size: 454 nm × 1747 nm). (d) The integrated one-dimensional profiles for the measured data (red line) and reconstruction (black line).*

the planar waveguide is translationally invariant. Fig. 3.8(a) shows the design (ideal) field distribution obtained from the FD simulations (simulated in 1+1 dimension), with the yellow dashed line indicating the quasi-focus in plane P_1 (xy plane) at a distance z = 226.0 μm. Fig. 3.8(b)) shows the pattern in the P_1 plane (xy plane), as calculated in 2+1 dimensions. These results can be compared with the experimental reconstruction results with the loose support in Fig. 3.8(c) and (d), based on using the parabolic wave equation [20]. The quasi-focus point is at 247.1 μm in the P_2 plane (white dash line). We see that the field distribution is only in qualitative agreement. This can be expected from the deviations in the layer parameters from the design values (see Table 3.2). In addition, the experimental setting was not perfect, since the incoming beam intensity was probably not constant over the entire structure range, as indicated by the reconstructions of the exit wave. Importantly, however, the quasi-focal spots are still observed in the experimental result. The $FWHM$ of the quasi-focal spot in the P_2 plane is 45.0 nm (Fig. 3.8(d)) along x, which are not much

Figure 3.8: *Near-field distribution for (a, b) design WGA, (c, d) measured WGA, (e, f) control structure WGM in theory and (g, h) measured WGM. (a) Design-WGA: one-dimensional FD simulation for the parameters of the design WGA structure, showing 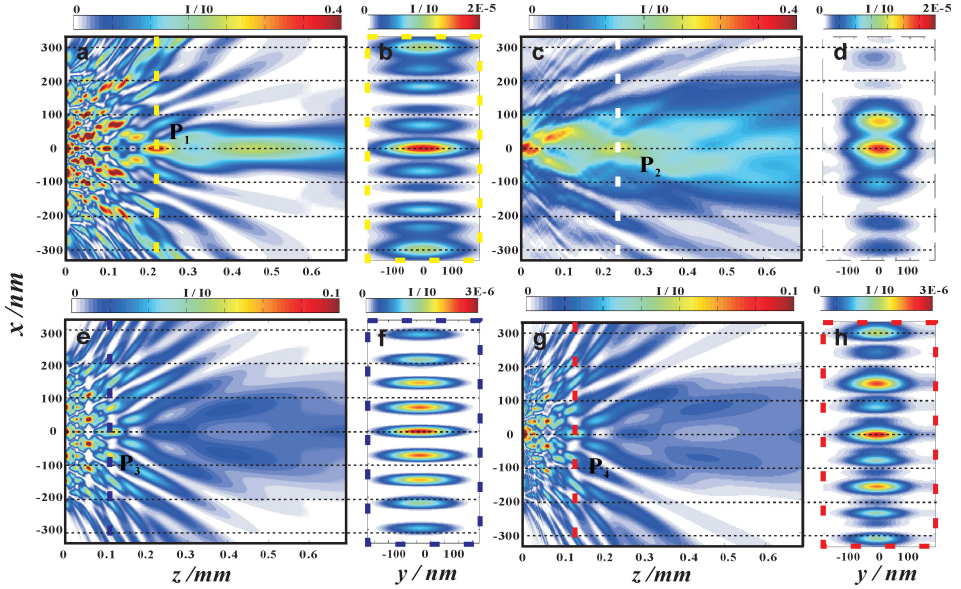the field in free space behind the exit plane of the WGA. (b) Design-WGA: the field distribution in the P_1 xy plane, corresponding to the yellow dashed line in (a), calculated by full two-dimensional FD simulations. (c) Measured-WGA reconstructed by the loose support: one-dimensional free propagation by using the parabolic wave equation in 1+1 dimensions ($x + z$ dimensions) [20], starting from the reconstructed near-field pattern of the WGA [reconstruction data corresponding to Fig. 3.5(d)]. (d) Measured-WGA reconstructed by the loose support: the field distribution in the P_3 xy plane, corresponding to the white dashed line in (c), calculated by the parabolic wave equation in 2+1 dimensions ($xy + z$ dimensions). (e) Design-WGM: one-dimensional FD simulation for the parameters of the design WGM structure, showing the field in free space behind the exit plane of the WGM. (f) Design-WGM: the field distribution in the P_3 xy plane, corresponding to the dark blue dashed line in (e), calculated by full two-dimensional FD simulations. (g) Measured-WGM: one-dimensional free propagation by using the parabolic wave equation in 1+1 dimensions, starting from the reconstructed near-field pattern of the WGM [reconstruction data corresponding to Fig. 3.7(c)]. (h) Measured-WGM: the field distribution in the P_4 xy plane, corresponding to the red dashed line in (g), calculated by the parabolic wave equation in 2+1 dimensions.*

larger than the design values of 22.0 nm (Fig. 3.8(b)).

Furthermore, as desired, the field distribution of the WGA is significantly different from the WGM control structure as shown in Fig. 3.8(e-h). In this case (WGM), the field distribution is again calculated from the WGM experimental values (field reconstruction with tight support). The near-field pattern (Fig.

3.8(g, h) is very close to the simulated one (Fig. 3.8(e, f)). Note that the intensities are lower than for the WGA, owing to the longer working length L_2 and correspondingly higher absorption. Importantly, the interference pattern have no obvious central peak as for the WGA. We conclude that the reconstructed field pattern for the WGA (both in 1+1 dimension and 2+1 dimensions) shows the characteristic features of the design structure, supporting the concept of near-field control by variation of guiding layer thickness.

3.5 Discussion and Conclusion

In summary, we have reconstructed the near-field distribution of an Ni/C X-ray waveguide array (WGA) from the measured far-field data. To this end, we have used two different supports (the tight support and the loose support). Phase retrieval of one-dimensional structures is known to be problematic. Despite the fact that the experiment has used a focused beam and a two-dimensional detection scheme, and hence falls into the (nominal) category of two-dimensional, the variation of the signal is essentially one dimensional. For this reason we had anticipated that we could require as much support information as possible, and have therefore used the strong *a priori* information of position of the seven waveguide channels (the beamlets). However, in the case of the WGA a tight support did not turn out to be necessary, and the loose support actually gave smaller errors in the reconstruction. The reconstruction results are quite robust. The coarse pattern of the reconstructed field was similar in both cases. Contrarily, for the periodic WGM, the tight support turned out to be necessary, which is not surprising given the known difficulty associated with phase retrieval of periodic structures. Therefore, the constraints have to be tightened. Note that we also performed one-dimensional phase retrieval based on detector data summed over the columns. As expected, these reconstructions were less stable.

Using the two-dimensional phase retrieval, we could validate the concept of tailored near-field distributions, put forward before on the basis of analytical theory and numerical simulations. According to this concept, the multi-beam interference pattern is controlled by variation of both seven C guiding layer thicknesses and eight Ni cladding layer thicknesses in the experiment. This leads to beam intensity modulations in the free space behind the waveguide exit, which are distinctly different from those obtained for a WGM with constant seven C guiding layer thicknesses and eight Ni cladding layer thicknesses. In particular, quasi-focal spot sizes in the sub-50 nm range can be generated. In future,

such tailored near-fields exhibiting large structural diversity can be used for coherent imaging, for example by ptychography [82–84], which has been shown to benefit from a highly structured illumination wavefield. Note that, not only for imaging applications but also as a more powerful probe reconstruction for inspection of the WGA near-field, ptychography is an obvious extension for future work. Finally, we suggest that future generalizations of the WGA concept could include design of twin peaks for differential phase contrast, or emission of radiation directed away from the optical axis (off-axis), similar to the optics of distributed antenna in other spectral ranges.

Acknowledgments

4 The Goos-Hänchen effect observed for focused x-ray beams under resonant-mode-excitation

Qi Zhong, Lars Melchior, Jichang Peng, Qiushi Huang, Zhanshan Wang and Tim Salditt

We have coupled a nano-focused synchrotron beam into a planar x-ray waveguide structure through a thinned cladding, using the resonant beam coupling (RBC) geometry, which is well established for coupling of macroscopic x-ray beams into x-ray waveguides. By reducing the beam size and using specially designed waveguide structures with multiple guiding layers, we can observe two reflected beams of similar amplitudes upon resonant mode excitation. At the same time, the second reflected beam is shifted along the surface by several millimeters, constituting a exceptionally large Goos-Hänchen effect. We evidence this effect based on its characteristic far-field patterns resulting from interference of the multiple reflected beams. The experimental results are in perfect agreement with finite-difference simulations.

4.1 Introduction

Planar waveguide for hard x-rays are nowadays well established [13–18]. They can be simply realized by a thin film structure consisting of a low density (guiding) layer sandwiched in between layers of high density, the so-called cladding layer. Planar x-ray waveguide can hence be fabricated by a thin film deposition techniques with sub-nm control. Planar x-ray waveguide can be used for the definition of nanometer-sized highly coherent x-ray beams, for mode filtering [79], and for x-ray holographic imaging [11]. More complex structures can be realized by extending and generalizing the sequence of thin film layers. In [30], multiple guiding layers separated by thin claddings were used to exploit coupling between several guided beams. Several coherent beams were

extracted at the end of the waveguide, and evidenced by measuring the far-field interference pattern. More recently, waveguide arrays with multiple guiding layers (WGA) where tailored in the guiding layer thickness and position, to achieve a quasi-focusing in the field behind the waveguide exit [80].

Two different geometries are typically used to couple a synchrotron beam into a waveguide. Either the *front coupling* scheme, where the beam is coupled through the front face directly into the guiding layer [25, 27], or the *resonant beam coupling* (RBC) scheme, where the beam enters from the side through a thinned cladding, usually the top face [35, 42–44]. In this case, the guided modes are resonantly excited by shining a parallel beam onto the waveguide under grazing incidence using a precisely controlled incidence angle α_i for each modes. In order to couple into the guiding layer, the evanescent tail of the parallel beam is used, which "reaches through" the thinned top cladding. The illuminated surface area of the planar waveguide (footprint) is typically a few millimeters long. Resonant mode excitation manifests itself in the plateau of total in the form of sharp dips (cusps) at a set of α_i. At these angles, photons "get trapped" under the resonance conditions in the guiding layer propagating parallel to the surface over an active coupling length [30]. Similar resonant effects - albeit with lower quality factor - can be observed in thin film samples with more general layer sequence (which do not form a waveguide as such) [85]. For infinite samples and beams, the cusp arises since photons are more likely to get absorbed, when photons are coupled into the structure, rather than being reflected at the top. If the footprint reaches the edge of the RBC, the guided beam may also exit at the side. The lateral shift of a waveguided radiation before being reflected can also be regarded as a special manifestation of the Goos-Hänchen effect, well known in the optical regime [46, 47, 49–51, 53, 54, 86]). For visible and near-infrared radiation, it was also shown that this effect can become particularly strong for resonant grating waveguide structures, and can be accompanied by generation of multiple reflected beams [87, 88].

In this work, we study the coupling of finite (sub-μm) x-ray beams into RBCs with three guiding layers in the $[Ni/C]_3/Ni$ structure. Using specially designed structures and resonant mode excitation, the Goos-Hänchen effect results in a enormous shift in the reflected beam of several millimeters. Since part of the incident beam is directly reflected without coupling, one can then face a peculiar situation with two (or even more) reflected beams of almost equal amplitude. In other words, optical simulation shows that multi-guide RBCs can be used as coherent beam splitters, with possible future applications in interferometry or holography. Furthermore, such devices could possibly also serve to split and delay ultra-short x-ray pulses. The goal of the present work is hence to shed light

on this novel phenomenon, using both optical simulations and an experimental proof-of-concept.

For conventional use of RBCs, the standard simulation tool is a transfer matrix algorithm similar or the well known Parratt formalism [89]. The reflected and transmitted intensity, as well as the internal and external standing electromagnetic field can then be plotted as a function of the structural parameters of the RBCs (layer thickness, composition and density, interface roughness) as a function of α_i. Tacitly, such simulations assume infinite beams and samples. For the present purpose, we hence have to turn to alternative techniques, namely finite-difference (FD) simulations of beam propagation, as presented in the next section devoted to optical design, simulation and fabrication of multi-guide RBCs.

4.2 Simulation, design and fabrication

The IMD software [45] was used to simulate x-ray intensity inside a RBC structure as demonstrated earlier [30, 35, 42]. Fig. 4.1(a) shows the single layer schematic of a RBC, serving as a reference for the multi-guide RBCs structures. The low density guiding layer is sandwiched in between two high density cladding layers. The top cladding is sufficiently thin to enable coupling of the beam in reflection geometry. Here we use Ni (5 nm) /C (50 nm) /Ni (50 nm) on a GaAs substrate. Fig. 4.1(b) shows the simulated x-ray reflectivity as a function of incident angle α_i in the range from 0.1° to 0.3°, for 13.8 keV photon energy. Note that both the incoming beam size and the RBC length L are treated as infinite. The sharp dips in the x-ray reflectivity between the critical angles α_c^C of C and α_c^{Ni} of Ni evidence the excitation of the TE_0 , TE_1 , TE_2 and TE_3 modes inside the cavities. The corresponding calculated electric field intensity distribution as a function of α_i and the depth in x direction can be conveniently illustrated in the form of two-dimensional contour plots, as represented in Fig. 4.1(c). The characteristic antinodes of the x-ray standing waves corresponding to electric modes (TE_m, $m = 0, ..., 3$) of RBC structure can be easily located. Fig. 4.1(d, e, f) shows the equivalent plots for the multi-guide RBCs with three guiding layers [Ni (5 nm)/C (50 nm)]$_3$ /Ni (50 nm) on GaAs substrate. The coupling of the modes results in a splitting and lifting of degeneracy, as first discussed in [30].

The simulations shown above have been calculated for an infinite beam. Such simulations can only be expected to describe experiments well, if the beam footprint on the surface s is much larger than the beam offsets o arising from the Goos-Hänchen effect, associated with the multiple reflections and cou-
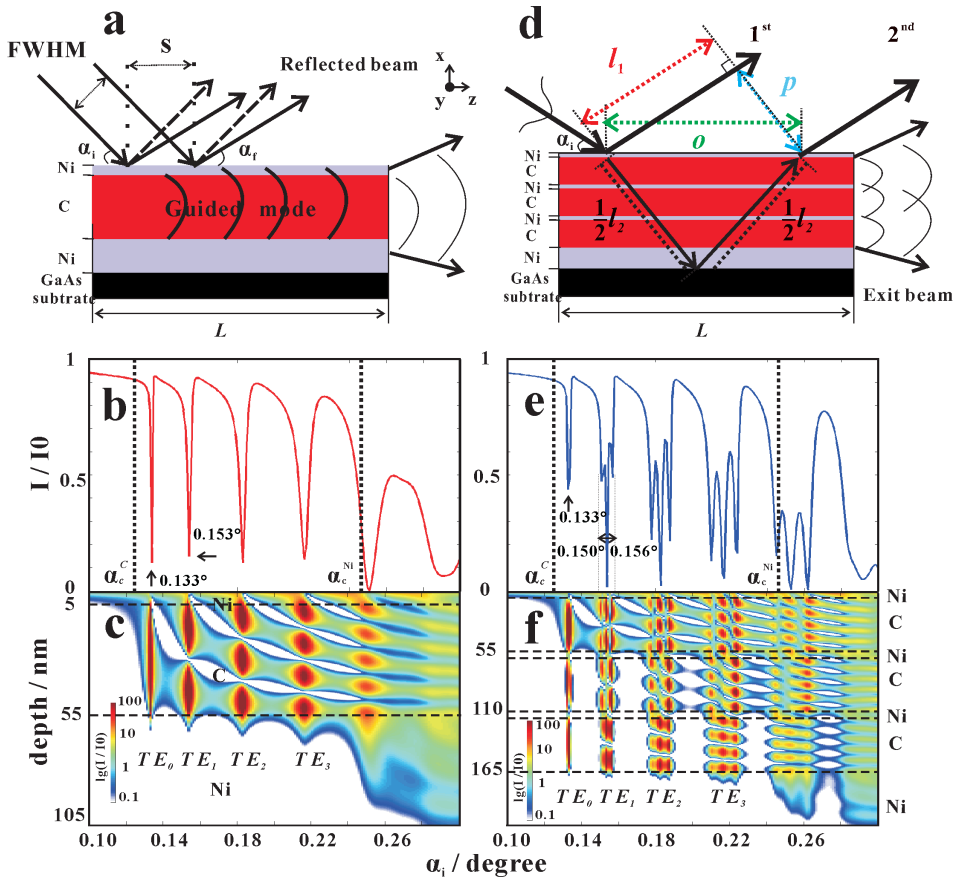
Figure 4.1: *(a) A simple sketch of a RBC, consisting of one C layer (red) and two Ni layers (purple), deposited on the GaAs substrate. (b) Reflectivity as a function of α_i for 13.8 keV photon energy. The critical angles of C (α_c^C) and Ni (α_c^{Ni}) are shown as black dotted lines. (c) Calculated field intensity in the RBC in logarithmic scaling. The modes TE_m observed at different α_i are labeled. (d-f) The corresponding plots for a multi-guide RBCs structure with three C guiding layers and four Ni cladding layers. In the schematic (d) the incoming beam with a beam size $FWHM$ is coupled into the multi-guide RBCs structure, illuminating the surface over a size $s = FWHM/sin(\alpha_i)$. If $FWHM$ and s are sufficiently small, the RBCs structure can exhibit several reflected beams, which is the central phenomena studied in this work. Important parameters characterizing the 1st and 2nd reflected beams are the path length of 1st reflected beam l_1 (red dash line), the path length of 2nd reflected beam l_2 (black dash line), the beam offsets on the surface o (green dash lines), and the distance between two beams p (blue dash lines). Note that the simulation shown in (e,f) assume an infinite beam and structure.*

pling into modes, as schematically illustrated in Fig. 4.1(d). If the illuminated spot size on the surface s and o become of comparable size, we must expect
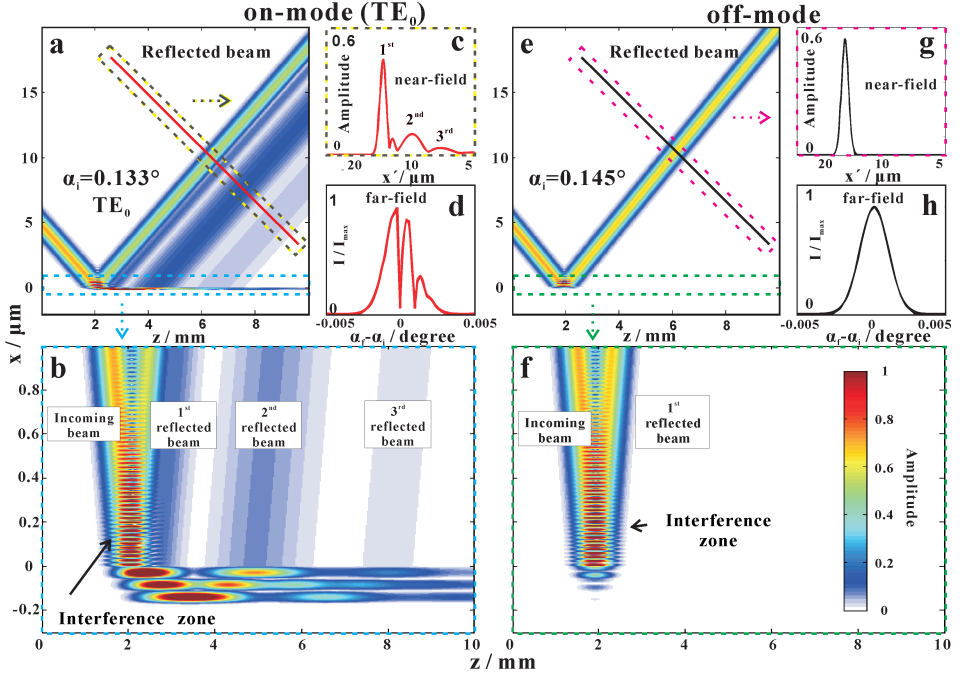
Figure 4.2: *Simulation of mode excitation with finite (sub-μm) beams. The near-field distributions for (a, b, c, d)* on-mode *conditions at $\alpha_i = 0.133°$, and (e, g, h, f)* off-mode *conditions at $\alpha_i = 0.145°$, simulated for the theoretical RBCs parameters tabulated in Tab. 4.1, and (the experimental) photon energy 13.8 keV. For the incoming beam a Gaussian profile with beam size $FWHM = 600$ nm was assumed. (c, g) The 1D profiles in the near-field, and (d, h) the corresponding normalized far-field patterns.*

deviations. In particular, we anticipate the formation of several reflected beams which are well separated in positions. With respect to the schematically sketched geometry, the path length difference Δ between 1st and 2nd reflected beams is given by $\Delta = l_2 - l_1$, with $l_2 = 2((o/2)^2 + d_{RBC}^2)^{1/2}$ and $l_1 = p/tan(\alpha_i)$, where d_{RBC} denotes the total thickness of the multi-guide RBCs, and p the distance between the two parallel reflected beams. Of course, this geometric optical argument is overly simplistic, but it should certainly give the correct order of magnitude, in particular to estimate the time delay $\Delta t = \Delta/c$ between the two beams, which is on the order of several attoseconds given the grazing incidence angles of mode excitation (a few mrad) and a typical total film thickness of the RBCs (several 100 nm).

In order to observe such phenomena, we must collimate or focus the beam down to $FWHM$ values which are on the order of the characteristic RBCs

sizes along the vertical direction (x). Let's consider typical values for the experimental design: at the angle of the TE_0 mode $\alpha_i = 0.133°$, a beam size of $FWHM = 600$ nm would result in $s \simeq 260\ \mu$m, which is smaller than the beam offset o, estimated based on d_{RBC} and the fact that multiple-reflections and coupling in and out of modes will results in a more significant beam offset o. In order to make these speculations precise, we need to simulate the propagation, coupling and reflection of finite beams in the RBCs structure. To this end, we use FD calculations of the parabolic (paraxial) wave equation [20].

Fig. 4.2 presents the results of FD simulations, carried out for the multi-guide RBCs sketched in Fig. 4.1(d), with the theoretical design parameters tabulated in Tab. 4.1, for (the experimental) photon energy 13.8 keV, and incoming Gaussian beam with beam size $FWHM = 600$ nm. The near-field distributions are shown for two cases: (a-d) *on-mode* and (e-h) *off-mode*, where *on-mode* refers to the excitation of the TE_0 mode at $\alpha_i = 0.133°$, and *off-mode* refers to $\alpha_i = 0.145°$. The total length of the RBCs (and the FD simulation) along z is $L = 10$ mm. Under *on-mode* conditions, three reflected beams are observed, exiting the RBCs surface at different offsets along z. An interference zone [55] is also formed between the primary incoming beam and the 1st reflected beam as shown in Fig. 4.2(b). The guided modes are resonantly excited in the different channels at different positions along z. When the guided modes form in the top channel, the 2nd or 3rd reflected beam comes out from the surface. Fig. 4.2(c) shows a cross-section through the reflected beam in the near-field (red line, orthogonal to the reflected beam). Fig. 4.2(d) shows the corresponding normalized far-field pattern (intensity profiles). For comparison, the *off-mode* case for $\alpha_i = 0.145°$ is shown in Fig. 4.2(e) and (f). From these simulations, we can conclude that the experimentally observable fingerprint of the multiple reflections is the characteristic lineshape of the reflected beam in the far-field, in particular the cusps visible in (d). Note that these cusps should be observed for constant α_i as a function of the coordinate on the detector, or in a so-called detector-scan along 2θ when using a point detector.

Fig. 4.3 presents analogous results for the TE_2 mode with (a) $FWHM$: 600 nm at $\alpha_i = 0.187°$ and (b) $FWHM$: 300 nm at $\alpha_i = 0.185°$, respectively, illustrating the importance of a sufficiently focused incoming beam to clearly separate the reflected beams. Note that in this case, the maximum values of the two reflected beams (1st and 2nd) are almost equal, which makes this configuration attractive for beam-splitter and delay applications.

To sum up, FD simulations show that multi-guide RBCs structures can result in multiple reflected beams, linked to mode excitation with finite-size (sub-μm) beams. The phenomenon occurs only at the proper α_i values required for mode
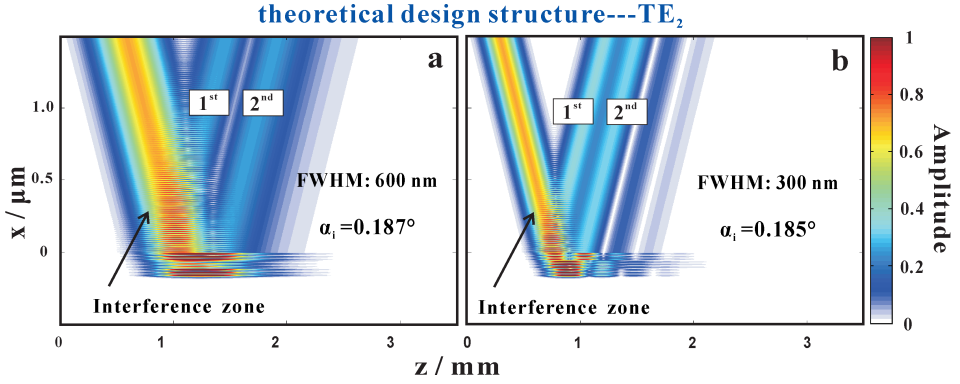
Figure 4.3: *Under excitation of the TE_2 mode, simulated for the theoretical design parameters, the two reflected beams (1st and 2nd) are almost equal amplitude. This is true for a range of beam sizes, here demonstrated for (a) $FWHM = 600$ nm, and (b) $FWHM = 300$ nm. Note the small offset in α_i appears when changing the beam size.*

excitation. Since the near-field distribution is often not accessible experimentally, it is important to evidence this effect by far-field measurements, which is possible due to the characteristic lineshape associated with the multi-exit beam behavior. Next, we turn to the fabrication of the structures designed according to the FD simulation results.

For the purpose of fabricating the multi-guide RBCs sample, we have used direct-current magnetron sputtering system [66, 71] at the Institute of Precision Optical Engineering at Tongji University, China. The fabricated RBCs consists of three amorphous C layers, and four polycrystalline Ni layers, following the theoretical design parameters as shown in Tab. 4.1. The in total 7 layers were deposited on $GaAs$ substrates alternately, under the base pressure 3.0×10^{-4} Pa. The sputter gas was Ar with purity of 99.999%, and the gas pressure was kept constant at $1.50 \pm .02$ mTorr (0.1995 Pa). After the fabrication, the x-ray macroscopic reflectivity (XMR) was obtained with macroscopic beam size, using an in-house $Cu \, K_\alpha$ source ($\lambda = 0.154$ nm), equipped with a reflectometer. The 1D XMR curve (as shown in Fig. 4.8 in app. 4.4) was fitted by using the Genetic Binda algorithm of IMD [45] with individual layer thickness values of the Ni and C layers, as shown in Tab. 4.1. Afterwards, the 2D far-field pattern of RBCs sample was carried out at the GINIX (Goettingen Instrument for Nano-Imaging with X-rays) experiment setup, installed at the P10 beamline at the PETRA III synchrotron facility in Hamburg (DESY) [12]. Using the energy of 13.8 keV, the far-field patterns were recorded by a Eiger 4 M pixel detector (Dectris).

Table 4.1: *The theoretical designed parameters and XMR fitting structure are compared.*

Layer name	Ni	C	Ni	C	Ni	C	Ni	GaAs sub
Theoretical design results								
Layer thickness / nm	5.0	50.0	5.0	50.0	5.0	50.0	50.0	
XMR fitting structure								
Layer thickness / nm	5.3	47.2	5.3	47.2	5.3	47.2	50.1	

4.3 Results

Fig. 4.4 presents the schematic of the experimental setup of GINIX at beam-line P10, and illustrates the data reduction. The synchrotron is focused onto the RBCs structure by a Kirkpatrick-Baez (KB) mirror system. The illuminating beam size at the focal distance f is determined by the gap of the horizontal slit hg (in x direction). With entrance slit larger than the KB acceptance $hg \geq 0.4$ mm, the beam size at the sample plane SP is around 295 nm in x direction. Decreasing hg from 0.4 mm to 0.05 mm, the measurements have been carried out after careful alignment (at $hg = 0.05$ mm), with (successively) larger spot sizes ($FWHM$), broadened by diffraction. The transmitted primary beam and the desired reflected beam were recorded in the far-field by the Eiger 4 M pixel detector (Dectris), as exemplified in Fig. 4.4(b), with pixel size 75 μm, placed at $D = 5.4$ m behind the focal plane. In Fig. 4.4(c), a close-up of the 2D line-shape of the reflected beam is shown under *off-mode* condition at $\alpha_i = 0.170°$, while (d) shows the *on-mode* lineshape for the TE_2 mode at $\alpha_i = 0.187°$. The 2D far-field patterns are integrated in y direction to yield the corresponding 1D profiles, see the Fig. 4.4(e) and (f), respectively. In both 1D and 2D representations, the far-field pattern of the *on-mode* case differs from the reflected beams signal of the *off-mode* case. Namely, it shows characteristic cusps (minima). Note that due to mirror imperfections, also the *off-mode* reflected beam exhibits vertical stripes, but under *on-mode* additional and more pronounced minima are observed. Fig. 4.4(g) presents the intensity distribution, as a function of α_i and detector coordinate x, after integration of the intensity along y. In this plot the angular increment is $\Delta\alpha_i = 0.001°$, while the pixel size (x direction) is 75 μm. Typically, α_i was scanned in the range from -0.1° to 0.5°. Except for $\alpha_i \simeq 0$, where the incoming beam can pass above the RBCs surface, the RBCs with its GaAs substrate significantly attenuates the primary beam.

Next, we compare the experimental pattern to the FD simulations. To this end, we start from the integrated intensity patterns as shown in Fig. 4.4(g), but now transform the detector coordinate along x to $\alpha_f - \alpha_i$. In this way the reflected
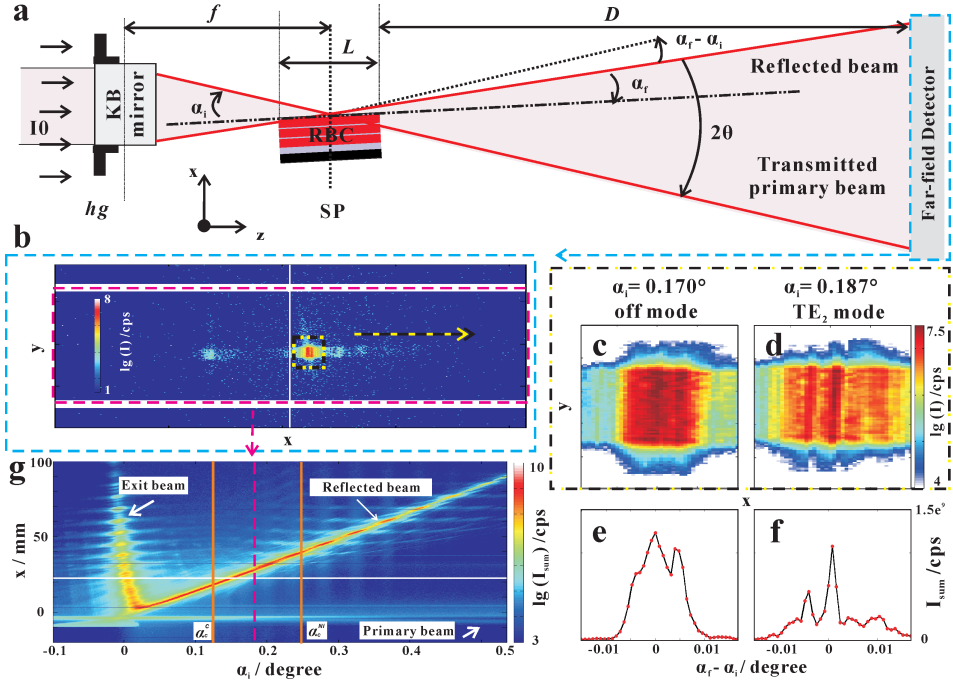
Figure 4.4: *(a) Schematic of the GINIX experimental setup. The RBCs is positioned in the focal plane at distance f behind the Kirkpatrick-Baez (KB) mirror system. The reflection plane is horizontal. By closing the slits in front of the KB mirror, the focus is made fully coherent (in the relevant horizontal plane). The diffraction limited spot size is then adjusted by the gap of the horizontal slits* hg. *The far-field intensity patterns at 13.8 keV photon energy (selected by the Si(111) monochromator) is then recorded as a function of exit angle* α_f *for each finely tuned incidence angle* α_i, *using a Eiger 4M pixel detector (Dectris) at distance* $D = 5.4$ *m. The lineshape of the reflected beam is then analyzed as a function of* $\alpha_f - \alpha_i$. *(b) An exemplary two-dimensional (2D) far-field pattern with primary and reflected beams for* $\alpha_i = 0.187°$ *and* $hg = 0.05$ *mm. (c, d) Zoom of the reflected beam, for (c)* $\alpha_i = 0.170°$, *and (d)* $\alpha_i = 0.187°$, *corresponding to* **off-mode** *and* **on-mode** *(TE_2) conditions, respectively. (e, f) The corresponding integrated 1D far-field curves, obtained after integration along* y. *(g) The intensity distribution as a function of* α_i *and* x, *integrated over* y. *The integration domain is indicated by the red dash rectangles in (b). The relevant region* $\alpha_c^C \leq \alpha_i \leq \alpha_c^{Ni}$ *containing the characteristic reflectivity cusps of the* TE_m *mode is marked by orange lines.*

intensity as function of α_i corresponds to a horizontal stripe, with a width given by the divergence of the reflected beam.

Fig. 4.5(a) shows the experimental result, for the relevant range including in particular the region $\alpha_c^C \leq \alpha_i \leq \alpha_c^{Ni}$, where four different modes are observed. The angular resolution in $\alpha_f - \alpha_i$ is about resolution $8 \times 10^{-4°}$. The blank gaps due to the inter-module gaps of the detector (see Fig. 4.4(g)) had been filled
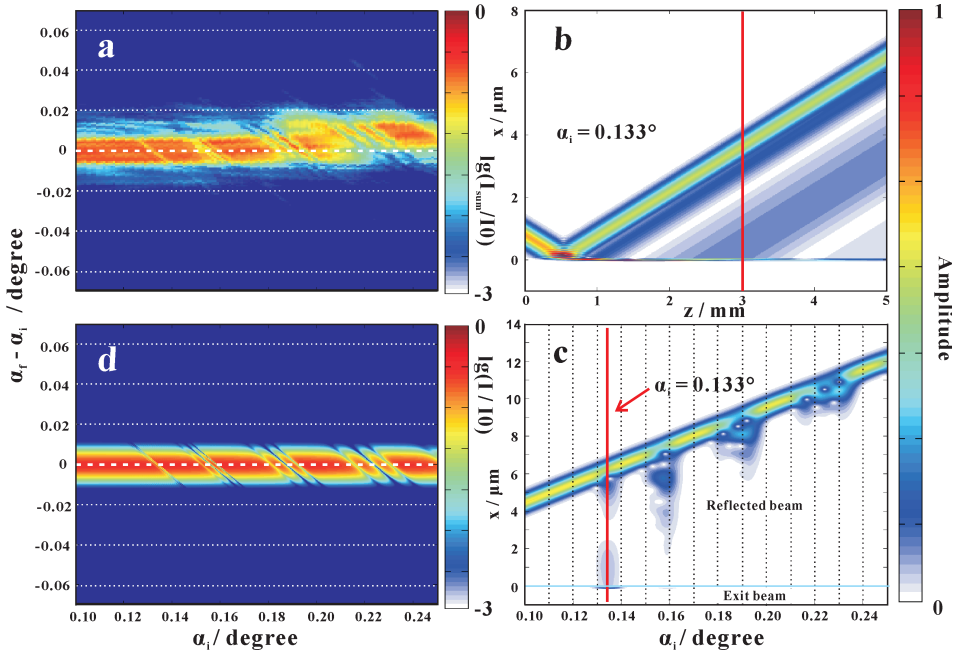
Figure 4.5: *Comparison of experimental and simulation results. (a) Experimental results: Close-up of the experimental lineshape in the relevant α_i range, for the data shown in Fig. 4.4(g), after transformation $x \rightarrow \alpha_f - \alpha_i$. (b) FD near-field distribution (amplitude) of the RBCs structure with tabulated XMR fitting parameters, for $\alpha_i = 0.133°$. (c) Simulated near-field amplitude in the plane indicated by the red line in (b) for all α_i in the relevant range. (d) Simulation results, corresponding to (a), obtained by transforming the FD data shown in (b, c) to the far-field pattern.*

with values from neighboring pixels. In order to obtain data of similar structure, we treat the FD results in an analogous manner. First the reflected beam is simulated by near-field propagation, as shown in Fig. 4.5(b) for the case $FWHM$=600 nm and $\alpha_i = 0.133°$. The geometric parameters of the multi-guide RBCs structure were taken from the XMR fitting structure in Tab. 4.1. For the simulation, the pixel sizes in x and z directions were 1 nm and 0.1 μm, respectively. The amplitude and phase of the reflected beam were then collected at a certain reference plane at about 2.5 mm behind the focus or center of the RBCs structure, indicated by the red line at $z = 3$ mm in Fig. 4.5(b). Fig. 4.5(c) exhibits the amplitude distribution along x at $z = 3$ mm, for all α_i. In this plot, the angular resolution is $\Delta\alpha_i = 10^{-4}°$. From this simulated amplitude data as shown in Fig. 4.5(c) and the corresponding phase (not shown), we then compute the far-field intensity distribution by performing a discrete Fourier trans-

form (FFT algorithm). Note that in order to perform the FFT, we first have to transform the data along the vertical red line in Fig. 4.5(b) to a plane orthogonal to the reflected beam. This is accomplished by a multiplicative phase $factor = \exp(ikx\sin(\alpha_i))$, resulting in a properly tilted coordinate x' for the output field. Fig. 4.5(d) presents the results, i.e. the simulated far-field intensity, again as a function of α_i and $\alpha_f - \alpha_i$, so that it can be directly compared to the experimental result of Fig. 4.5(a). The angular resolution in $\alpha_f - \alpha_i$ is $3.03 \times 10^{-4\circ}$. Direct observation illustrates that the characteristic stripe patterns observed in the simulated and experimental far-field intensities (Fig. 4.5(a) and (d)) are nearly identical. Note that the observed far-field stripe patterns can be directly attributed to the multiple reflections in the near-field for the different *on-mode* angles α_i. In other words, they indicate the presence of several reflected beams by interference.
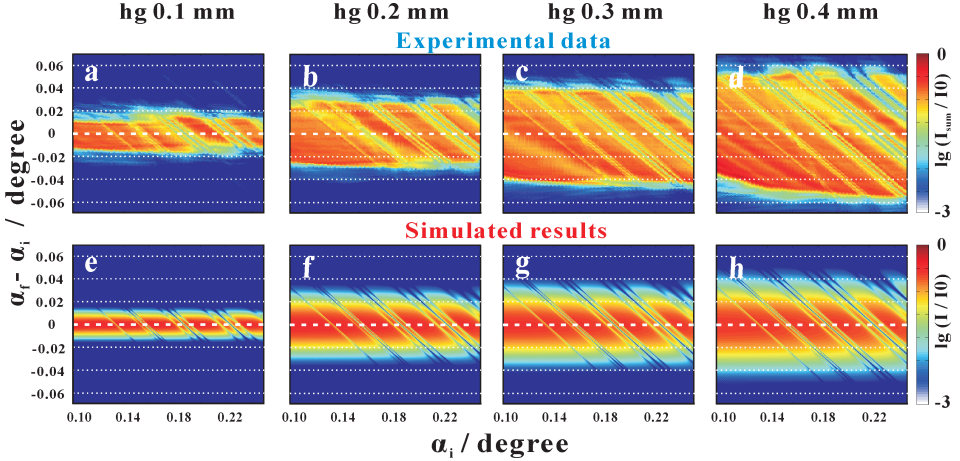
Figure 4.6: *The extended comparison of the measured far-field patterns and the simulated far-field patterns, presented for different beam sizes, as controlled by the entrance slits. The results are presented for (a, e)* $hg = 0.1$ *mm, (b, f)* $hg = 0.2$ mm, *(c, g)* $hg = 0.3$ *mm, and (d, h)* $hg = 0.4$ *mm, respectively.*

Fig. 4.6 shows an extended comparison of the measured far-field patterns and the simulated far-field patterns, presented for different beam sizes, as controlled by the entrance slits. Namely, results are shown of (a, e) $hg = 0.1$ mm, (b, f) $hg = 0.2$ mm, (c, g) $hg = 0.3$ mm, and (d, h) $hg = 0.4$ mm, respectively. For all slits and beam sizes, the experimental results and the simulations are in good agreement. Note that the beam size is an important control parameter, since the multiple reflected beam can only be observed for finite (typically sub-μm) beam sizes. From the FD simulations, the beam sizes $FWHM$ are 600 nm

for the case $hg = 0.05$ mm, 300 nm for the case $hg = 0.1$ mm, 130 nm for the case $hg = 0.2$ mm, 110 nm for the case $hg = 0.3$ mm and 90 nm for the case $hg = 0.4$ mm, respectively. Note that the relationship between beam size and hg is further elucidated in app. 4.4.

4.4 Discussion and Conclusion

The comparison between the simulated and experimental reflectivity clearly shows that the multi-guide RBCs structure can result in two spatially offset reflected beams, when modes are excited (*on-mode* condition). This requires finite-size illumination (sub-μm) beams. In the far-field the beams interfere due to their divergence, but in the near-field the beams are well separated.

To accentuate these results, the near-field intensity distribution is shown in Fig. 4.7 for the *on-mode* condition, both for Fig. 4.7(a) the theoretical design parameters, and Fig. 4.7(d) the XMR fitting parameters as tabulated in Tab. 4.1. In both cases the desired beam-splitting is observed, see Fig. 4.7(b, e) the close-ups of the near-field profile, and Fig. 4.7(c, f) the corresponding far-field profiles, with the experimental data shown alongside in Fig. 4.7(f). The experimental 1D profile (black) and the simulated far-field curve (red), shown for the TE_2 mode at $hg = 0.1$ mm (corresponding to Fig. 4.6(a)), exhibit a similar lineshape with the identical cusps positions. Note that the deviations in the *off-mode* regions of the far field patterns can be attributed to the fact that the FD simulations assume an idealized Gaussian beam, while the experimental focal lineshape is quite different. Importantly, simulation and experiment give consistent results and both show that the two reflected beams are of nearly equal amplitude, as desired. Note that the influences of $FWHM$ and the mode number on the respective amplitudes of the two beams are further illustrated in app. 4.4.

In summary, the multi-guide RBCs with three guiding layers in the $[Ni/C]_3/Ni$ structure, as can be fabricated by state-of-the-art thin film sputter deposition, can exhibit interesting new phenomena when illuminated with finite-size (sub-μm) beams, which are completely obscured when simulating and measuring with standard macroscopic beams. In particular, multiple reflected beams can be observed exiting the structure at well controlled spatial offset. This effect could be exploited in interferometric applications or for off-axis holographic x-ray imaging. One could, for example, place an object onto the surface at a position illuminated only by the second beam. The associated phase shifts could then be probed by far-field interference with the first (reference) beam. While the present work is entirely focused on continuous-wave (cw) illumina-
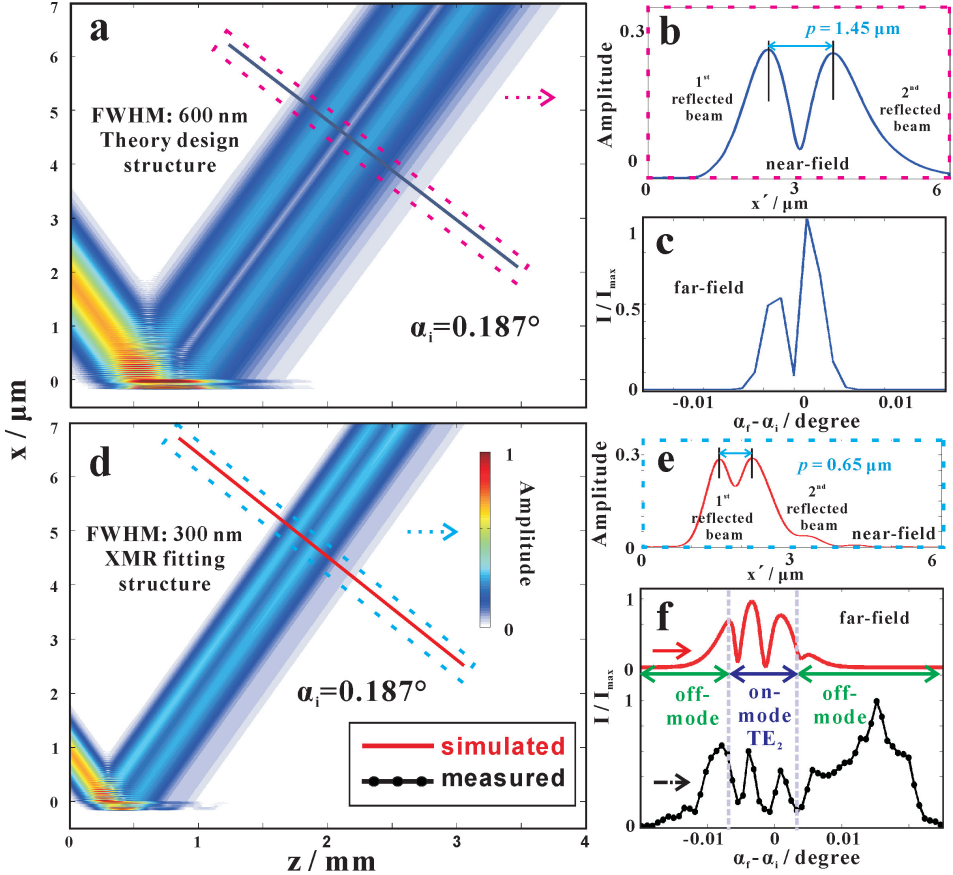
Figure 4.7: *(a) The near-field distributions for the multi-guide RBCs structure at $\alpha_i = 0.187°$, as computed by FD simulation for the theoretical RBCs parameters tabulated in Tab. 4.1, and for the experimental photon energy 13.8 keV, and beam size $FWHM = 600$ nm. (b) The 1D near-field profile, with (c) the corresponding far-field profile calculated by a FFT. (d, e) Analogous simulations for the RBCs parameters as refined by XMR fitting structure, for $\alpha_i = 0.187°$ and $FWHM=300$ nm. (f) Comparison between the simulated (red) and experimental (black) far-field profiles. The cusps along the detector coordinate α_f are 'fingerprints' for the presence of two reflected beams. By comparison, we can further infer that both reflected beams in the experiment are of similar amplitude, around $\simeq 0.29$.*

tion (both simulation and experiment), one could also explore the effect of such RBCs on ultra-short and focused x-ray pulses, as generated by free-electron laser (FEL) or higher harmonic (HHG) radiation. In particular, such designed multi-guide resonant beam couplers could serve as time-delay beam splitters with attosecond delay, orders of magnitude smaller than current macroscopic

pulse delay stages [90, 91]. Multi-guide RBCs in combination with sub-μm beams may further be useful to probe surface and near-surface structure and dynamics. Finally, they offer novel opportunities for x-ray quantum optical experiments, extending the seminal work in this field performed with single guiding layers [92].

Appendix

X-ray macroscopic reflectivity (XMR)
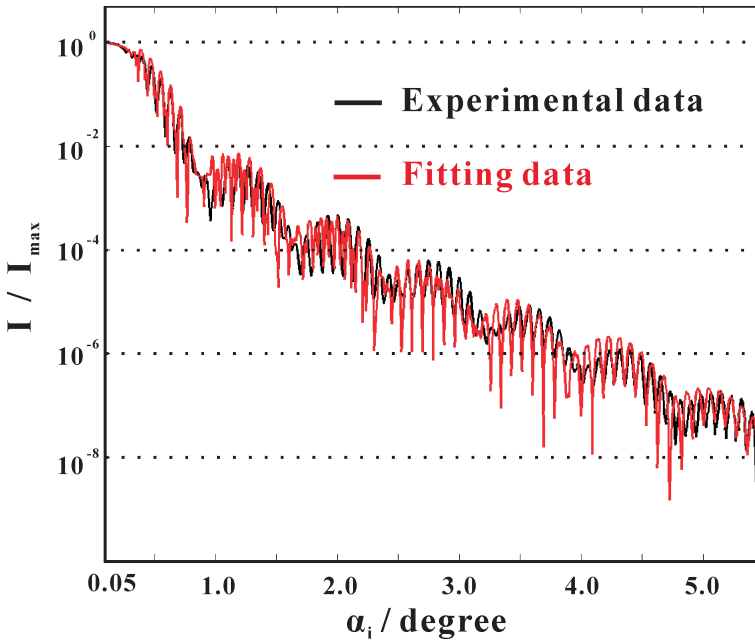
Figure 4.8: *Measured reflectivity (black line) and fitting curve (red line) as a function of incident angle α_i for the RBCs sample.*

XMR was performed for the multi-guide RBCs, using an in-house Cu K_α source ($\lambda = 0.154$ nm), equipped with collimating multilayer mirrors and a fully motorized reflectometer [73]. The x-ray reflectivity was recorded with 0.1 mm beam as defined by the entrance slits. An angular range of 0° to 8° was scanned. Fig. 4.8 shows the reflectivity as a function of α_i in black line, after subtracting the diffuse (nonspecular) background as measured by an off-set scan (off-set angle

of 0.1°), and after performing the illumination correction. The XMR curve was fitted (red line) in the region of 0.05° to 5.5° using the Genetic Binda algorithm of IMD with individual layer thickness values of the Ni/C layers as free parameters. The fitting results are tabulated in Tab. 4.1.

The relationship between hg and beam size
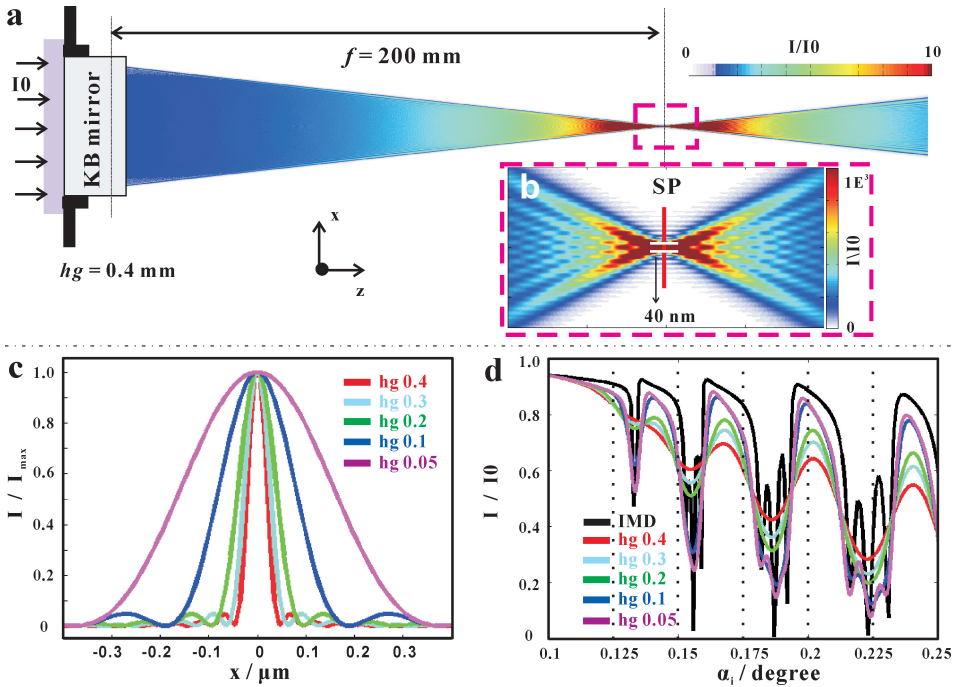
Figure 4.9: *(a) Schematic of the experimental setup, and field distribution calculated by free space propagation between the KB mirror and focal plane. The incoming beam, with primary intensity I_0 and photon energy 13.8 keV is coupled into the RBCs, which is positioned at $f = 200$ mm in the focal plane of KB mirror system. (b) Close-up of the focal intensity for hg = 0.4 mm, resulting in $FWHM = 40$ nm . (c) Simulated beam profiles (normalized) in the focal plane (hg = 0.4 mm in red line, hg = 0.3 mm in light blue line, hg = 0.2 mm in green line, hg = 0.1 mm in dark blue line, hg = 0.05 mm in purple line). (d) The corresponding 1D profiles from Fig. 4.5(a) and Fig. 4.6 are compared to the reflectivity calculated for infinite beams by IMD (black line), plotted for an angular range of α_i from 0.1 to 0.25 degrees.*

Fig. 4.9(a, b) present field simulations by free propagation from the KB mirror to the focal (sample) plane *SP*, combined with the schematic of the experimental setup. The focal plane is at position $f = 200$ mm. For $hg = 0.4$ mm, the spot size

in the focal plane is $FWHM = 40$ nm. With the variation of hg in the simulation, the calculated $FWHM$ are 330 nm for $hg = 0.05$ mm, 170 nm for $hg = 0.1$ mm, 90 nm for $hg = 0.2$ mm, 60 nm for $hg = 0.3$ mm and 40 nm for $hg = 0.4$ mm, respectively, as determined from the curves shown in Fig. 4.9(c). These results deviate from those obtained by matching the lineshape of the FD simulations to the experimental data (where beam size was a free parameter), see values tabulated in Tab. 4.2. This can be attributed to a number of reasons: Firstly, finite source size is not included. Secondly, the slit size hg is a nominal value likely to have an offset with respect to the true gap. Finally, the sample may have been positioned slightly out of the focal plane in some scans. Nevertheless, the general trend of increasing $FWHM$ with decreasing hg is preserved.

Fig. 4.9(d) shows a comparison of the plateau of the total reflection, between

Table 4.2: *Comparison of beam size $FWHM$, between the free propagation simulated results and FD simulated data.*

Conditions	**hg 0.4 mm**	**hg 0.3 mm**	**hg 0.2 mm**	**hg 0.1 mm**	**hg 0.05 mm**
The free propagation simulated results					
$FWHM$/ **nm**	40	60	90	170	330
The FD simulated results					
$FWHM$/ **nm**	90	110	130	300	600

the simulations for infinite beam (IMD simulation, black) and the different finite beam sizes, as varied by hg as the control parameter in FD simulations. The dips (cusps) become much sharper with decreasing hg, i.e. increasing $FWHM$. Compared to the IMD reflectivity, all dips of the simulated results ($hg = 0.4$ mm in red line, $hg = 0.3$ mm in light blue line, $hg = 0.2$ mm in green line, $hg = 0.1$ mm in dark blue line, $hg = 0.05$ mm in purple line) keep the antinodes corresponding to the *on-mode* case at the same positions, but the intensity differences between *on-mode* and *off-mode* decreases.

Further discussion for the reflected beams

Fig. 4.10 presents the evolution of the near-field and far-field profiles of the multi-guide RBCs, when the beam size is increased from $FWHM = 130$ nm to $FWHM = 1800$ nm, based on the analogous calculations as shown in Fig. 4.7. Fig. 4.10(c, e, g) show that the maximum values of the two reflected beams (1st and 2nd reflected beams), remain roughly equal over the entire range, resulting in the characteristic lineshape of the reflected beam, see Fig. 4.10(d, f, h). This

phenomenon can be tailored by tuning the parameters of $FWHM$, incident angle α_i and the structure of RBCs.
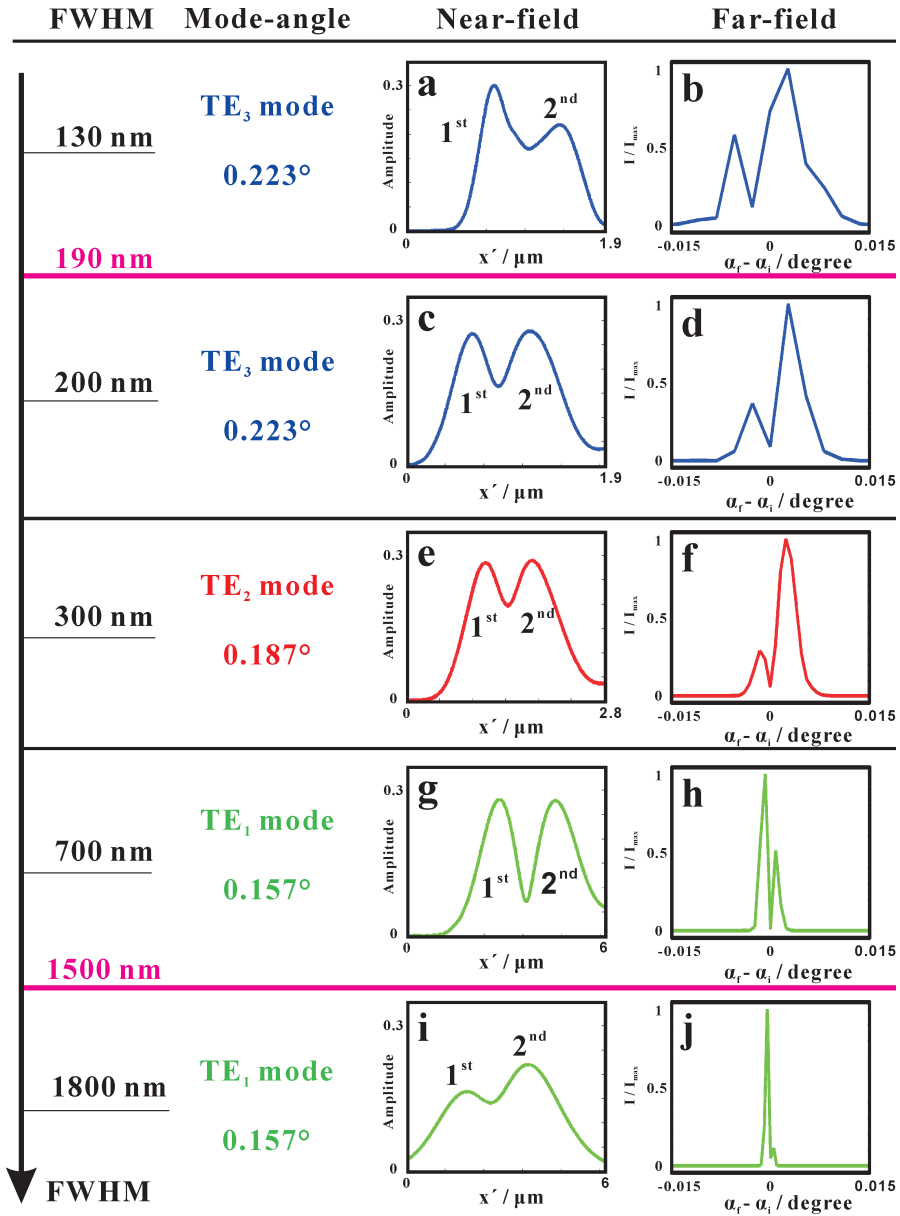

Figure 4.10: *Using similar simulations as shown in Fig. 4.7, (a, c, e, g, i) near-field and (b, d, f, h, j) far-field profiles, calculated for increasing FWHM, from 130 nm to 1800 nm.*

Acknowledgments

5 Conclusion and outlook

The aim of this thesis was to design novel waveguide structures, and to analyze them in view of complex phenomena of near-field propagation. For this purpose, experimental far-field measurements were used in combination with FD simulations and phase retrieval methods. Two novel structures have been designed, fabricated and characterized: the WGA, yielding several waveguided beams in transmission, and multi-guide RBCs, tailored to yield two or several reflected beams. The WGA and the multi-guide RBCs are not only distinct in the coupling geometry. A major difference is related to the fact that the WGA principle is based on the separation (non coupling) of the different transmitted wavelets, while the RBC functions are based on a strong coupling of guided radiation in several layers.

For the WGA structure: In Chapter 2, the basic concept of the x-ray waveguide array (WGA) was first proposed. The WGA is a novel geometry combining the multilayers and front couplers concept in the x-ray wavelength, aimed at creating a particular interference pattern and designed near-field distributions behind the waveguide exit. With controlled exit phases by variation of d, The WGA can serve several purposes: Firstly, it enables similar optical functions and applications as conventional x-ray waveguides used at synchrotron sources, in particular coherence and spatial filtering in the incoming beam. Compared to the conventional waveguides with a single guiding layer, the WGA has a larger effective entrance cross section, and can thereby help to increase the coupling efficiency. Secondly, with an optimized material combination, the WGA can reduce the absorption inside the cladding. Third and most importantly, the phase relations between the different guided beams can be tailored to produce special near-fields behind the WGA's exit by multi-waveguide interference. Near-field interference behind the exit plane is then achieved by carefully designing the multilayer geometry, in particular by choosing different cross sections d_i for each channel i. This allows to tailor intensity distributions with special properties, e.g. creating a secondary quasi-focal spot in free-space. We demonstrate this concept by a specific x-ray Mo/C WGA consisting of seven planar waveguides, fabricated by high precision direct-current magnetron sputtering of amorphous carbon and molybdenum. With the precise analysis of the layer thickness combination, the FD simulations present a free-standing quasi-focal spot behind the WGA with a spot size of 23.8 nm ($FWHM$).

For the WGA structure: In Chapter 3, contrary to the analysis method in the previous chapter, we present a much more direct visualization of the near-field interference pattern. The WGA is verified experimentally by reconstructing the near-field from the measured far-field diffraction pattern, based on iterative phase retrieval algorithms (ER and HIO). Some steps forward with respect to the previous work. Firstly, to further illustrate the specific field modulating effects which can be achieved by a symmetrical variation of the waveguide width d_i for each waveguide i, we have investigated the near-field of two different kinds of waveguide structures, namely the mentioned Ni/C WGA and WGM, respectively. Secondly, the WGA is designed as an 1DWG structure. It is to be noted that the phase problem in one-dimensional geometries is generally not amenable to phase retrieval by iterative algorithms (non-uniqueness). Therefore, to enable the successful field reconstruction, we use a pre-focused beam with substantially higher spatial coherence so that the field is confined in the xy plane perpendicular to the optical axis z, and a 2D detection scheme. For this reason, we had anticipated the requirement of as much support information as possible, and have therefore used the strong *a priori* information of position of the seven waveguide channels (the beamlets). Two different supports (the tight support and the loose support) have been compared with regard to wavefront reconstruction. Owing to the smaller error and most convincing pattern, the results from loose support using the ER algorithm are somewhat robust, and can be compared with the FD calculations of the designed WGA parameters in the near-field. In particular, a quasi-focal spot size in the sub-50 nm range can be achieved. It must be noted, however, that a WGA with a small number of layers has a very limited capability to optimize this quasi-focal spot. In particular, it seems not possible to reduced the substantial amount of further maxima and minima in the near-field.

For the multi-guide RBCs structure: In Chapter 4, the multi-guide RBCs with three guiding layers in the $[Ni/C]_3/Ni$ structure can exhibit novel phenomena when illuminated with finite-size (sub-μm) beams, which are completely occurred when simulating and measuring with standard macroscopic beams. Since part of the incident beam is directly reflected without coupling, one can then face a peculiar situation with two (or even more) reflected beams of almost equal amplitudes. The lateral shift of the different reflected beams can be regarded as a special manifestation of the Goos-Hänchen effect. One could even call this a giant Goos-Hänchen effect. Both optical simulations and the experimental proof-of-concept results show that multi-guide RBCs structures can result in multiple reflected beams, linked to the specially designed structures, and resonant mode excitation with finite-size (sub-μm) beams. It is to

be noted worthy that the maximum values of the two reflected beams can also reach the same value.

Outlook

Further generalisations of WGA scheme could include several extensions and applications:

1. Simulations show that special effects like a double focus or tilted emission of the beam can be achieved by such WGA structures, Mo/C WGA and Ni/C WGA. A near-field design with a doubled quasi-focal spot, for example, could be used for differential phase contrast imaging. Tilted emission, on the other hand, could be used to increase the effective numerical aperture for holographic recordings.

2. This concept can be directed at two-dimensional control of the near-field distribution by crossing to thin WGA foils, similar to the 2DWGs described in [27, 28].

3. Such tailored near-field distributions exhibiting large structural diversity can be used for coherent imaging, not only for imaging applications, but also as a more powerful probe reconstruction for inspection of the WGA near-field; by ptychography, for example, which has been shown to benefit from highly structured illumination wave field. Further, the very structured and diverse near-field distributions could be very beneficial for ptychographic phase retrieval.

Further generalisations of multi-guide RBCs scheme could include several extensions and applications:

1. The multiple reflected beams can be observed exiting the structure at well controlled spatial offset. This effect could be exploited in interferometric applications or for off-axis holographic x-ray imaging. One could, for example, place an object onto the surface at a position illuminated only by the second beam. The associated phase shifts could then be probed by far-field interference with the first (reference) beam.

2. The present work is entirely focused on continuous-wave (cw) illumination (both simulation and experiment), one could also explore the effect of such RBCs on ultra-short and focused x-ray pulses, as generated by free-electron laser (FEL) or higher harmonic (HHG) radiation. In particular, such designed

multi-guide resonant beam couplers could serve as time-delay beam splitters with attosecond delay, orders of magnitude smaller than current macroscopic pulse delay stages [90, 91]. Multi-guide RBCs in combination with sub-μm beams, may further be useful to probe surface and near-surface structure and dynamics.

3. The structures offer novel opportunities for x-ray quantum optical experiments, extending the seminal work in this field performed with single guiding layers [92].

4. Owing to the basic analysis of the Goos-Hänchen effect, the further analytical and numerical simulations could be very beneficial for the novel phenomena in the multi-guide RBCs structure with a higher number of guiding layers.

Appendix

A.1 The design, simulation and reconstruction in waveguide arrays

A.1.1 Basic calculations using mathematica source code

mode_equation.nb

```
1
2  % ***************Ni/C/Ni structure******************
3  %  symm. modes_in_Ni/C/Ni
4  %  n2: Ni_13.8keV 1-9.34051513E-06
5  %  n1: C_13.8keV 1-2.39850965E-06
6  %  n2: Ni_8keV 1-2.48911183E-05
7  %  n1: C_8keV 1-7.18478759E-06
8  % ::Input ::
9  (*lambda:=1.2398/8; *) %  working energy  13.8_keV_or_8_keV
10 (*d:=50;*) % thickness of guiding layer in nm
11 (* n1:=1-7.18478759*10^(-6); *)  % index of guiding layer
12 (*n2:=1-2.48911183*10^(-5);*)  % index of cladding  layer
13 (*m:=0;*) % mode  m=1,...,4
14
15 % basic calculated parameters
16 (*k0:=2\[Pi]/lambda;*)
17 (*CellPrint[TextCell[Row[{"k0=",k0}]]]*)
18 (*V:=k0 d Sqrt[ n1^2-n2^2];   *)
19 (*CellPrint[TextCell[Row[{"V=",V}]]]*)
20 (*CellPrint[TextCell[Row[{"N[V/\[Pi]]=",N[V/\[Pi]]}]]]*)
21 % intersection points in figure
22 (*Plot[{U Tan[U-m \[Pi]/2],U Cot[m \[Pi]/2-U],Sqrt[V^2/4-U^2]},*)
23 (* {U,0,V}, PlotRange -> {-V,V}]*)
24 (*Clear[Un,U]*)
25
26 % calculate the eigen function
27 (*U:= Un /. FindRoot[Un Tan[Un-m \[Pi]/2]==Sqrt[V^2/4-Un^2], {Un
       ,1.5}];*)
28 (*CellPrint[TextCell[Row[{"Xi=",U}]]]*)
29
30 % calculate the Beta
31 (*\[Beta]:=(k0^2 n1^2 -4*U^2/d^2)^0.5 ;
32 CellPrint[TextCell[Row[{"\[Beta]=",\[Beta]}]]]*)
33
34 % calculate the Kappa
35 (*\[Kappa]:=Sqrt[k0^2 n1^2 -\[Beta]^2 ];
36 CellPrint[TextCell[Row[{"\[Kappa]=",\[Kappa]}]]]*)
37
38 % calculate the Gamma
```

```
39   (*\[Gamma]:=Sqrt[\[Beta]^2-k0^2 n2^2];
40   CellPrint[TextCell[Row[{"\[Gamma]=",\[Gamma]}]]]*)
41
42   % calculate field intensity and amplitude
43   (*Ey[z_  /; z<-d/2]:=Cos[\[Kappa] d/2+m \[Pi]/2]* Exp[\[Gamma](z+d/2)
        ]*)
44   (*Ey[z_  /; -d/2<=z<d/2]:=Cos[\[Kappa] z-m \[Pi]/2] *)
45   (*Ey[z_  /; z>d/2]:=Cos[\[Kappa] d/2-m \[Pi]/2]* Exp[-\[Gamma](z-d/2)
        ]*)
46   (*Plot[{Ey[z],Ey[z]^2}, {z,-50,50},PlotRange -> {-1,1}]*)
47
48   % Ni/C/Ni_for_symmetrical_modes
49
50   (*dbdd[V_,d_,\[Beta]_,Xi_,k0_,n1_]:=(k0^2n1^2)/(d \[Beta])-V^2 /(d
        ^3*\[Beta]*(1+Xi*Sin[Xi]/Cos[Xi]^3+Tan[Xi]^2))-\[Beta]/d*)
51
52   % Ni/C/Ni_for_asymmetrical_modes
53
54   (*dbdd[V_,d_,\[Beta]_,Xi_,k0_,n1_]:=(k0^2n1^2)/(d \[Beta])-V^2 /(d
        ^3*\[Beta]*(1-Xi*Cos[Xi]/Sin[Xi]^3+Cot[Xi]^2))-\[Beta]/d*)
```

A.1.2 Free space propagation using matlab source code

toy_model.nb

```
1    % free propagation in xz plane (1+1dimn)
2    % Tim Salditt, initial version
3    % Qi Zhong revised.
4    % This program is mainly used to calculate WGA with inteference
         patterns
5    clear all; close all; clc
6    set(0,'DefaultFigureColor','white');
7    %% define exit field
8
9    Nx=3000
10   lambda=1.2398/19.9              % wavelenght [nm]
11   k0=2*pi/lambda;
12   dx=1;
13   x = linspace(-floor(Nx/2),floor(Nx/2),Nx);
14   x=x*dx
15   % different incoming beam
16   % rect = @(x) 0.5*(sign(x+0.5) - sign(x-0.5)); % rectangular beam
17   gauss= @(x) exp(-pi*x.^2)                       % gauss beam
18   width =8;  % FWHM of gauss beam
19   Nphase =7;  % different number of channels
20   % % %  set the phase profile
21   dL=1e5; % nm
22   f=2*dL; % focal length    % inf    gratings
23   phase= @(x) -k0*(x.^2)/(2*f);  % phase profile
24   psi = zeros(1,Nx);
25
26   %%  Double focal spots
```

```
27  % xpos0 = -240
28  % D1=[60 60 60 60 60 60 60 60]
29  % S=abs(xpos0)/2
30  % for ind = 1:Nphase
31  %    if ind==1
32  %      xpos(ind)=xpos0+D1(ind);
33  %      phase1(ind)= phase(xpos(ind)+S);
34  %      psi = psi+gauss((x-xpos(ind))/width)*exp(1i*phase1(ind));
35  %    elseif ind<=Nphase/2
36  %      xpos(ind)=xpos(ind-1)+D1(ind);
37  %      phase1(ind)= phase(xpos(ind)+S);
38  %      psi = psi+gauss((x-xpos(ind))/width)*exp(1i*phase1(ind));
39  %    else
40  %      xpos(ind)=xpos(ind-1)+D1(ind);
41  %      phase1(ind)= phase(xpos(ind)-S);
42  %      psi = psi+gauss((x-xpos(ind))/width)*exp(1i*phase1(ind));
43  %    end
44  % end
45
46  %%  A quasi-focal spot
47  D1=[56 73 92 92 73 56]
48  d=[8 8 8 8 8 8 8]
49  xpos0 =-(D1(1)+D1(2)+D1(3)+d(1)+d(2)+d(3)+d(4))  % one focal spot
50  % xpos0 =-(d(1))                                % off-axis focal spot
51  for ind = 1:Nphase
52    if ind==1
53        xpos(ind)=xpos0+d(ind);
54        phase1(ind)= phase(xpos(ind));
55        psi = psi+gauss((x-xpos(ind))/width)*exp(1i*phase1(ind));
56
57    else
58        xpos(ind)=d(ind)+D1(ind-1)+xpos(ind-1);
59        phase1(ind)= phase(xpos(ind));
60        psi = psi+gauss((x-xpos(ind))/width)*exp(1i*phase1(ind));
61    end
62  end
63  %% phase shape
64
65  figure(1);plot(x,abs(psi).^2);
66  xlabel('x')
67  ylabel('E0^2')
68
69
70  phase2=phase1/pi;
71  figure(2);plot(xpos,phase2/1.9,'MarkerSize',70,'Marker','.','Color'
        ,[1 0 0]);
72  set(gca,'FontSize',16);
73  xlabel('d')
74  ylabel('phase')
75  axis([-440 440 -3.14 1]);
76  % phase3(:,1)=xpos;
77  % phase3(:,2)=phase2;
78  %  name5='phase_WGM';
79  %
80  % %best_simulation_far_field_searching21    8500
81  % filename5=sprintf('%s%s/%s.mat',folder,subfolder,name5);
```

```
82  %
83  %   save(filename5,'phase3','-v7.3');
84
85  %% simulate  propagation in xz-plane
86
87  Nz = 10000;
88  Psimatrix = zeros(Nx,Nz);
89  Imatrix = zeros(Nx,Nz);
90  z = linspace(1,300000,Nz);
91  F=dx^2/lambda./z;
92
93  for ind =1:Nz
94          Psimatrix(:,ind) = prop_nf_pa_1d_F1(psi,F(ind),1);
95  end
96  Imatrix = abs(Psimatrix).^2;
97
98  figure(3);imagesc(z*1e-6,x(1000:2000)*1e-3,Imatrix(1000:2000,:));
        colorbar
99  set(gca,'FontSize',36);
100 colorbar('FontSize',24);
101 xlabel('[z mm]')
102 ylabel('[x \mu m]')
103 set(gca,'FontSize',20,'YGrid','on');
104 caxis([0.01 0.7]);
```

prop_nf_pa_1d_F1.m

```
1   % Author K. Giewekemeyer
2   % Original file from sftp://klaus@login.roentgen.physik.uni-
        goettingen.de/
3   % home/klaus/Documents/Uni/Daten/Messzeiten/0909_BESSY/
        analysis_at_home/matlab/main/tools
4   % last modified on 2014 by Qi Zhong.
5   % modified by Tim Salditt in terms of unitless variable Fresnel
        number F
6
7   % prop_nf_pa propagates a 2d-wave field within paraxial approximation
         into the
8   % optical near field. Sufficient sampling of the phase-chirp function
9   % is checked with a near-field criterion which is only valid within
        the
10  % paraxial approximation.
11  % The validity of the small-angle approximation is enforced. If it is
         not
12  % obeyed, the function returns an error.
13  % If sampling of the phase chirp function is not sufficient, the
        field is
14  % embedded into a wider field of fiew, filling new pixels, so that a
15  % continuous boundary conditions are obeyed.
16  % If the field has been enlarged prior to propagation, it is cut back
17  % to the original size after propagation. Note that this cropping
        generally
18  % destroys the conservation of the total fluence in the array.
```

```matlab
19  %
20  % Martin KrenkeL:
21  %     - Added the possibility to choose the factor f a priori to
         avoid to
22  %         big fields. If f is not passed than the calculated f is used.
23  %     - Disabled small angle approximation error and changed to a
         warning
24
25  function Im = prop_nf_pa_1d_F(im,F,f)
26
27  % dx, dy: pixel widths in horizontal and vertical direction
28  % Delta_z: propagation distance
29  % lambda: wavelength
30  % im: incident 2d wave field
31
32  [dummy, Nx] = size(im);
33  k = 2*pi;
34  % Sampling criterion for phase chirp.
35  px = abs( F/(Nx^2));
36
37  % beta = 1 ensures Nyquist sampling. Higher beta's make result better
         , but
38  % computationally more expensive.
39  beta = 1;
40
41  if f > 1
42      fprintf('Probe-FOV is enlarged by factor %3.2f for propagation.\n
             ',beta*f);
43      % enlarged array sizes
44      Nx_l = ceil(beta*f)*Nx;
45      dqx = 2*pi/(Nx_l);
46      Qx = ((1:Nx_l)-floor(Nx_l/2)-1)*dqx;
47      % paraxial propagator
48      kappaz = -1/2*ifftshift(Qx.^2)/F/k;
49      % center in new array
50      CX = floor(Nx_l/2)+1;
51      % Embedding of image into larger field.
52      im_l1 = zeros(Nx_l);
53      im_l =im_l1(1,:);
54      % Filling up new pixels with boundary values (continuous boundary
55      % conditions).
56      % bottom rows
57      im_l(1:CX-floor(Nx/2)-1)= im(1);
58      im_l(CX+ceil(Nx/2):Nx_l)= im(end);
59      % center: actual field
60      im_l(CX-floor(Nx/2):CX+ceil(Nx/2)-1) = im;
61      % propagation
62      Im_l = fftshift(ifft(fft(ifftshift(im_l)).*exp(1i*kappaz)));
63      % decrease field of view
64      Im = Im_l(CX-floor(Nx/2):CX+ceil(Nx/2)-1);
65  else
66      dqx = 2*pi/(Nx);
67      Qx = ((1:Nx)-floor(Nx/2)-1)*dqx;
68      kappaz = -1/2*ifftshift(Qx.^2)/F/k;
69      Im = fftshift(ifft(fft(ifftshift(im)).*exp(1i*kappaz)));
70  end
```

A.1.3 Finite differences simulations

Dissertation_WGA_WGM.ll

```
1   // This code is to simulate the propagation inside and outside the
2   // WGA or WGM, using finite-difference algorithm.
3   // Lars Melchior, initial version
4   // Qi Zhong revised.
5
6   load: "FDPresets.ll"
7
8   // Simulation variables
9
10  complex nInside;
11  complex nOutside;
12  complex nvaccum;
13  complex nSubstrate;
14  real Length;
15  real Prefocus
16  real MoP4
17  real CP3
18  real MoP3
19  real CP2
20  real MoP2
21  real CP1
22  real MoP1
23  real C0
24  real MoN1
25  real CN1
26  real MoN2
27  real CN2
28  real MoN3
29  real CN3
30  real MoN4
31  real dP3
32  real dP2
33  real dP1
34  real dN1
35  real dN2
36  real dN3
37
38  real Exit
39
40  // Setup simulation box
41
42  nx=5000;
43  ny=225;   // 230
44  nz=10000;
45
46  // Set box size
47
48  sx=5um;
49  sy=900nm;
50  sz=1mm;
51
```

```
52  // Set WG-length
53
54  Prefocus=50um
55  Length=280um
56
57  // Set interested box size
58
59  roix=0.880um;
60  roiy=140nm;
61
62  // Set default values
63
64  setKWithEnergy: 19.9keV;
65  complex nC=1-1.15041234E-06-4.00255384E-10i;
66  complex nMo=1-3.64842936E-06-6.23605203E-08i;
67  complex nGe=1-2.48719084E-06-1.1472121E-07i;
68  complex nVa=1;
69  nvaccum=nVa;
70  nInside=nC;
71  nOutside=nMo;
72  nSubstrate=nGe;
73
74  // Set geometry
75
76  // theory   WGA focus in one point
77  real MoP4=50nm
78  real CP3=4nm
79  real MoP3=56nm
80  real CP2=6.2nm
81  real MoP2=53.8nm
82  real CP1=7.6nm
83  real MoP1=52.4nm
84  real C0=8nm
85  real MoN1=52.4nm
86  real CN1=7.6nm
87  real MoN2=53.8nm
88  real CN2=6.2nm
89  real MoN3=56nm
90  real CN3=4nm
91  real MoN4=50nm
92
93  //// theory   WGM grating type
94  //real MoP4=50nm
95  //real CP3=8nm
96  //real MoP3=52nm
97  //real CP2=8nm
98  //real MoP2=52nm
99  //real CP1=8nm
100 //real MoP1=52nm
101 //real C0=8nm
102 //real MoN1=52nm
103 //real CN1=8nm
104 //real MoN2=52nm
105 //real CN2=8nm
106 //real MoN3=52nm
107 //real CN3=8nm
```

```
108  //real MoN4=50nm
109
110  real alpha=0;
111  real dP3=(CP2/2)+(CP3/2)+MoP3;
112  real dP2=(CP2/2)+(CP1/2)+MoP2;
113  real dP1=(C0/2)+(CP1/2)+MoP1;
114  real dN1=(C0/2)+(CN1/2)+MoN1;
115  real dN2=(CN2/2)+(CN1/2)+MoN2;
116  real dN3=(CN3/2)+(CN2/2)+MoN3;
117  real dA=dN1+dN2+dN3+CN3/2+MoN4;
118
119  // WGA (1-D) with seven channels
120  bool InsideWaveguide_1(real x,real y,real z)=( (x+dP1+dP2+dP3) < (CP3
        /2) & -(CP3/2) < (x+dP1+dP2+dP3) ) ;
121  bool InsideWaveguide_2(real x,real y,real z)=( (x+dP1+dP2) < (CP2/2)
        & -(CP2/2) < (x+dP1+dP2) ) ;
122  bool InsideWaveguide_3(real x,real y,real z)=( (x+dP1) < (CP1/2) & -(
        CP1/2) < (x+dP1) ) ;
123  bool InsideWaveguide_4(real x,real y,real z)=( x < (C0/2) & -(C0/2) <
         x ) ;
124  bool InsideWaveguide_5(real x,real y,real z)=( (x-(dN1)) < (CN1/2) &
        -(CN1/2) < (x-(dN1)) ) ;
125  bool InsideWaveguide_6(real x,real y,real z)=( (x-(dN1+dN2)) < (CN2
        /2) & -(CN2/2) < (x-(dN1+dN2)) ) ;
126  bool InsideWaveguide_7(real x,real y,real z)=( (x-(dN1+dN2+dN3)) < (
        CN3/2) & -(CN3/2) < (x-(dN1+dN2+dN3)) ) ;
127
128  real bound=4*(dA);
129  complex N(real x, real y, real z){
130  complex absorber=0;
131  real dist=sqrt(x*x+y*y);
132  if dist>bound :absorber =i*(dist-bound)*imag(nMo)*100;
133  }=(z>Length+Prefocus | z<Prefocus ? nvaccum:((x<-(dA))|(x>(dA))?
        nSubstrate:(InsideWaveguide_1(x,y,z) | InsideWaveguide_2(x,y,z)|
        InsideWaveguide_3(x,y,z) | InsideWaveguide_4(x,y,z)|
        InsideWaveguide_5(x,y,z) | InsideWaveguide_6(x,y,z)|
        InsideWaveguide_7(x,y,z) ?nInside:nOutside))+absorber);
134
135  // incident-wave
136  double alpha_ins = 0.00degrees
137  double dist = 0
138
139  // Incoming beam using 1-D Gauss-wave
140  //complex realgauss(real r,real z,real E0,real w0,real k)=gauss(r,z,
        E0,w0,k)*exp(-i*k*z);
141  //complex Initial(real x,real y,real z){ real r=sqrt(x^2+y^2)-dist;
        }=realgauss(r*cos(alpha_ins)-z*sin(alpha_ins),z*cos(alpha_ins)+r*
        sin(alpha_ins),1,250nm,k)/exp(-i*k*z);
142
143  //  Incoming beam using 2-D Gauss-wave 2-D
144  //complex realgauss(real x, real y,real z,real E0,real wx0,real wy0,
        real k)=gauss2D(x,y,z,E0,wx0,wy0,k)*exp(-i*k*z);
145  //complex Initial(real x,real y,real z)=realgauss(x*cos(alpha_ins)-z*
        sin(alpha_ins),y*cos(alpha_ins)-z*sin(alpha_ins),z*cos(alpha_ins)
        +sqrt(x^2+y^2)*sin(alpha_ins),1,300nm,140nm,k)/exp(-i*k*z);
146
```

```
147  //   Incoming beam using Plane-wave
148
149  complex planewave(real z) =  exp(-i*k*z);
150  complex Initial(real x,real y,real z)=planewave(x * sin(alpha_ins) +
         z * cos(alpha_ins))/exp(-i*k*z);
151  complex U0(real x,real y,real z)=z<Prefocus ?Initial(x,y,z):( x<(C0
         /2+MoN1) &x>-(C0/2+MoP1)& z>Prefocus && z<=Prefocus+Length ?
         Initial(x,y,z)*exp(-i*(nOutside-1)*k*z):0);
152
153  // Setup finite difference solver
154
155  n=N:(real,real,real);
156  initial=Initial:(real,real,real);
157  u0=U0:(real,real,real);
158  F=F_wave:(real,real,real);
159  A=A_wave();
160
161  // Set the sampler
162
163  MyFDSampler2D(int zi,real z,cpp_field &simField){
164
165   // Define variables
166     real roi;
167     if roix==0: roi=sx;
168     else roi=roix;
169     int nroiX=floor(nx*roi/sx);
170     int nroiY=floor(ny*roi/sy);
171     int nxbegin=floor((nx*(1-roi/sx))/2);
172     int nybegin=floor((ny*(1-roi/sy))/2);
173
174
175     if zi==0: {
176       // Initialize sampler
177       int nroiX=floor(nx*roi/sx);
178       FDS2DField.resize(nz,nroiX);
179       FDS2DFrontImg.resize(simField.width,simField.height,1);
180
181       if FDS_plot: {
182         FDS2DImg.resize(nz,nroiX,1);
183         fill FDS2DImg: 0;
184       }
185     }
186
187     // Sample
188     for int xi from 0 to nroiX-1:{
189       FDS2DField[zi,xi]=simField[floor(ny/2)+1,xi+nxbegin];
190       if FDS_plot: FDS2DImg[zi,xi]=abs(FDS2DField[zi,xi]); // Norm
             creates too hight contrast
191     }
192
193     // save the 2-D pattern of xy plane with different z position
194     // get the field in x-y plane at the distance zi = 3130 (the
             desired pixel number in z direction)
195     if zi == 3130: {
196       string filename
197       filename << "Data/cross_" << zi << ".dat"
```

```
198        IO & file = open(filename.c_str())
199        for int xi from 0 to FDS2DFrontImg.width-1: {
200          for int yi from 0 to FDS2DFrontImg.height-1: file << abs(
                 simField[xi,yi]) << "\t"
201          file << "\n"
202        }
203        file.flush()
204      }
205
206
207      // Status update and plot
208      if FDS_status: io << clearline << iobold << "Simulation running: "
             << ioreset << floor(zi/nz*100) << "%";
209      if FDS_plot: {
210        //for int xi from 0 to FDS2DFrontImg.width-1: for int yi from 0
               to FDS2DFrontImg.height-1: FDS2DFrontImg[xi,yi]=abs(simField[
               xi,yi]);
211        show: FDS2DImg;
212        //show: FDS2DFrontImg;
213        field tmp = field(simField)
214        plot: tmp
215      }
216
217      if FDS_status & zi==nz-1:{
218        // Finalize sampler
219        FDS2DExitField=simField;
220        io << clearline << iobold << "Simulation complete. " << ioreset <<
               "Recorded field name is 'FDS2DField'." << endl;
221      }
222    }
223
224    sample1D=FDSampler1D:(int,real,cpp_vector&);
225    sample2D=MyFDSampler2D:(int,real,cpp_field&);
226
227    // Sweep function
228    // Sweep
229
230    Sweep_1D(){
231      bool op=FDS_plot;
232      bool stat=FDS_status;
233      FDS_plot=false;
234      FDS_status=false;
235
236      for int i from 1 to 250: {
237        alpha_ins=i*0.001degrees;
238        io << "Set alpha_ins to " << i*0.001 << " degrees" << endl;
239        run1D();
240        realplot: abs(FDS1DField);
241      }
242
243      FDS_plot=op;
244      FDS_status=stat;
245    }
246
247    // Usage message
248
```

```
249 | clear();
250 | io << iobold << "Waveguide " << ioreset << "simulation loaded, enter
    |     'run1D()', 'Sweep_1D()', or 'run2D()' to start simulation." <<
    |     endl;
```

A.1.4 Phase retrieval methods using ER and HIO algorithms

phase_retrieval.m

```matlab
1  % The object reconstruction and propagation
2  % Qi Zhong's version
3
4  %% Default settings for images
5  clear all
6  close all
7  clc
8  % set(0,'DefaultFigureColor',[0.9 0.9 0.9]);
9  % set(0,'DefaultAxesFontSize',18);
10 % set(0,'DefaultAxesFontWeight','bold');
11 %% path to matlab tools
12 addpath /homegroups/AG_Salditt/Messzeiten/2016/GINIX/Analysis/
       Qi_Zhong/TJ0415M722/Eiger/reconstruction/ErrorReduction_backup
13 addpath /net/roentgen/home/AG_Salditt/Messzeiten/2016/GINIX/Analysis/
       Qi_Zhong/TJ0415M722/Eiger/reconstruction/ErrorReduction_backup
14 addpath /homegroups/AG_Salditt/Messzeiten/2016/GINIX/Analysis/
       Qi_Zhong/TJ0415M722/Eiger/reconstruction/
       phase_retrieval_algorithms
15 folder='/net/roentgen/home/AG_Salditt/Messzeiten/2016/GINIX/Analysis/
       Qi_Zhong/TJ0415M722/Eiger/reconstruction/Waveguide_reconstruction
       '   % for ruprecht
16 subfolder=sprintf('%s','/data');
17 % subfolder1=sprintf('%s','/best');
18 %% Das Experiment
19 E=13.8;                        %Energie [keV]
20 lambda=12.398/E*1e-10;         %Wellenlnge [m]
21 z=5.4;                          %distance wg - detector [m]
22 d2x=75e-6;                      %Pixelgr  e Detektor [m]
23 d2y=75e-6;
24 %% import data
25 M2=importdata('TJ0415M721_2D_pattern.mat');
26 M33=importdata('TJ0415M721_2D_pattern_1.mat');
27 figure(1);imagesc(log10(M2))
28 set(gca,'FontSize',20);
29 title('TJ0415M721 g2vg 0.03');
30 figure(1);imagesc(log10(M33))
31 set(gca,'FontSize',20);
32 title('TJ0415M721 g2vg 0.03');
33 % set roi
```

```
34  roi.h_min=63;
35  roi.h_max=2112;
36  roi.v_min=103;
37  roi.v_max=152;
38  M1=M2(roi.v_min:roi.v_max,roi.h_min:roi.h_max);
39  figure(21);imagesc(log10(M1));colorbar
40  set(gca,'FontSize',20);
41  title('roi image pattern for TJ0415M721');
42  caxis([0 7])
43  M=M1;
44  P.size_original_x=size(M1,2);
45  P.size_original_y=size(M1,1);
46  %% read in data create equal number of pixels in x and y
47  for i=1:size(M,1)
48      for j=1:size(M,2)
49  if log10(M(i,j))>8
50      M(i,j)=0;
51  end
52      end
53  end
54  M=padarray(M,[50/0.05 0],'both'); % ensure equal resolution
        vertical size/2
55  figure(3);imagesc(log10(M))
56  %% mask for measurements
57  mask=zeros(size(M,1),size(M,2));
58  mask(:,456:495)=0;
59  mask(:,1007:1047)=0;
60  mask(:,1558:1598)=0;
61  figure(3);imagesc(log10(mask))
62  %% padding with zeros for larger resolution
63  mask1=padarray(mask,[60 60],'both');
64  M=padarray(M,[60 60],'both');
65  M=abs(M);
66  % reconstruct range
67  range=2170; %2170
68  center=1085;
69  M11=M(center-range/2+1:center+range/2,center-range/2+1:center+range
        /2);
70  mask=mask1(center-range/2+1:center+range/2,center-range/2+1:center+
        range/2);
71  figure(31);imagesc(log10(M11));colorbar
72  set(gca,'FontSize',20);
73  title('image pattern in larger resolution');
74  caxis([0 7])
75  %% measured data and mask given to data structure P
76  P.mask=mask;
77  P.M=M11;
78  %% Coordinatesystem
79  %pixelsize at waveguide exit = in real space
80  d1x=lambda*z/size(M,2)/d2x;
81  d1y=lambda*z/size(M,1)/d2y;
82  %  beam size on the sample
83  bs.v=46*d1y;
84  bs.h=230*d1x;
85  % Coordinatesystem in real space
86  [x,y]=create_cosy(M11,d1x,d1y);
```

```
87   %% primary condition
88   [X Y]=meshgrid(x,y);
89   % % Autocorrelation for the primary start
90   AC=abs(fftshift(ifft2(ifftshift(M11))));
91   u=AC>0.2*max(max(AC));  % amplitude
92
93   % amplitude and planar phase in object plane for ER
94   u = abs(u).*exp(1i*zeros(size(u)));
95
96   % amplitude and random phase in object plane for HIO
97   % u = abs(u).*exp(1i*rand(size(u)));
98   %% Define a support = place at waveguide exit
99   % the variables of the support position
100  bs.h=230;
101  bs.v1=46;
102  bs.v2=460;
103  bs.v3=23;
104  P.initial_start=zeros(size(M));
105  %  the geometry of the WGA in y direciton
106  w1=abs(1112-1068);
107  w2=abs(1115-1063);
108  w3=abs(1129-1047);
109  w4=abs(1134-1038);
110  w5=abs(1124-1044);
111  w6=abs(1109-1057);
112  w7=abs(1103-1059);
113  w8=abs(1092-1077);
114  P.initial_support=zeros(size(M));
115  P.initial_support1=zeros(size(M));
116  dd=97; % the tails of the beam  27--230,
117  % shift and adjustment
118  L1=2;
119  L2=L1;
120  L3=2;
121  L4=-90;
122  %% tight support
123
124  % P.initial_support(center-bs.v2/2-w1/2:center+bs.v2/2+w1/2,980-L3-L4
         :997+L3-L4)=1   ; % #1   % (y,xn1:n2)
125  % P.initial_support(center-bs.v2/2-w2/2:center+bs.v2/2+w2/2,1015-L1-
         L4:1032+L2-L4)=1  ;  % #2
126  % P.initial_support(center-bs.v2/2-w3/2:center+bs.v2/2+w3/2,1043-L1-
         L4:1067+L2-L4)=1  ;  % #3
127  % P.initial_support(center-bs.v2/2-w4/2:center+bs.v2/2+w4/2,1075-L1-
         L4:1097+L2-L4)=1  ;  % #4
128  % P.initial_support(center-bs.v2/2-w5/2:center+bs.v2/2+w5/2,1105-L1-
         L4:1129+L2-L4)=1   ; % #5
129  % P.initial_support(center-bs.v2/2-w6/2:center+bs.v2/2+w6/2,1140-L1-
         L4:1158+L2-L4)=1   ; % #6
130  % P.initial_support(center-bs.v2/2-w7/2:center+bs.v2/2+w7/2,1175-L3-
         L4:1191+L3-L4)=1  ;  % #7
131
132  %% loose support
133
134  P.initial_support(center-bs.v2/2-w4/2:center+bs.v2/2+w4/2,940-L3-L4
         :1231+L3-L4)=1;
```

```
135
136  %% set for different thresholds for different supports or different
         algorithms
137  P.S1=P.initial_support(center-range/2+1:center+range/2,center-range
         /2+1:center+range/2);
138  P.S2=P.initial_support(center-range/2+1:center+range/2,center-range
         /2+1:center+range/2);
139  P.S3=P.initial_support(center-range/2+1:center+range/2,center-range
         /2+1:center+range/2);
140  py=size(P.S1(:,1));
141  px=size(P.S1(:,2));
142  figure(51);imagesc(px*3,py*3,abs(P.S2)); colorbar
143  set(gca,'FontSize',16);
144  axis([2700 3800 2300 4200]);
145  title('Support');
146
147  % N iterations
148  P.it=2500;
149  % different thresholds for the HIO+ER algorithm
150  P.threshold1=2500;
151  P.threshold2=2500;
152  %%  Reconstruction with different algorithms ER and HIO
153
154  % for ER algorithm
155  [uout,Error,U]=ErrorReduction(u,P);
156
157  % for HIO algorithm
158  % P.HIO_parameter_beta=1;
159  % [uout,Error,U,L_M,L_U,Im_U,Im_M,u_a]=HIO_algorithm(u,P);
160
161  % object plane
162  psi=uout;
163  %% set the roi for the object plane using in free propagation
164  range1=680;
165  psi2=psi(center-range1/2+1:center+range1/2,center-range1/2+1:center+
         range1/2);
166  u1=zeros(size(M));
167  u1(center-range/2+1:center+range/2,center-range/2+1:center+range/2)=
         uout;
168  %% free propagate
169  d1x=lambda*z/size(M,2)/d2x; %pixelsize at waveguide exit = in real
         space
170  d1y=lambda*z/size(M,1)/d2y;
171  % the propagation distance
172  Nz=1000;
173  Delta_z=0.69e-3;
174  dist=linspace(0,Delta_z,Nz);
175  stepsize=1e-7;    % -- 100 nm
176  i_n=0;
177  % basic set
178  Psimatrix1 = zeros(size(psi2,1),Nz);
179  Imatrix1 = zeros(size(psi2,1),Nz);
180  Psimatrix = zeros(size(psi2,1),Nz);
181  Imatrix = zeros(size(psi2,1),Nz);
182  z1=[1:Nz];
183  x1=[1:size(psi2,1)];
```

```
184  x2=[1:size(M11,1)];
185  % used for 1-D propagation
186  L_near1=sum(abs(psi2),1);
187  % set the F funtion for 1-D propagation
188  F=d1x^2/lambda./dist;
189  % primary I0
190   I0=5.2e9;
191  for iii=1:max(size(dist))
192      %% 2-D free progation both in x-z and x-y planes
193  %     tmp_prop1=prop_nf_pa_2D(psi2,lambda,dist(iii),d1x,d1y,3); %,X)
           vergr  ern (1 bis 10 oder so), damit aliasing nicht auftritt
194  %     % in x-y plane
195  %     psi_prop1(:,:,iii)=tmp_prop1;
196  %     L_near11(:,iii)=sum(abs(psi_prop1(:,:,iii)),1);
197  %     Psimatrix1(:,iii)=L_near11(:,iii);
198  %     % in x-z plane
199  %     Imatrix1 = abs(Psimatrix1).^2
200  %     clear tmp_prop1
201      %% 1-D free progation in x-z planes
202      Psimatrix(:,iii) = prop_nf_pa_1d_F1(abs(L_near1),F(iii),3);
203      Imatrix = abs(Psimatrix).^2;
204  end
205  %% x-z plane figures
206      figure(1002)
207      imagesc(z1*stepsize/1e-6,x1*d1x/1e-9,(Imatrix)/I0);colorbar
208      set(gca,'FontSize',16);
209      xlabel('distance / um','FontSize',16)
210      ylabel('width / nm','FontSize',16)
211      axis([1 690 640 1340]);
212      caxis([0 0.2])
213      title('near field propagation in x-z plane')
214  %% x-y plane figures at the distance ii
215  ii=1370
216  pos=ii*stepsize/1e-6;
217  near=psi_prop1(:,:,ii);
218      figure(1003)
219      imagesc(x1*d1x/1e-9*0.5,x1*d1x/1e-9,abs(near)/4e7)
220      set(gca,'FontSize',16);
221      title(ii);colorbar
222      caxis([0 3e-6])
223      axis([1 1400*0.5 850 1150]);
224      title('near field propagation in x-y plane')
```

ErrorReduction.m

```
1  % The Error reduction algorithm
2  % The original source code is from Anna-Lena Robisch
3  % Qi Zhong revised.
4
5  function [uout,Error,U]=ErrorReduction(u,P)
```

```
6  %%
7  close all
8  M_mask=P.M;
9  it=P.it;
10 %threshold1=P.threshold1;
11 %threshold2=P.threshold2;
12 S1=P.S1;
13 S2=P.S2;
14 S3=P.S3;
15
16 %%
17 clear error;
18 %%  start the algorithm
19 for iii=1:1:it
20     %% different threshold for different supports
21     if iii < P.threshold1;
22         S=S1;
23     elseif P.threshold1<iii < P.threshold2;
24         S=S2;
25     else
26         S=S3;
27     end
28
29     %% amplitude constraint in detector plane
30
31     U=DFT(u);
32
33     %% Calculate Error
34     U_nor=abs(cut2Darray(U,P.size_original_x,P.size_original_y)).^2;
35     U_nor=U_nor./max(max(U_nor));
36     M_nor=cut2Darray(P.M,P.size_original_x,P.size_original_y);
37     M_nor=M_nor./max(max(M_nor));
38     % the different types of error
39     Error.nor(iii,1)=sum(sum(sqrt(abs(U_nor-M_nor))))/...
40         (P.size_original_x*P.size_original_y);
41     Error.error(iii,1)=sum(sum(sqrt(abs(abs(cut2Darray(U,...
42         P.size_original_x,P.size_original_y)).^2-...
43         cut2Darray(P.M,P.size_original_x,...
44         P.size_original_y)))))/(P.size_original_x*P.size_original_y);
45     error_nor=Error.nor;
46     error=Error.error;
47
48      %% Plot error
49
50     figure(4)
51 %     plot(log10(error_mask),'Color','black');
52 %     hold on
53 %     plot(log10(error_mask_nor),'Color','green');
54     plot(error,'Color','blue');
55 %     plot(log10(error_nor),'Color','red');
56     drawnow
57
58     %% set Intensities
59
60     Im_U=abs(cut2Darray(U,P.size_original_x,P.size_original_y)).^2;
61     Im_M=cut2Darray(P.M,P.size_original_x,P.size_original_y);
```

```
62      L_U=sum(Im_U,1);
63      L_M=sum(Im_M,1);
64
65      %% Do amplitude Constraint
66
67      u=IDFT(U./(abs(U)+1e-20).*sqrt(P.M));
68
69      %% Do Support constraint
70
71      u=S.*u;
72
73   end
74   % output
75   uout=u;
```

HIO_algorithm.m

```
1    % The Error reduction algorithm
2    % The original source code is from Anna-Lena Robisch
3    % Qi Zhong revised.
4
5    function [uout,Error,U,L_M,L_U,Im_U,Im_M,u_a]=HIO_algorithm(u,P)
6    %%
7    close all
8    mask=P.mask;
9    M_mask=P.M;
10   it=P.it;
11   n=P.averagen;
12   HIO_parameter_beta=P.HIO_parameter_beta;
13   S1=P.S1;
14   S2=P.S2;
15   S3=P.S3;
16   clear error;
17   S=S1;
18   u_a=zeros(size(u));
19   %% start the algorithm
20   for iii=1:1:it
21       %% amplitude constraint in detector plane
22
23       U=DFT(u);
24
25       %% Calculate Error
26       % set
27       U_mask=U-U.*mask;
28       U_mask_nor=abs(cut2Darray(U_mask,P.size_original_x,P.
             size_original_y)).^2;
29       U_mask_nor=U_mask_nor./max(max(U_mask_nor));
30       M_mask_nor=cut2Darray(M_mask,P.size_original_x,P.size_original_y)
             ;
31       M_mask_nor=M_mask_nor./max(max(M_mask_nor));
```

```
32      U_nor=abs(cut2Darray(U,P.size_original_x,P.size_original_y)).^2;
33      U_nor=U_nor./max(max(U_nor));
34      M_nor=cut2Darray(P.M,P.size_original_x,P.size_original_y);
35      M_nor=M_nor./max(max(M_nor));
36      B_M=abs(cut2Darray(U,P.size_original_x,P.size_original_y)).^2;
37      sumbm=sum(sum(B_M));
38      % the different types of error
39      Error.mask_nor(iii,1)=sum(sum(sqrt(abs(U_mask_nor-M_mask_nor))))
            /...
40          (P.size_original_x*P.size_original_y);
41      Error.mask(iii,1)=sum(sum(sqrt(abs(abs(cut2Darray(U_mask,...
42          P.size_original_x,P.size_original_y)).^2-...
43          cut2Darray(M_mask,P.size_original_x,...
44          P.size_original_y)))))/(P.size_original_x*P.size_original_y);
45      Error.nor(iii,1)=sum(sum(sqrt(abs(U_nor-M_nor))))/...
46          (P.size_original_x*P.size_original_y);
47      Error.error(iii,1)=sum(sum(sqrt(abs(abs(cut2Darray(U,...
48          P.size_original_x,P.size_original_y)).^2-...
49          cut2Darray(P.M,P.size_original_x,...
50          P.size_original_y)))))/(P.size_original_x*P.size_original_y);
51      Error.errorM(iii,1)=sqrt(sum(sum(abs(abs(cut2Darray(U,...
52          P.size_original_x,P.size_original_y)).^2-...
53          cut2Darray(P.M,P.size_original_x,...
54          P.size_original_y))))/sumbm);
55      %%  plot error
56      error_mask_nor=Error.mask_nor;
57      error_mask=Error.mask;
58      error_nor=Error.nor;
59      error=Error.error;
60      error_M=Error.errorM;
61
62      figure(4)
63      subplot(2,2,1)
64       plot(log10(error_M),'Color','black');
65       title('error_M')
66      subplot(2,2,2)
67       plot((error_mask_nor),'Color','green');
68       title('error_mask_nor')
69      subplot(2,2,3)
70       plot(error,'Color','blue');
71       title('errork')
72      subplot(2,2,4)
73       plot((error_nor),'Color','red');
74       title('error_nor')
75      drawnow
76      %% set Intensities
77      Im_U=abs(cut2Darray(U,P.size_original_x,P.size_original_y)).^2;
78      Im_M=cut2Darray(P.M,P.size_original_x,P.size_original_y);
79      L_U=sum(Im_U,1);
80      L_M=sum(Im_M,1);
81
82      %% Do amplitude Constraint
83      u_corr=IDFT(U./(abs(U)+1e-20).*sqrt(P.M)+U.*mask);
84      %% Do Support constraint
85      % different thresholds for different algorithms
86      if iii < P.threshold1;
```

```matlab
 87            u = S.*u_corr+ (1-S).*(u-HIO_parameter_beta*u_corr);    % HIO
 88        elseif P.threshold1<iii < P.threshold2;
 89            u=S.*u_corr;                                            % ER
 90        else
 91            S=S3;
 92        end
 93        % average from last 50 graphs
 94        if (it-n) < iii;
 95            u_a = abs(u_a)+abs(u);    % HIO
 96            figure(2)
 97            imagesc((abs(u_a)));
 98        end
 99  end
100  % output
101  Im_U=Im_U;
102  Im_M=Im_M;
103  L_M=L_M;
104  L_U=L_U;
105  U=U;
106  error.mask_nor=Error.mask_nor;
107  error.mask=Error.mask_nor;
108  error.nor=Error.nor;
109  error.error=Error.error;
110  error.errorM=Error.errorM;
111  u_a=u_a;
112  uout=u;
```

B.1   The PyPropagate source code for the Resonant beam couplers

B.1.1   The design of RBC structure

The design of Resonant Beam Couplers

```
In [1]:   from pypropagate import *
          import matplotlib.pyplot as plt
          import matplotlib as mpl
          from matplotlib import animation, rc
          import scipy.interpolate as interpolate
          from IPython.display import HTML
          import cmath
          from matplotlib.colors import LogNorm
          import math
```

```
In [2]:   %matplotlib inline
          mpl.rcParams['animation.bitrate'] = 20000
```

Create the settings

```
In [3]:   settings = presets.settings.create_paraxial_wave_equation_settings()
          pde = settings.partial_differential_equation
          presets.boundaries.set_plane_wave_initial_conditions(settings)
          s = settings.symbols
          s.u_boundary = 0
```

Define the Gaussian beam

```
In [4]:   g = settings.create_category('gaussian',info='Parameters of the gaussian be
          am')
          g.create_symbol('sigma_x',info = 'Waist size at z = 0', type=pc.Types.Rea
          l,positive=True)
          g.create_symbol('alpha',info = 'angle',type=pc.Types.Real,positive=True)
          g.create_function('w_x',(s.z,),pc.sqrt(2)*pc.sqrt(g.sigma_x**2+2*pd
          e.A*s.z),info = 'Waist size')
          g.create_function('u_0',(s.x,s.y,s.z),g.sigma_x/(g.w_x) *pc.exp(-
          s.x**2/(g.w_x**2)));
          xa,za = pc.cos(g.alpha)*s.x-pc.sin(g.alpha)*s.z,pc.cos(g.alpha)*s.z+pc.si
          n(g.alpha)*s.x
          g.create_function('u',(s.x,s.y,s.z),g.u_0.function(xa,s.y,za)*pc.exp(-1
          j*s.k*(za - s.z) ));
          settings.get(g.u_0)
```

Out[4]:

$$\exp\left[-\cfrac{1}{2\ (\sigma \quad ^2-\frac{c\,i\,z}{ })}\ x^2\right]\ (2\ (\sigma_{x_{\text{gaussian}}}{}^2-\cfrac{c\,i\,z}{\omega\,n(x,y,z)}\ ))^{-\frac{1}{2}}\ \sigma_{x_{\text{ga}}}$$

Set pulse paramters

```
In [5]: g.sigma_x = 600 * units.nm / (pc.sqrt(8*pc.log(2))) #beam size FWHM
        alpha = pc.parameter('alpha',0.135) #incident angle
        g.alpha = -alpha * units.degrees
```

Define the refractive index

```
In [6]: s_padding = 1000*units.nm
        d_padding = 100*units.nm
        r_padding = pc.piecewise((0,s.xmax - s.x>d_padding + s_padding),((s.x - s.x
        max + d_padding + s_padding)/s_padding, s.xmax - s.x>d_padding),(1,True))
        n_padding = r_padding * settings.numerics.create_symbol("n_GaAs",1-5.042959
        86E-06-4.4443712E-07j) + (1-r_padding)
```

Set the RBC structure

```
In [7]: #symbol of the different layers index
        r = settings.create_category('resonator')
        r.create_function('n_1',(s.omega,))
        r.create_function('n_2',(s.omega,))
        r.create_function('n_3',(s.omega,))
        r.create_function('n_4',(s.omega,))
        r.create_function('n_5',(s.omega,))
        r.create_function('n_6',(s.omega,))
        r.create_function('n_7',(s.omega,))
        r.create_function('n_8',(s.omega,))
        #symbol of the different layers
        r.create_symbol('d_1')
        r.create_symbol('d_2')
        r.create_symbol('d_3')
        r.create_symbol('d_4')
        r.create_symbol('d_5')
        r.create_symbol('d_6')
        r.create_symbol('d_7')
        r.create_symbol('d_max',r.d_1+r.d_2+r.d_3+r.d_4+r.d_5+r.d_6+r.d_7)
        #positions of the different layers index
        r.create_function('n',(s.x,s.omega),pc.piecewise(
                (n_padding,s.x>0),
                (r.n_1,s.x>-r.d_1),
                (r.n_2,s.x>-(r.d_1+r.d_2)),
                (r.n_3,s.x>-(r.d_1+r.d_2+r.d_3)),
                (r.n_4,s.x>-(r.d_1+r.d_2+r.d_3+r.d_4)),
                (r.n_5,s.x>-(r.d_1+r.d_2+r.d_3+r.d_4+r.d_5)),
                (r.n_6,s.x>-(r.d_1+r.d_2+r.d_3+r.d_4+r.d_5+r.d_6)),
                (r.n_7,s.x>-(r.d_1+r.d_2+r.d_3+r.d_4+r.d_5+r.d_6+r.d_7)) ,
                (r.n_8,True) ) );
```

Set refractive index paramters

```
In [8]: r.n_1 = settings.numerics.create_symbol("n_Ni", 1-9.34051513E-06-5.64049571
        E-07j)
        r.n_2 = settings.numerics.create_symbol("n_C", 1-2.39850965E-06-1.34966505
        E-09j)
        r.n_3 = settings.numerics.create_symbol("n_Ni", 1-9.34051513E-06-5.64049571
        E-07j)
        r.n_4 = settings.numerics.create_symbol("n_C", 1-2.39850965E-06-1.34966505
        E-09j)
        r.n_5 = settings.numerics.create_symbol("n_Ni", 1-9.34051513E-06-5.64049571
        E-07j)
        r.n_6 = settings.numerics.create_symbol("n_C", 1-2.39850965E-06-1.34966505
        E-09j)
        r.n_7 = settings.numerics.create_symbol("n_Ni", 1-9.34051513E-06-5.64049571
        E-07j)
        n_GaAs = settings.numerics.create_symbol("n_GaAs", 1-5.04295986E-06-4.44437
        12E-07j)
        ## substrate
        cladding_width = 0.4*units.um
        p = pc.Min(pc.Max(0,s.x + r.d_max + 1 * units.um)/cladding_width,1)
        r.n_8 =  p * n_GaAs + (1-p) * n_GaAs
        ## layer thickness
        r.d_1 = 5*units.nm
        r.d_2 = 50*units.nm
        r.d_3 = 5*units.nm
        r.d_4 = 50*units.nm
        r.d_5 = 5*units.nm
        r.d_6 = 50*units.nm
        r.d_7 = 50*units.nm
```

```
/usr/lib64/python2.7/site-packages/pypropagate/categorized_dictionary.p
y:151: UserWarning: overwriting attribute n_Ni
  warnings.warn("overwriting attribute %s" % name, UserWarning)
/usr/lib64/python2.7/site-packages/pypropagate/categorized_dictionary.p
y:154: UserWarning: overwriting key n_Ni_numerics
  warnings.warn("overwriting key %s" % key, UserWarning)
/usr/lib64/python2.7/site-packages/pypropagate/categorized_dictionary.p
y:170: UserWarning: overwriting attribute n_Ni
  warnings.warn("overwriting attribute %s" % name, UserWarning)
/usr/lib64/python2.7/site-packages/pypropagate/categorized_dictionary.p
y:151: UserWarning: overwriting attribute n_C
  warnings.warn("overwriting attribute %s" % name, UserWarning)
/usr/lib64/python2.7/site-packages/pypropagate/categorized_dictionary.p
y:154: UserWarning: overwriting key n_C_numerics
  warnings.warn("overwriting key %s" % key, UserWarning)
/usr/lib64/python2.7/site-packages/pypropagate/categorized_dictionary.p
y:170: UserWarning: overwriting attribute n_C
  warnings.warn("overwriting attribute %s" % name, UserWarning)
/usr/lib64/python2.7/site-packages/pypropagate/categorized_dictionary.p
y:151: UserWarning: overwriting attribute n_GaAs
  warnings.warn("overwriting attribute %s" % name, UserWarning)
/usr/lib64/python2.7/site-packages/pypropagate/categorized_dictionary.p
y:154: UserWarning: overwriting key n_GaAs_numerics
  warnings.warn("overwriting key %s" % key, UserWarning)
/usr/lib64/python2.7/site-packages/pypropagate/categorized_dictionary.p
y:170: UserWarning: overwriting attribute n_GaAs
  warnings.warn("overwriting attribute %s" % name, UserWarning)
```

In [9]:
```
s.n = r.n
settings.get_numeric(s.n)
```

Out[9]:

$$
\begin{cases}
0 & \text{if } \frac{11\,\text{m}}{10^7} < x_{\max} - x \\
1 + \dfrac{10^6}{\text{m}}\left(\dfrac{11\,\text{m}}{10^7} + x - x_{\max}\right) & \text{if } \frac{\text{m}}{10^7} < x_{\max} - x \quad \left(-\dfrac{252147993}{5\cdot 10^{13}} - \dfrac{694433\,i}{15625\cdot 10^8}\right) \\
1 & \text{otherwise}
\end{cases}
$$

$$
\begin{array}{l}
\dfrac{99999065948487}{10^{14}} - \dfrac{564049571\,i}{10^{15}} \\[4pt]
\dfrac{19999952029807}{2\cdot 10^{13}} - \dfrac{26993301\,i}{2\cdot 10^{16}} \\[4pt]
\dfrac{99999065948487}{10^{14}} - \dfrac{564049571\,i}{10^{15}} \\[4pt]
\dfrac{19999952029807}{2\cdot 10^{13}} - \dfrac{26993301\,i}{2\cdot 10^{16}} \\[4pt]
\dfrac{99999065948487}{10^{14}} - \dfrac{564049571\,i}{10^{15}} \\[4pt]
\dfrac{19999952029807}{2\cdot 10^{13}} - \dfrac{26993301\,i}{2\cdot 10^{16}} \\[4pt]
\dfrac{99999065948487}{10^{14}} - \dfrac{564049571\,i}{10^{15}} \\[4pt]
\dfrac{49999747852007}{5\cdot 10^{13}} - \dfrac{694433\,i}{15625\cdot 10^8}
\end{array}
$$

Set the boundary conditions

In [10]:
```
#position of incoming beam
s.u0 = g.u.subs(s.x,s.x-3*g.sigma_x)
s.u_boundary = pc.piecewise( ( s.u0,s.x>0), (0,True) )
```

Set the simulation box

In [11]:
```
s.ymin = -2 * units.um
s.ymax = 2 * units.um
s.xmin = -2 * units.um
s.xmax = 30* units.um
s.zmin = 0
s.zmax =10*units.mm
s.Nz = 5000
s.Ny = 2000
s.Nx = 30000
#working energy
settings.wave_equation.set_energy(13.8*units.keV)
```

Plot the refractive index

In [25]:
```
plot(pc.real(s.n),settings);
```
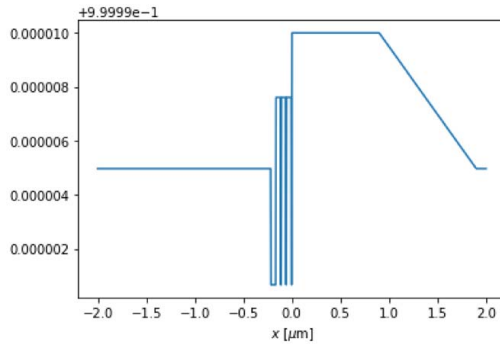

Figure out necessarry simulation box resolution

In [13]:
```
#incident angle
alpha.set_value(0.216)
```

In [14]:
```
# set the pixel sizes in x and z directions
test_settings = settings.copy()
test_settings.wave_equation.n = 1
test_settings.simulation_box.zmin = 0
test_settings.simulation_box.zmax = 5 * units.mm
test_settings.simulation_box.xmax = 5 * units.um
test_settings.simulation_box.xmin = -15 * units.um
test_settings.simulation_box.Nx = 20000
test_settings.simulation_box.Nz = 50000
settings.simulation_box.Nx = test_settings.get_numeric(test_settings.simula
tion_box.Nx)
settings.simulation_box.Nz = test_settings.get_numeric(test_settings.simula
tion_box.Nz)
```

Calculate the stationary field

In [15]:
```
propagator = propagators.FiniteDifferences2D(settings)
stationary_field = propagator.run_slice()[-0.5*units.um:7*units.um,0:4*unit
s.mm:s.sz/24000] # choosing simulation region
```

```
propagating:|███████████████| 9999/9999 [57.8s < 0(0)s]]
```

In [16]:
```
plot(abs(stationary_field),vmax=1)
np.shape(abs(stationary_field))
```
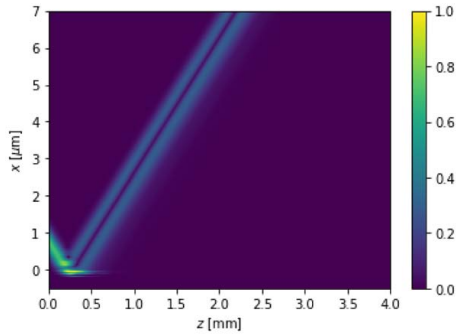

Out[16]: (4688, 10000)

In [17]:
```
# setting the certain plane to collecting near-field information
center = (3.3*units.um,1.5 *units.mm) #position
extent = 6.5*units.um  # Length
angle = pc.pi/2  # rotation angle
```

In [18]:
```
xe = settings.get_as(((center[0] - pc.sin(angle) * extent/2)/units.um, (cen
ter[0] + pc.sin(angle) * extent/2)/units.um),float)
ze = settings.get_as(((center[1] - pc.cos(angle) * extent/2)/units.mm,  (ce
nter[1] + pc.cos(angle) * extent/2)/units.mm),float)
plot(abs(stationary_field),ax=plt.gca(),vmax=0.9)
plt.plot(ze,xe,color='w')
plt.ylim(-0.2,7)
plt.show()
```
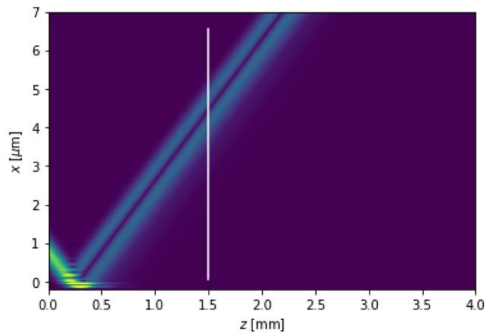
```
In [19]: class Interpolated:
             def __init__(self,data):
                 self._data = data
             def __getitem__(self,s):
                 x,y = s
                 fx,cx = np.floor(x).astype(int), np.ceil(x).astype(int)
                 fy,cy = np.floor(y).astype(int), np.ceil(y).astype(int)
                 ll = self._data[fx,fy]
                 lr = self._data[cx,cy]
                 ul = self._data[fx,cy]
                 ur = self._data[cx,cy]
                 xi = np.fmod(x,1)
                 yi = np.fmod(y,1)
                 return (1-xi) * ((1-yi) * ll + yi * ul) + xi * ((1-yi) * lr + yi *
         ur)
         def create_slice_callback(center,extent,angle,settings):
             l = pc.Symbol('l')
             x0,z0 = center
             zi = s.zi.function( z0 + pc.cos(angle) * (l-0.5)*extent )
             xi = s.xi.function( x0 + pc.sin(angle) * (l-0.5)*extent )
             steps = 5000
             nl = np.linspace(0,1,steps)
             xindicesexpr,zindicesexpr = settings.get_optimized((xi,zi))
             xindices,zindices = [i.real for i in pc.numpyfy((xindicesexpr,zindicese
         xpr))(l=nl)]
             cache = np.zeros(settings.get_as((2,s.Nx),int),dtype=np.complex128)
             inter = Interpolated(cache)
             result = CoordinateNDArray(np.zeros(steps,dtype=np.complex128),
                                        [(0,extent)],(s.x,),settings.get_numeric_transf
         orm())
             k = s.k
             angle2 = -angle + pc.pi/2
             dzkcosanglem1 = settings.get_as(k*s.dz*(pc.cos(angle2) - 1),float)
             mdxksinangle  = settings.get_as(-k*s.dx*pc.sin(angle2) ,float)
             ai = [0]
             def callback(propagator):
                 if ai[0] >= steps or propagator._i < np.floor(zindices[0]):
                     return
                 if ai[0] == 0:
                     ai[0] += 1
                     cache[1,:] = propagator._get_field()
                     return
                 cache[0:] = cache[1,:]
                 cache[1:] = propagator._get_field()
                 while ai[0] < steps and zindices[ai[0]] < propagator._i:
                     zi = zindices[ai[0]]
                     xi = xindices[ai[0]]
                     zr = zi - zindices[0]
                     xr = xi - xindices[0]
                     result.data[ai[0]] = inter[zi % 1,xi] * np.exp(1j *
                                             (xi * mdxksinangle + zi * dzkcosanglem1))
                     ai[0] += 1
             return result,callback
```
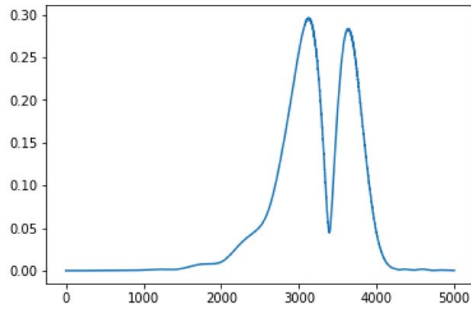
```
In [20]: sliced,callback = create_slice_callback(center,extent,angle,settings)
         propagator = propagators.FiniteDifferences2D(settings)
         propagator.run(callback=callback)
```

```
propagating:|███████████| 49999/49999 [120.7s < 0(0)s]]
```

near field profile
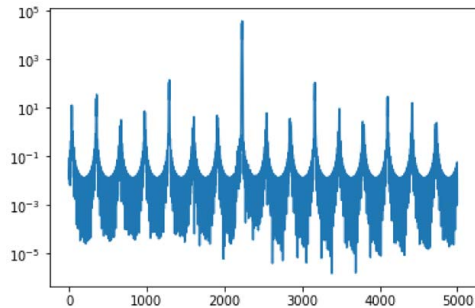
```
In [21]: plt.plot(abs(sliced))
```

```
Out[21]: [<matplotlib.lines.Line2D at 0x7ff0821ba550>]
```


far field profile

```
In [22]: far_fields1 = np.fft.fftshift(np.fft.fft(sliced,axis=0) ,axes = (0,) )
         plt.plot(abs(far_fields1)**2)
         plt.yscale('log')
```

B.1.2 Analyzing and simulating the far-field distribution with different incident angles

RBC g2hg 0.3 mm analysis

In [1]:
```
from pypropagate import *
import matplotlib.pyplot as plt
import matplotlib as mpl
from matplotlib import animation, rc
from matplotlib.colors import LogNorm
import scipy.interpolate as interpolate
from IPython.display import HTML
from scipy import ndimage as nd
import cmath
```

In [2]:
```
%matplotlib inline
```

Create the settings

In [3]:
```
tests = False
```

In [4]:
```
settings = presets.create_2D_paraxial_settings_with_parameter('alpha')
pde = settings.partial_differential_equation
s = settings.symbols
```

Define the Gaussian beam

In [5]:
```
g = settings.create_category('gaussian',info='Parameters of the gaussian be
am')
g.create_symbol('sigma_x',info = 'Waist size at z = 0',type=pc.Types.Real,p
ositive=True)
g.create_symbol('z_0',0)
g.create_symbol('x_0',0)
g.create_function('w_x',(s.z,),pc.sqrt(2)*pc.sqrt(g.sigma_x**2+2/(1j*s.k)*
(s.z - g.z_0)),info = 'Waist size')
g.create_function('u_0',(s.x,s.z),g.sigma_x/(g.w_x)*pc.exp(-(s.x -
g.x_0)**2/(g.w_x**2)));
xa,za = pc.cos(s.alpha)*s.x+pc.sin(s.alpha)*s.z,pc.cos(s.alpha)*s.z-pc.si
n(s.alpha)*s.x
g.create_function('u',(s.x,s.z,s.alpha),g.u_0.function(xa,za)*pc.exp(-1
j*s.k*(za - s.z)));
settings.get(g.u_0)
```

Out[5]:
$$\exp(-\frac{1}{2\,(\sigma_{x_{\text{gaussian}}}{}^2 - \frac{2\,c\,i\,z}{\omega})}\,x^2)\,(2\,(\sigma_{x_{\text{gaussian}}}{}^2 - \frac{2\,c\,i\,z}{\omega}))^{-\frac{1}{2}}\,\sigma_{x_{\text{gaussian}}}$$

In [6]:
```
g.sigma_x = 130 * units.nm / (pc.sqrt(8*pc.log(2))) # FWHM
```

Define the refractive index

```
In [7]:  #symbol of the different layers index
         r = settings.create_category('resonator')
         r.create_function('n_1',(s.omega,))
         r.create_function('n_2',(s.omega,))
         r.create_function('n_3',(s.omega,))
         r.create_function('n_4',(s.omega,))
         r.create_function('n_5',(s.omega,))
         r.create_function('n_6',(s.omega,))
         r.create_function('n_7',(s.omega,))
         r.create_function('n_8',(s.omega,))
         #symbol of the different layers
         r.create_symbol('d_1')
         r.create_symbol('d_2')
         r.create_symbol('d_3')
         r.create_symbol('d_4')
         r.create_symbol('d_5')
         r.create_symbol('d_6')
         r.create_symbol('d_7')
         r.create_symbol('d_max',r.d_1+r.d_2+r.d_3+r.d_4+r.d_5+r.d_6+r.d_7)
         #positions of the different layers index
         r.create_function('n',(s.x,s.omega),pc.piecewise(
                 (1,s.x>0),
                 (r.n_1,s.x>-r.d_1),
                 (r.n_2,s.x>-(r.d_1+r.d_2)),
                 (r.n_3,s.x>-(r.d_1+r.d_2+r.d_3)),
                 (r.n_4,s.x>-(r.d_1+r.d_2+r.d_3+r.d_4)),
                 (r.n_5,s.x>-(r.d_1+r.d_2+r.d_3+r.d_4+r.d_5)),
                 (r.n_6,s.x>-(r.d_1+r.d_2+r.d_3+r.d_4+r.d_5+r.d_6)),
                 (r.n_7,s.x>-(r.d_1+r.d_2+r.d_3+r.d_4+r.d_5+r.d_6+r.d_7)) ,
                 (r.n_8,True) ) );
```

Define some useful values for later.

```
In [8]:  # Cladding layers
         c1 = -r.d_1/2
         c2 = -(r.d_1+r.d_2/2)
         c3 = -(r.d_1+r.d_2+r.d_3/2)
         c4 = -(r.d_1+r.d_2+r.d_3+r.d_4/2)
         c5 = -(r.d_1+r.d_2+r.d_3+r.d_4+r.d_5/2)
         c6 = -(r.d_1+r.d_2+r.d_3+r.d_4+r.d_5+r.d_6/2)
         c7 = -(r.d_1+r.d_2+r.d_3+r.d_4+r.d_5+r.d_6+r.d_7/2)
         # Guiding layers
         d1 = -r.d_1
         d2 = -(r.d_1+r.d_2)
         d3 = -(r.d_1+r.d_2+r.d_3)
         d4 = -(r.d_1+r.d_2+r.d_3+r.d_4)
         d5 = -(r.d_1+r.d_2+r.d_3+r.d_4+r.d_5)
         d6 = -(r.d_1+r.d_2+r.d_3+r.d_4+r.d_5+r.d_6)
         d7 = -(r.d_1+r.d_2+r.d_3+r.d_4+r.d_5+r.d_6+r.d_7)

         dmax = 0
         dmin = -(r.d_1+r.d_2+r.d_3+r.d_4+r.d_5+r.d_6+r.d_7)
```

Set refractive index paramters

```
In [9]:  r.n_1 = presets.create_material('Ni',settings) # cladding layer
         r.n_2 = presets.create_material('C',settings)  # guiding layer
         r.n_3 = presets.create_material('Ni',settings)
         r.n_4 = presets.create_material('C',settings)
         r.n_5 = presets.create_material('Ni',settings)
         r.n_6 = presets.create_material('C',settings)
         r.n_7 = presets.create_material('Ni',settings)
         cladding_width = 0.4*units.um
         p = pc.Min(pc.Max(0,s.x + r.d_max + 1 * units.um)/cladding_width,1)
         #substrate
         r.n_8 =  p * presets.create_material('GaAs',settings) + (1-p)
         * presets.create_material('GaAs',settings)
         # layer structure
         r.d_1 = 5.3*units.nm
         r.d_2 = 47.2*units.nm
         r.d_3 = 5.3*units.nm
         r.d_4 = 47.2*units.nm
         r.d_5 = 5.3*units.nm
         r.d_6 = 47.2*units.nm
         r.d_7 = 50.1*units.nm
```

```
In [10]:  s.n = r.n
          settings.get_numeric(s.n)
```

Out[10]:

$$
\begin{cases}
1 & \text{if } 0 < x \\
n_{\text{Ni}}(\omega) & \text{if } -\frac{53\,\text{m}}{10^{10}} < x \\
n_C(\omega) & \text{if } -\frac{21\,\text{m}}{4\cdot10^8} < x \\
n_{\text{Ni}}(\omega) & \text{if } -\frac{289\,\text{m}}{5\cdot10^9} < x \\
n_C(\omega) & \text{if } -\frac{21\,\text{m}}{2\cdot10^8} < x \\
n_{\text{Ni}}(\omega) & \text{if } -\frac{1103\,\text{m}}{10^{10}} < x \\
n_C(\omega) & \text{if } -\frac{63\,\text{m}}{4\cdot10^8} < x \\
n_{\text{Ni}}(\omega) & \text{if } -\frac{519\,\text{m}}{25\cdot10^8} < x \\
n_{\text{GaAs}}(\omega) & \text{otherwise}
\end{cases}
$$

Set the boundary conditions

```
In [11]:  # position of incoming beam
          s.u0 = g.u.subs(s.x,s.x-3*g.sigma_x)
          s.u_boundary = pc.piecewise( ( s.u0,s.x>0), (0,True) )
          settings.wave_equation.set_energy(13.8*units.keV)
```

Plot the refractive index

```
In [12]:  s.xmin = -2 * units.um
          s.xmax = 2 * units.um
          s.Nx = 1000
          plot(pc.real(s.n),settings);
```
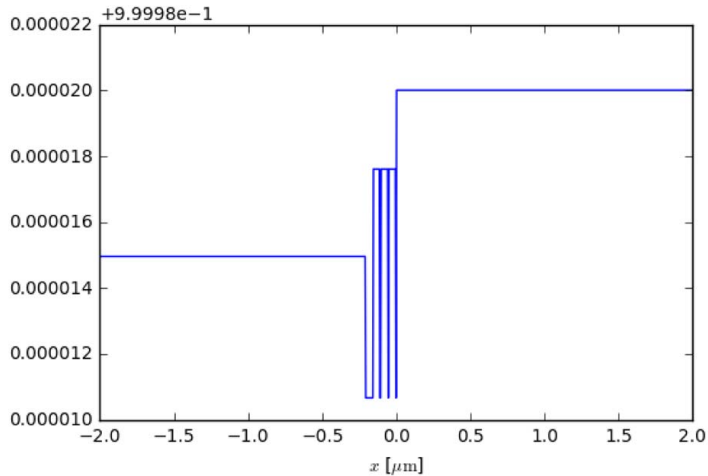

Figure out necessarry simulation box resolution

```
In [13]:  # incident angle region
          s.alphamax = 0.25 * units.degrees
          s.alphamin = 0.1 * units.degrees
          g.z_0 = 0
          g.x_0 = 0
          g.sigma_x = 130 * units.nm / (pc.sqrt(8*pc.log(2)))    # FWHM
```

```
In [14]:  # pixel sizes in x and z directions
          test_settings = settings.copy()
          test_settings.wave_equation.n = 1
          test_settings.simulation_box.zmin = 0
          test_settings.simulation_box.zmax = 5 * units.mm
          test_settings.simulation_box.xmax = 5 * units.um
          test_settings.simulation_box.xmin = -15 * units.um
          test_settings.simulation_box.Nx = 20000
          test_settings.simulation_box.Nz = 50000
```

```
In [15]:  if tests:
              test_settings.partial_differential_equation.alpha0 = s.alphamax
              propagator = propagators.FiniteDifferencesPropagator1D(test_settings)
              test_field = propagator.run_slice()[::s.sx/1000,::s.sz/1000]
```

In [16]:
```
if tests:
    ansettings = test_settings.copy()
    ansettings.simulation_box.Nx = test_field.shape[1]
    ansettings.simulation_box.Nz = test_field.shape[0]
    anfield = expression_to_array(ansettings.get(s.u0).subs(s.alpha,s.alpha
max),ansettings)
```

In [17]:
```
if tests:
    #plot(abs(anfield),vmax=0.7)
    plot(abs(test_field),vmax=0.7)
    plot(abs(abs(test_field) - abs(anfield)),vmax=0.7)
```

In [18]:
```
s.Nx = pc.ceil(s.sx/test_settings.get_numeric(s.dx))
s.Nz = pc.ceil(s.sz/test_settings.get_numeric(s.dz))
```

Set simulation box

In [19]:
```
g.sigma_x = 130 * units.nm / (pc.sqrt(8*pc.log(2))) # FWHM
s.xmin = -2 * units.um
s.xmax = 15 * units.um
s.zmin = 0
s.zmax = 3 * units.mm
g.z_0 = 0
g.x_0 = 0
```

In [20]:
```
if tests:
    settings.partial_differential_equation.alpha0 = s.alphamin
    propagator = propagators.FiniteDifferencesPropagator1D(settings)
    min_field = propagator.run_slice()[::s.sx/1000,::s.sz/1000]
    plot(min_field)
```

In [21]:
```
if tests:
    settings.partial_differential_equation.alpha0 = s.alphamax
    propagator = propagators.FiniteDifferencesPropagator1D(settings)
    max_field = propagator.run_slice()[::s.sx/1000,::s.sz/1000]
    plot(max_field)
```

Calculate the fields

In [22]:
```
# setting the incident angle simulated region
s.alphamin = 0.1 * units.degrees
s.alphamax = 0.25 * units.degrees
s.Nalpha = 1500
```

g2hg 0.3 mm

In [23]:
```
g.sigma_x = 130 * units.nm / (pc.sqrt(8*pc.log(2))) # FWHM
```

```
In [24]: propagator_595 = propagators.FiniteDifferencesPropagator2D(settings)
```

```
In [25]: propagator_595._solver.thread_count = 12
```

```
In [26]: inner_field_595 = propagator_595.run_slice()[dmin:dmax:(dmax - dmin)/100
         0,:,::s.sz/1000]
```

```
         Simulation running. Step 1000/1000: 100% [███████████████████] [9041.1
         s] [eta 0s +- 0s]] Simulation running. Step 2/1000:    0% [
         ] [8.6 s] [eta 8607s +- 0s]
```

near field amlitude distribution with different angles

```
In [27]: plot(propagator_595.get_field(),figsize=(8,5))
```

```
Out[27]: <matplotlib.image.AxesImage at 0x7f50d5d85290>
```
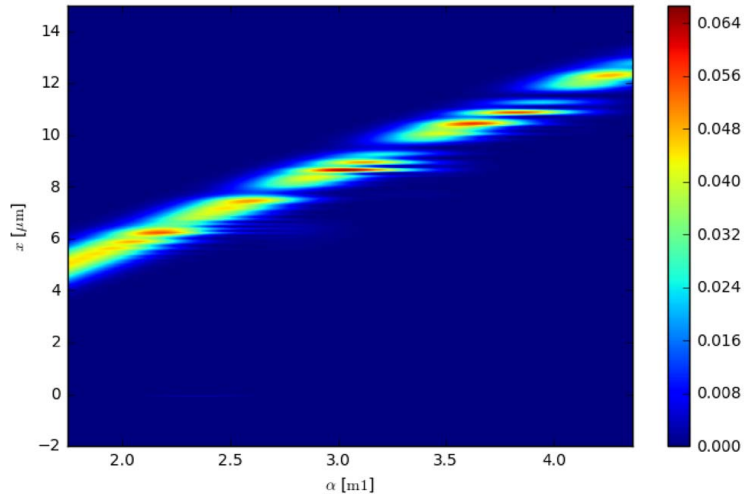

far field amlitude distribution with different angles

```
In [33]: farfielddata = (abs(np.fft.fftshift(np.fft.fft(propagator_595.get_field(),a
         xis=0),axes=[0]))**2)[::-1]
         farfield595 = CoordinateNDArray(farfielddata,[(-1,1),(s.alphamin,s.alphama
         x)],[pc.Symbol('x\''),s.alpha],settings.get_numeric_transform())
```

```
In [34]:  %matplotlib inline
          plot(farfield595[0.03:0.085],figsize=(10,5))
```

Out[34]: <matplotlib.image.AxesImage at 0x7f4fbc737d50>
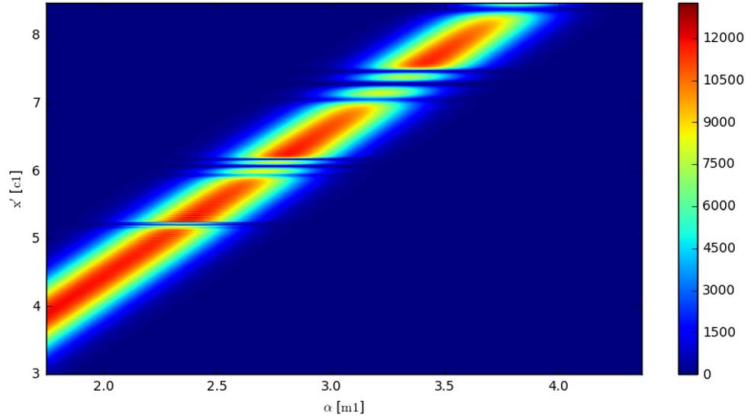
far field amlitude distribution shifted

```
In [35]:  shift = expression_to_array(pc.exp(1j*pc.sin(s.alpha)*s.x*s.k),settings).tr
          anspose()
          farfield595_shifteddata = (abs(np.fft.fftshift(np.fft.fft(propagator_595.ge
          t_field() * shift,axis=0),axes=[0]))**2)[::-1]
          farfield595_shifted = CoordinateNDArray(farfield595_shifteddata,[(-1,1),
          (s.alphamin,s.alphamax)],[pc.Symbol('x\''),s.alpha],settings.get_numeric_tr
          ansform())
```

```
In [36]:  %matplotlib inline
          plot(farfield595_shifted[-0.01:.01],figsize=(10,4))
```

Out[36]: <matplotlib.image.AxesImage at 0x7f4fbc5d0950>
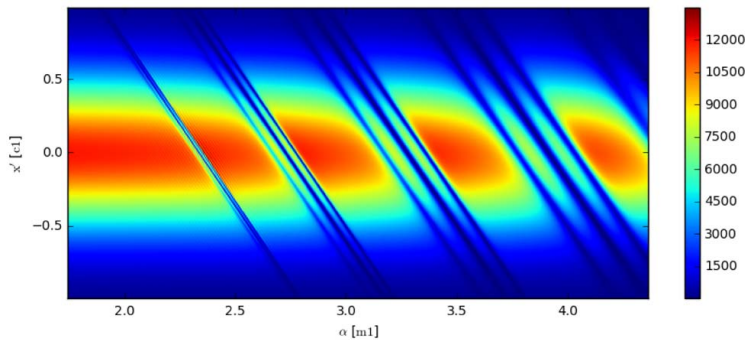
In [38]:
```
plot((abs(farfield595_shifted)**2).sum(axis=pc.Symbol('x\'')))# one dimenti
onal curve
```

Out[38]: <matplotlib.lines.Line2D at 0x7f4fbc2cc3d0>
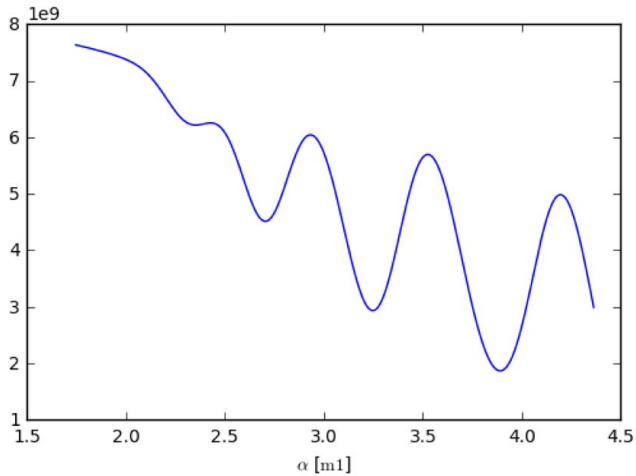
In [122]:
```
#Experimental data in the following
import scipy.io
exp_595 = scipy.io.loadmat('/IRP/AG_Salditt/Messzeiten/2016/GINIX/Analysi
s/Qi_Zhong/TJ0116C312/Eiger/TJ0116C322a_master_08.mat')
exp_595 = exp_595['data_sum'][::-1,::-1]
plt.imshow(exp_595,aspect='auto',norm=LogNorm(),vmax=10**9.5); plt.colorba
r()
```

Out[122]: <matplotlib.colorbar.Colorbar at 0x7ff2f30e5b10>
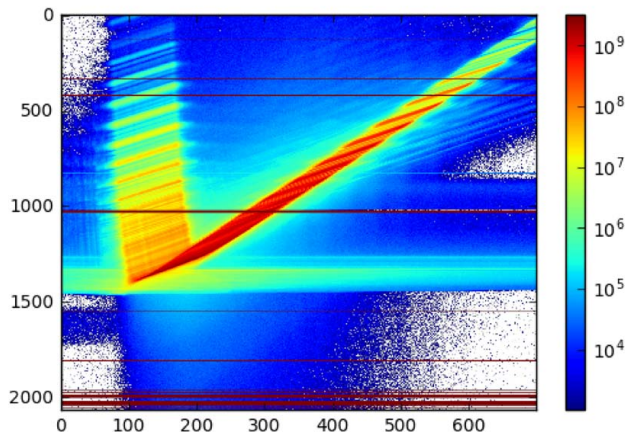
```
In [123]: # experimental data shifted
          x,y = np.meshgrid(np.arange(exp_595.shape[1]),np.arange(exp_595.shape[0]))
          exp_595_shifted = exp_595[ np.floor((y - x * 2.33) % exp_595.shape[0]).asty
          pe(int) ,x]
```

```
In [124]: bad_pixels = exp_595_shifted > 10**10
          ind = nd.distance_transform_edt(bad_pixels, return_distances=False, retur
          n_indices=True)
          exp_595_shifted = exp_595_shifted[tuple(ind)]
          plt.imshow(exp_595_shifted,aspect='auto',norm=LogNorm(),vmax=10**9.5)
```

Out[124]: <matplotlib.image.AxesImage at 0x7ff2f31c0dd0>
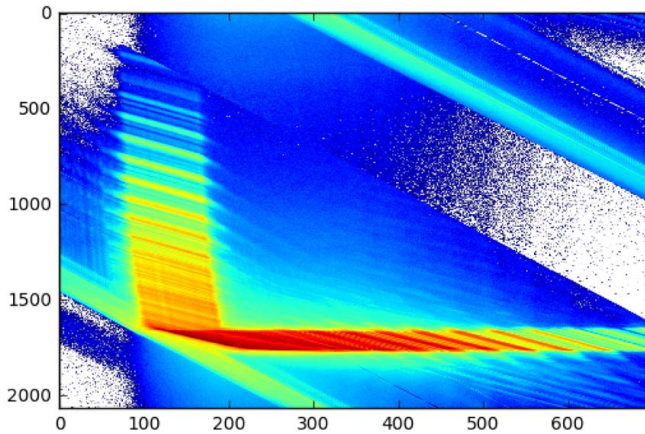

```
In [125]: plt.figure(figsize=(10,4))
          plt.imshow(exp_595_shifted[1650:1775,:],norm=LogNorm(),vmax=10**9.5,aspec
          t='auto',interpolation='None')
          plt.colorbar()
```

Out[125]: <matplotlib.colorbar.Colorbar at 0x7ff331b967d0>
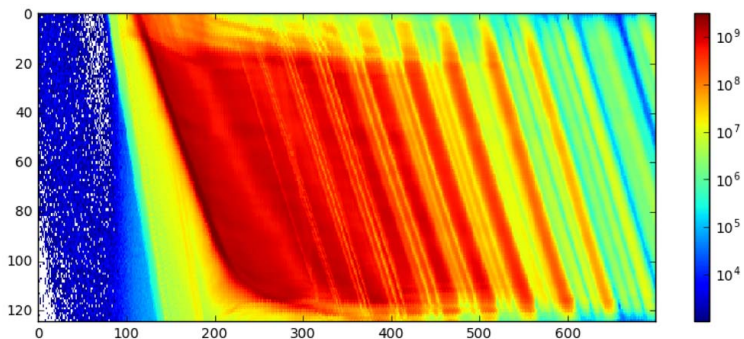
All the initial ipython codes are written by Lars Melchior. Qi Zhong has modified a small part of the scripts. The type of the source code is '.ipynb'.

The code for *Multi_guide_RBCs_three_guiding_layers* in App. B.1.1 illustrates that: the RBC with three guiding layers is simulated the field propagation inside and outside the structure; then the 2nd or 3rd reflected beams are exited from the RBC surface; finally the near-field information is collected and transformed to the far-field curve.

The code for *RBC_g2hg03_analysis* in App. B.1.2 presents the simulation of the experimental far-field distribution with different incident angle α_i. The process is as follows: first the wave field propagation in the RBCs structure is simulated at a certain angle; second the corresponding plane (orthogonal to the reflected beam) is collected in the near-field; third the near-field distribution is calculated as a function of incident angle and transformed to the far-field pattern; finally the simulated far-field distribution is compared with an experimental one.

C.1 Different scan methods in *Wendi* in-house setup
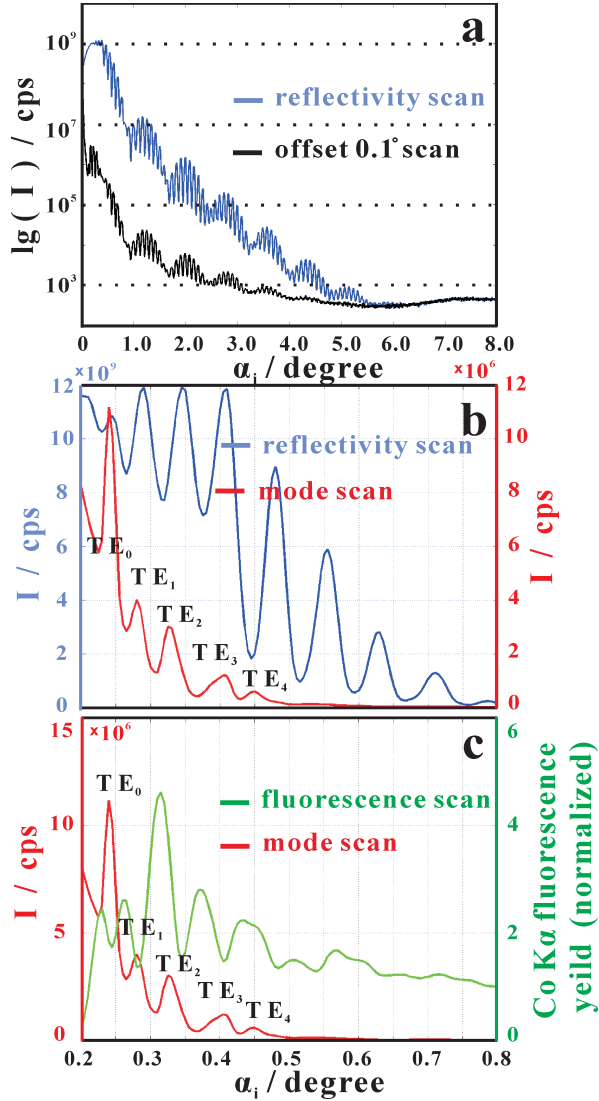
Figure C11: *(a) Measured reflectivity (blue line) and off-scan curve with off-scan angle 0.1° (black line) as a function of incident angle α_i for the RBCs sample with [Ni (5 nm)/C (50 nm)]$_3$ /Ni (50 nm) on GaAs substrate; (b) Detailed reflectvity scan (blue line) and mode scan (red line) as a function of α_i in the range from 0.2°–0.8° ; (c) mode scan (red line) and Co Kα fluorescence yield (green line) as a function of α_i in the range from 0.2°–0.8° .*

Fig. C11 presents the different scan curves measured by the in-house setup *Wendi* at the Institute for X-ray Physics, University of Göttingen. We assume the incident angle to be α_i, and the diffracted beam angle to be α_f.
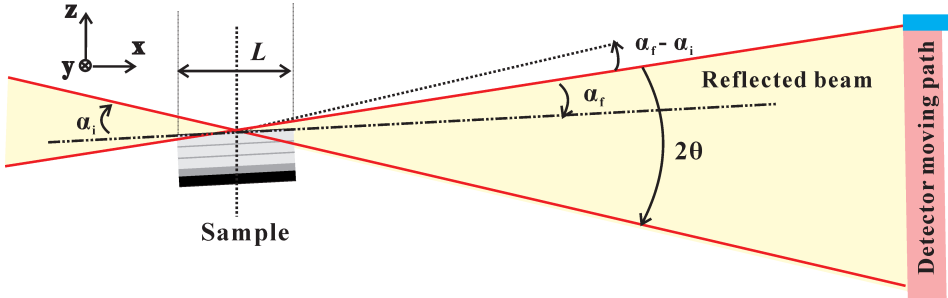
Figure C12: *The basic schematic of Wendi setup.*

The description of different scan methods are discussed in the following, based on the schematic of experimental setup in Fig. C12.

Reflectivity scan is the method which measures the intensity of the reflected beam as a function of incident angle α_i. The scintillation counter collects the diffracted beams with the angle α_f. When $\alpha_i = \alpha_f$, the reflectivity curve versus α_i in the range of $0°$ to $8°$ yields the reflectivity scan, also named $\theta - 2\theta$ scan, as shown in the blue line of Fig. C11(a).

Off-set reflectivity scan is the intensity of reflectivity beam when the incident and diffracted angles are not quite equal, followed by *off-set angle = $\alpha_i - \alpha_f$*. It is to be noted that during the off-set reflectivity scan, if we want to subtract a background signal, the normal way is to measure the background reflectivity with a small offset of the incident beam or diffracted beam. Thus, in the off-set reflectivity (black line) as shown in Fig. C11(a, b), the 'background' signal is measured with the off-set angle $\alpha_i - \alpha_f = 0.1°$ of incident beam.

Mode scan is an intensity curve of diffracted beam when the diffracted angle $\alpha_f = 0$. In this case, the guided modes are resonantly excited by shining a parallel beam onto the waveguide under grazing incidence, using a precisely controlled incidence angle α_i for each modes. At these angles, photons "get trapped" under the resonance conditions in the guiding layer propagating parallel to the surface over an active coupling length L, final coupled out. The resonant modes (TE_0, TE_1, TE_2, TE_3 and TE_4 modes) excitation manifest themselves in the plateau of total in the form of sharp dips (cusps) at a set of α_i as shown in the red line of Fig. C11(b, c).

Fluorescence scan is measured by the *Wendi* setup and a fluorescence detec-

tor (AXAS, KETEK GmbH) which is placed vertical to the sample surface with a distance (3 – 5 mm). The sample structure: a Co layer with < 1 nm is inserted into the central part of top C layer in the RBCs with $[Ni$ (5 nm)$/C$ (50 nm)$]_3 /Ni$ (50 nm) on GaAs substrate. With collecting the $Co\ K\alpha$ fluorescence signal, the cusps of the Co Kα fluorescence as a function of α_i are presented in the green line of Fig. C11(c). The detailed fluorescence pattern depends upon the position and thickness of the Co marker layer [93]. Owing to the thinned Co layer and limited step sizes of the instruments, the fluorescence peaks can not match the corresponding resonant modes.

Bibliography

[1] W. Röntgen. Über eine neue Art von Strahlen. *Sitzungsberichte der physikal.-medizin. Gesellschaft*, 137:132–141, 1895.

[2] E. Abbe. Beiträge zur Theorie des Mikroskops und der mikroskopischen Wahrnehmung. *Archiv für mikroskopische Anatomie*, 9(1):413–418, 1873.

[3] D. H. Bilderback, S. A. Hoffman, and D. J. Thiel. Nanometer spatial resolution achieved in hard x-ray imaging and Laue diffraction experiments. *Science*, 263(5144):201–203, 1994.

[4] D. J. Thiel, D. H. Bilderback, A. Lewis, and E. A. Stern. Submicron concentration and confinement of hard x-rays. *Nuclear Instruments and Methods in Physics Research Section A: Accelerators, Spectrometers, Detectors and Associated Equipment*, 317(3):597 – 600, 1992.

[5] P. Kirkpatrick and A. V. Baez. Formation of Optical Images by X-Rays. *J. Opt. Soc. Am.*, 38(9):766–774, 1948.

[6] O. Hignette, P. Cloetens, W. K. Lee, W. Ludwig, and G. Rostaing. Hard X-ray microscopy with reflecting mirrors status and perspectives of the ESRF technology. *J. Phys. IV France*, 104:231–234, 2003.

[7] A. Snigirev, V. Kohn, I. Snigireva, A. Souvorov, and B. Lengeler. Focusing high-energy x rays by compound refractive lenses. *Appl. Opt.*, 37(4):653–662, 1998.

[8] C. G. Schroer, O. Kurapova, J. Patommel, P. Boye, J. Feldkamp, B. Lengeler, M. Burghammer, C. Riekel, L. Vincze, A. van der Hart, and M. Kuchler. Hard x-ray nanoprobe based on refractive x-ray lenses. *Appl. Phys. Lett.*, 87(12):124103–3, 2005.

[9] J. Vila-Comamala, Y. S. Pan, J. J. Lombardo, W. M. Harris, W. K. S. Chiu, C. David, and Y. X. Wang. Zone-doubled Fresnel zone plates for high-resolution hard X-ray full-field transmission microscopy. *J. Synchrotron Rad.*, 19(5):705–709, 2012.

[10] M. Osterhoff, M. Bartels, F. Döring, C. Eberl, T. Hoinkes, S. Hoffmann, T. Liese, V. Radisch, A. Rauschenbeutel, A.-L. Robisch, A. Ruhlandt, F. Schlenkrich, T. Salditt, and H.-U. Krebs. Two-dimensional sub-5-nm hard x-ray focusing with MZP. *Proc. SPIE*, 8848:884802–884802–8, 2013.

[11] M. Bartels, M. Krenkel, J. Haber, R. N. Wilke, and T. Salditt. X-Ray Holographic Imaging of Hydrated Biological Cells in Solution. *Phys. Rev. Lett.*, 114:048103, 2015.

[12] T. Salditt, M. Osterhoff, M. Krenkel, R. N. Wilke, M. Priebe, M. Bartels, S. Kalbfleisch, and M. Sprung. Compound focusing mirror and X-ray waveguide optics for coherent imaging and nano-diffraction. *J. Synchrotron Rad.*, 22(4):867–878, 2015.

[13] E. Spiller and A. Segmüller. Propagation of x rays in waveguides. *Applied Physics Letters*, 24(2):60–61, 1974.

[14] Y. P. Feng, S. K. Sinha, H. W. Deckman, J. B. Hastings, and D. P. Siddons. X-ray flux enhance-

ment in thin-film waveguides using resonant beam couplers. *Phys. Rev. Lett.*, 71(4):537–540, 1993.

[15] S. Lagomarsino, A. Cedola, P. Cloetens, S. Di Fonzo, W. Jark, G. Soullié, and C. Riekel. Phase contrast hard x-ray microscopy with submicron resolution. *Appl. Phys. Lett.*, 71(18):2557–2559, 1997.

[16] V. K. Egorov and E. V. Egorov. Physics of planar x-ray waveguide. *Proc. SPIE*, 4502:148–172, 2001.

[17] W. Jark and S. Di Fonzo. Prediction of the transmission through thin-film waveguides for X-ray microscopy. *J Synchrotron Rad*, 11(5):386–392, 2004.

[18] M. J. Zwanenburg, J. F. Peters, J. H. H. Bongaerts, S. A. de Vries, D. L. Abernathy, and J. F. van der Veen. Coherent Propagation of X Rays in a Planar Waveguide with a Tunable Air Gap. *Phys. Rev. Lett.*, 82(8):1696–1699, 1999.

[19] F. Pfeiffer, C. David, M. Burghammer, C. Riekel, and T. Salditt. Two-Dimensional X-ray Waveguides and Point Sources. *Science*, 297(6):230, 2002.

[20] C. Fuhse and T. Salditt. Finite-difference field calculations for one-dimensionally confined X-ray waveguides. *Physica B: Condensed Matter*, 357(1-2):57–60, 2005.

[21] H. Neubauer, S. Hoffmann, M. Kanbach, J. Haber, S. Kalbfleisch, S. P. Krüger, and T. Salditt. High aspect ratio x-ray waveguide channels fabricated by e-beam lithography and wafer bonding. *J. Appl. Phys.*, 115(21):214305, 2014.

[22] C. Fuhse, C. Ollinger, and T. Salditt. Waveguide-Based Off-Axis Holography with Hard X-Rays. *Phys. Rev. Lett.*, 97(25):254801, 2006.

[23] H. Y. Chen, S. Hoffmann, and T. Salditt. X-ray beam compression by tapered waveguides. *Applied Physics Letters*, 106(19):194105, 2015.

[24] T. Salditt, S. Hoffmann, M. Vassholz, J. Haber, M. Osterhoff, and J. Hilhorst. X-Ray Optics on a Chip: Guiding X Rays in Curved Channels. *Phys. Rev. Lett.*, 115:203902, 2015.

[25] C. Fuhse, A. Jarre, C. Ollinger, J. Seeger, T. Salditt, and R. Tucoulou. Front-coupling of a prefocused x-ray beam into a monomodal planar waveguide. *Appl. Phys. Lett.*, 85(11):1907–1909, 2004.

[26] C. Bergemann, H. Keymeulen, and J. F. van der Veen. Focusing X-Ray Beams to Nanometer Dimensions. *Phys. Rev. Lett.*, 91(20):204801, 2003.

[27] S. P. Krüger, K. Giewekemeyer, S. Kalbfleisch, M. Bartels, H. Neubauer, and T. Salditt. Sub-15 nm beam confinement by twocrossed x-ray waveguides. *Opt. Express*, 18(13):13492–13501, 2010.

[28] S. P. Krüger, H. Neubauer, M. Bartels, S. Kalbfleisch, P. J. Giewekemeyer, K. Wilbrandt, M. Sprung, and T. Salditt. Sub-10 nm beam confinement by X-ray waveguides: design, fabrication and characterization of optical properties. *J. Synchrotron Rad.*, 19(2):227–236, 2012.

[29] T. Salditt, S. P. Krüger, C. Fuhse, and C. Bahtz. High-Transmission Planar X-Ray Waveguides.

Phys. Rev. Lett., 100(18):184801–4, 2008.

[30] F. Pfeiffer, T. Salditt, P. Høghøj, I. Anderson, and N. Schell. X-ray waveguides with multiple guiding layers. *Physical Review B*, 62(24):16939, 2000.

[31] F. Pfeiffer, T. Salditt, P. Høghøj, and C. David. New design schemes for x-ray waveguides based on multiple guiding layers and two-dimensional nanostructures. In *International Symposium on Optical Science and Technology*, pages 193–202. International Society for Optics and Photonics, 2001.

[32] I. R. Prudnikov. X-ray waveguides based on Bragg scattering of multilayers. *Phys. Rev. B*, 67:233303, 2003.

[33] I. R. Prudnikov. X-ray guided modes produced by Bragg reflections of multilayers: an analytical treatment. *Journal of Applied Crystallography*, 38(4):595–602, 2005.

[34] D. Marcuse. *Theory of dielectric optical waveguides*. Academic Press, New York, 1974.

[35] A. Jarre, T. Salditt, T. Panzner, U. Pietsch, and F. Pfeiffer. White beam x-ray waveguide optics. *Applied physics letters*, 85(2):161–163, 2004.

[36] M. Osterhoff and T. Salditt. Real structure effects in X-ray waveguide optics: The influence of interfacial roughness and refractive index profile on the near-field and far-field distribution. *Optics Communications*, 282(16):3250 – 3256, 2009.

[37] C. Fuhse. *X-ray waveguides and waveguide-based lensless imaging*. PhD thesis, 2006.

[38] F. Pfeiffer. X-ray Waveguides. Master's thesis, 1999.

[39] B. L. Henke, E. M. Gullikson, and J. C. Davis. X-Ray Interactions: Photoabsorption, Scattering, Transmission, and Reflection at E = 50-30,000 eV, Z = 1-92. *Atomic Data and Nuclear Data Tables*, 54(2):181 – 342, 1993.

[40] D. T. Attwood. *Soft X-Rays and Extreme Ultraviolet Radiation: Principles and Applications*. Ernest Orlando Lawrence Berkeley National Laboratory, Advanced Light Source, Berkeley, CA (US), 1999.

[41] M. Howells, C. Jacobsen, T. Warwick, and A. Van den Bos. Principles and applications of zone plate X-ray microscopes. In *Science of microscopy*, pages 835–926. Springer, 2007.

[42] T. Salditt, F. Pfeiffer, H. Perzl, A. Vix, U. Mennicke, A. Jarre, A. Mazuelas, and T. Metzger. X-ray waveguides and thin macromolecular films. *Physica B: Condensed Matter*, 336(1):181–192, 2003.

[43] Z. Jiang, D. R. Lee, S. Narayanan, J. Wang, and S. K. Sinha. Waveguide-enhanced grazing-incidence small-angle x-ray scattering of buried nanostructures in thin films. *Physical Review B*, 84(7), 2011.

[44] D. Pelliccia, S. Kandasamy, and M. James. Characterization of thin films for X-ray and neutron waveguiding by X-ray reflectivity and atomic force microscopy. *physica status solidi (a)*, 210(11):2416–2422, 2013.

[45] D. L. Windt. IMD–Software for modeling the optical properties of multilayer films. *Computers in Physics*, 12(4):360–370, 1998.

[46] F. Goos and H. Hänchen. Ein neuer und fundamentaler Versuch zur Totalreflexion. *Annalen der Physik*, 436(7-8):333–346, 1947.

[47] F. Goos and H. Lindberg-Hänchen. Neumessung des Strahlversetzungseffektes bei Totalreflexion. *Annalen der Physik*, 440(3-5):251–252, 1949.

[48] K. Artmann. Berechnung der Seitenversetzung des totalreflektierten Strahles. *Annalen der Physik*, 437(1-2):87–102, 1948.

[49] R. H. Renard. Total Reflection: A New Evaluation of the Goos–Hänchen Shift. *J. Opt. Soc. Am.*, 54(10):1190–1197, 1964.

[50] A. W. Snyder and J. D. Love. Goos-Hänchen shift. *Appl. Opt.*, 15(1):236–238, 1976.

[51] F. Pillon, H. Gilles, S. Girard, M. Laroche, R. Kaiser, and A. Gazibegovic. Goos-Hänchen and Imbert-Fedorov shifts for leaky guided modes. *J. Opt. Soc. Am. B*, 22(6):1290–1299, 2005.

[52] M. Merano, A. Aiello, G. W.'t Hooft, M. P. van Exter, E. R. Eliel, and J. P. Woerdman. Observation of Goos-Hänchen shifts in metallic reflection. *Opt. Express*, 15(24):15928–15934, 2007.

[53] X. M. Liu, Z. Q. Cao, P. F. Zhu, and Q. S. Shen. Solution to causality paradox upon total reflection in optical planar waveguide. *Phys. Rev. E*, 73:016615, 2006.

[54] M. Delgado and E. Delgado. Evaluation of a total reflection set-up by an interface geometric model. *Optik - International Journal for Light and Electron Optics*, 113(12):520 – 526, 2003.

[55] M. J. Bedzyk, G. M. Bommarito, M. Caffrey, and T. L. Penner. Diffuse-double layer at a membrane-aqueous interface measured with x-ray standing waves. *Science*, 248(4951):52–56, 1990.

[56] C. Ollinger, C. Fuhse, A. Jarre, and T. Salditt. Two-dimensional X-ray waveguides on a grating. *Physica B: Condensed Matter*, 357(1-2):53–56, 2005.

[57] A. Jarre, J. Seeger, C. Ollinger, C. Fuhse, C. David, and T. Salditt. X-ray waveguide nanostructures: Design, fabrication, and characterization. *Journal of Applied Physics*, 101(5):054306, 2007.

[58] J. Crank and P. Nicolson. A practical method for numerical evaluation of solutions of partial differential equations of the heat-conduction type. *Proc. Cambridge Philos. Soc.*, 43:55–67, 1947.

[59] J. W. Goodman. *Introduction to Fourier optics*. Roberts and Company Publishers, 2005.

[60] L. Melchior. Pypropagate. https://github.com/TheLartians/PyPropagate, 2016.

[61] J. R. Fienup. Reconstruction of an object from the modulus of its Fourier transform. *Opt. Lett.*, 3(1):27–29, 1978.

[62] J. R. Fienup. Phase retrieval algorithms: a comparison. *Appl. Opt.*, 21(15):2758–2769, 1982.

[63] S. Marchesini. Invited article: A unified evaluation of iterative projection algorithms for phase retrieval. *Review of Scientific Instruments*, 78(1):011301, 2007.

[64] V. Elser. Phase retrieval by iterated projections. *J. Opt. Soc. Am. A*, 20(1):40–55, 2003.

[65] Z. S. Wang, H. C. Wang, J. T. Zhu, Z. Zhang, Y. Xu, S. M. Zhang, W. J. Wu, F. L. Wang, B. Wang, L. Q. Liu, L. Y. Chen, A. G. Michette, S. J. Pfauntsch, A. K. Powell, F. Schüfers, A. Gaupp, and M. MacDonald. Broadband Mo-Si multilayer transmission phase retarders for the extreme ultraviolet. *Applied Physics Letters*, 90(3):031901, 2007.

[66] Q. Zhong, W. B. Li, Z. Zhang, J. T. Zhu, Q. S. Huang, H. C. Li, Z. S. Wang, P. Jonnard, K. L. Guen, J. M. André, H. J. Zhou, and T. L. Huo. Optical and structural performance of the Al(1%wtSi)/Zr reflection multilayers in the 17–19nm region. *Opt. Express*, 20(10):10692–10700, 2012.

[67] Q. Zhong, Z. Zhang, J. T. Zhu, Z. S. Wang, P. Jonnard, K. L. Guen, and J. M. André. The chemical characterization and reflectivity of the Al(1.0%wtSi)/Zr periodic multilayer. *Applied Surface Science*, 259:371 – 375, 2012.

[68] Q. Zhong, Z. Zhang, J. T. Zhu, Z. S. Wang, P. Jonnard, K. L. Guen, Y. Y. Yuan, J. M. André, H. J. Zhou, and T. L. Huo. The thermal stability of Al(1%wtSi)/Zr EUV mirrors. *Applied Physics A*, 109(1):133–138, 2012.

[69] Q. Zhong, Z. Zhang, S. Ma, R. Z. Qi, J. Li, Z. S. Wang, K. L. Guen, J. M. André, and P. Jonnard. The transition from amorphous to crystalline in Al/Zr multilayers. *Journal of Applied Physics*, 113(13):133508, 2013.

[70] Q. Zhong, Z. Zhang, S. Ma, R. Z. Qi, J. Li, Z. S. Wang, P. Jonnard, K. L. Guen, and J. M. André. Thermally induced structural modification in the Al/Zr multilayers. *Applied Surface Science*, 279:334 – 342, 2013.

[71] Q. Zhong, Z. Zhang, R. Z. Qi, J. Li, Z. S. Wang, K. L. Guen, J. M. André, and P. Jonnard. Enhancement of the reflectivity of Al/Zr multilayers by a novel structure. *Opt. Express*, 21(12):14399–14408, 2013.

[72] S. P. Krüger. *Optimization of waveguide optics for lensless x-ray imaging*. PhD thesis, 2010.

[73] S. Aeffner, T. Reusch, B. Weinhausen, and T. Salditt. Energetics of stalk intermediates in membrane fusion are controlled by lipid composition. *Proceedings of the National Academy of Sciences*, 109(25):E1609–E1618, 2012.

[74] S. Kalbfleisch, M. Osterhoff, K. Giewekemeyer, H. Neubauer, S. P. Krüger, B. Hartmann, M. Bartels, M. Sprung, O. Leupold, F. Siewert, and T. Salditt. The holography endstation of beamline P10 at PETRA III. *SRI 2009, 10TH INTERNATIONAL CONFERENCE ON RADIATION INSTRUMENTATION*, 1234(1):433–436, 2010.

[75] S. Kalbfleisch, H. Neubauer, S. P. Krüger, M. Bartels, M. Osterhoff, D. D. Mai, K. Giewekemeyer, B. Hartmann, M. Sprung, and T. Salditt. The Göttingen Holography Endstation of Beamline P10 at PETRA III/DESY. *AIPConf.Proc.*, 1365(1):96–99, 2011.

[76] T. Salditt, S. Kalbfleisch, M. Osterhoff, S. P. Krüger, M. Bartels, K. Giewekemeyer,

H. Neubauer, and M. Sprung. Partially coherent nano-focused x-ray radiation characterized by Talbot interferometry. *Opt. Express*, 19(10):9656–9675, 2011.

[77] S. Kalbfleisch. *A Dedicated Endstation for Waveguide-based X-Ray Imaging*. PhD thesis, Universität Göttingen, 2012.

[78] M. Bartels. *Cone-beam x-ray phase contrast tomography of biological samples Optimization of contrast, resolution and field of view.* PhD thesis, Universität Göttingen, 2013.

[79] M. Osterhoff and T. Salditt. Coherence filtering of x-ray waveguides: analytical and numerical approach. *New Journal of Physics*, 13(10):103026, 2011.

[80] Q. Zhong, M. Osterhoff, M. W. Wen, Z. S. Wang, and T. Salditt. X-ray waveguide arrays: tailored near fields by multi-beam interference. *X-Ray Spectrometry*, 46(2):107–115, 2017.

[81] R. N. Wilke, J. Wallentin, M. Osterhoff, D. Pennicard, A. Zozulya, M. Sprung, and T. Salditt. High flux ptychographic imaging using the new [55]μm-pixel detector 'lambda' based on the medipix3 readout chip. *Acta Crystallogr.A*, 70:552–562, 2014.

[82] P. Thibault, M. Dierolf, A. Menzel, O. Bunk, C. David, and F. Pfeiffer. High-Resolution Scanning X-ray Diffraction Microscopy. *Science*, 321(5887):379–382, 2008.

[83] A. M. Maiden and J. M. Rodenburg. An improved ptychographical phase retrieval algorithm for diffractive imaging. *Ultramicroscopy*, 109(10):1256–1262, 2009.

[84] M. Guizar-Sicairos, S. T. Thurman, and J. R. Fienup. Efficient subpixel image registration algorithms. *Opt. Lett.*, 33(2):156–158, 2008.

[85] J Wang, M. J. Bedzyk, and M. Caffrey. Resonance-enhanced x-rays in thin films: a structure probe for membranes and surface layers. *Science*, 258(5083):775–778, 1992.

[86] T. Tamir and H. L. Bertoni. Lateral Displacement of Optical Beams at Multilayered and Periodic Structures. *J. Opt. Soc. Am.*, 61(10):1397–1413, 1971.

[87] A. Sharon, D. Rosenblatt, and A. A. Friesem. Resonant grating–waveguide structures for visible and near-infrared radiation. *J. Opt. Soc. Am. A*, 14(11):2985–2993, 1997.

[88] C. Kappel, A. Selle, M. A. Bader, and G. Marowsky. Resonant double-grating waveguide structures as inverted Fabry–Perot interferometers. *J. Opt. Soc. Am. B*, 21(6):1127–1136, 2004.

[89] L. G. Parratt. Surface Studies of Solids by Total Reflection of X-Rays. *Phys. Rev.*, 95(2):359–369, 1954.

[90] C. von Korff Schmising, B. Pfau, M. Schneider, C. M. Günther, M. Giovannella, J. Perron, B. Vodungbo, L. Müller, F. Capotondi, E. Pedersoli, N. Mahne, J. Lüning, and S. Eisebitt. Imaging Ultrafast Demagnetization Dynamics after a Spatially Localized Optical Excitation. *Phys. Rev. Lett.*, 112:217203, 2014.

[91] A. Barty. Time-resolved imaging using x-ray free electron lasers. *Journal of Physics B: Atomic, Molecular and Optical Physics*, 43(19):194014, 2010.

[92] R. Röhlsberger, K. Schlage, B. Sahoo, S. Couet, and R. Rüffer. Collective Lamb Shift in Single-Photon Superradiance. *Science*, 328(5983):1248–1251, 2010.

[93] A. Gupta, P. Rajput, A. Saraiya, V. R. Reddy, M. Gupta, S. Bernstorff, and H. Amenitsch. Depth profiling of marker layers using x-ray waveguide structures. *Phys. Rev. B*, 72:075436, 2005.

Own publications

1. Q. Zhong, M. Osterhoff, M. W. Wen, Z. S. Wang, and T. Salditt.
   X-ray waveguide arrays: tailored near-fields by multi-beam interference.
   X-ray Spectrometry, **46**(2), 107–115 (2017).
   http://onlinelibrary.wiley.com/doi/10.1002/xrs.2740/full

2. Q. Zhong, L. Melchior, J. C. Peng, Q. S. Huang, Z. S. Wang, and T. Salditt.
   Reconstruction of the near-field distribution in x-ray waveguide array.
   Journal of Applied Crystallography, **50**(3), 701–711 (2017).
   https://doi.org/10.1107/S1600576717004630

3. Q. Zhong, L. Melchior, J. C. Peng, Q. S. Huang, Z. S. Wang, and T. Salditt.
   The Goos-Hänchen effect observed for focused x-ray beams under reson-
   ant mode excitation.
   Optics Express, **25**(15), 17431–17445 (2017).
   https://doi.org/10.1364/OE.25.017431

Acknowledgment

Most importantly, I would like to thank for my dear wife Li. Thank you to accompany with me and give fully support in the four years. Thank you to let my angel Mila come into my life. Thanks to my dear parents to let me experience such wonderful life. With your love, I can do everything. I love you all.

Curriculum vitae

Personal information

Name: Qi Zhong

Date of birth: 06. Oct. 1987

Place of birth: Baoji City, Shaanxi, China

Citizenship: Chinese

Education

09/2013-present:	PhD student in the Group of Tim Salditt, Institute for X-ray Physics, Georg-August-Universität Göttingen; Funded by German Science Foundation DFG (SFB 755) and the China Scholarship Council (CSC) of China.
09/2010-03/2013:	Master student in the Group of Zhanshan Wang, MOE Key Laboratory of Advanced Micro-Structured Materials, Institute of Precision Optical Engineering, Department of Physics, Tongji University, Shanghai, China
09/2006-06/2010:	Bachelor student, Department of Physics, Northwestern Polytechnical University, Xi'an City, Shaanxi, China
09/2003-06/2006:	Baoji Middle School, Baoji City, Shaanxi, China